Journal of Baku Engineering University

P H Y S I C S

BEU
BAKU ENGINEERING UNIVERSITY

Journal of
Baku Engineering
University

PHYSICS

Baku - AZERBAIJAN

Journal of Baku Engineering University

PHYSICS

2019. Volume 3, Number 1

CONTENTS

SYNTHESIS AND STABILIZATION OF METAL NANOPARTICLES OF IRON, NICKEL AND COBALT

HAJIYEVA F.V

Department of Chemical physics of nanomaterials, Baku State University

Baku/AZERBAIJAN

_flora_1985@mail.ru, fhajiyeva@bsu.edu.az_

ABSTRACT

In present work have been synthesized and stabilized metalnanoparticles of iron (Fe), nickel (Ni) and cobalt (Co) in the presence of surface-active substances (SAS)-stabilizers. It was found that by varying the deposition conditions: the nature of the surfactant, the concentration of stabilizer , the concentration of the initial reagents, temperature, solution pH , one can control the dispersion, uniformity, dimensionality and purity of the resulting metallic nanoparticles. It was shown that in the presence of stabilizers:cetyltrimethylammonium bromide (CTABr) and sodium oleate, metal nanoparticles are well distributed and monodispersed.It was determined that the average size of iron nanoparticles in the presence of sodium oleate is 26-50 nm, nickel and cobalt in the presence of CTABr-14-20 nm and 44-100 nm respectively, which is well correlated with electron microscopic (SEM) and atomic force microscopic(AFM) analyzes .

Keywords: stabilizer, nanoparticles, surfactant, metal.

DƏMİR, NİKEL VƏ KOBALT METAL NANOHİSSƏCİKLƏRİNİN SİNTEZİ VƏ STABİLLƏŞDİRİLMƏSİ

XÜLASƏ

Səthi-aktiv maddələr- stabilizatorlar iştirakında dəmir (Fe), nikel (Ni) və kobal (Co)metal nanohissəcikləri sintez edilmiş və stabilləşdirilmişdir. Müəyyən olmuşdur ki, nanohissəciklərin alınması zamanı çökdürulmə şəraitini: səthi-aktiv maddənin təbiətini, onun konsentrasiyasının, ilkin prekursorların miqdarını, məhlulun pH-nı, temperaturu variasiya etməklə metal nanohissəciklərinin dispersliyini, bircinsliyini və təmizliyini idarə etmək olar. Göstərilmişdir ki, STABr və natrium oleat iştirakında metal nanohissəcikləri yaxşı dispersiya olumuş və monodisperdir. Həmçinin təyin edilmişdir ki, natrium oleat iştirakında stabilləşdirilmiş dəmir nanohissəciklərin orta ölçüləri 26-50 nm, STABr iştirakında stabilləşdirilmiş nikel və kobalt nanohissəciklərin ölçüləri isə uyğun olaraq 14-20 nm və 44-100 nm təşkil edir, bu isə elektron mikroskopik və atom-qüvvə mikroskopik analizlərlə yaxşı korelyasiya edir.

Açar sözlər: stabilləşdirici, nanohissəciklər, səthi-aktiv maddə, metal.

СИНТЕЗ И СТАБИЛИЗАЦИЯ НАНОЧАСТИЦ МЕТАЛЛОВ ЖЕЛЕЗА, НИКЕЛЯ И КОБАЛЬТА

РЕЗЮМЕ

В данной работе были синтезированы и стабилизированы наночастицы металлов железа (Fe), никеля (Ni) и кобальта(Co) в присутствии поверхностно-активных веществ (ПАВ)-стабилизаторов. Установлено, что варьируя условия осаждения: природу поверхностно-активного вещества, концентрацию стабилизатора, концентрацию исходных реагентов, температуру, pH раствора можно контролировать дисперсность, однородность, размерность и чистоту полученных металлических наночастиц. Показано, что в присутствии стабилизаторов: цетитриметиаммоний бромида (ЦТАBr) и олеата натрия наночастицы металлов хорошо диспергированы и монодисперсны. Определено, что средний размер наночастиц железа в присутствии олеата натрия составляет 26-50 нм, никеля и кобальта в присутствии ЦТАBr- 14-20 нм и 44-100 нм соответственно, что хорошо коррелируется с электронно (СЭМ) и атомно-силовыми (АСМ) микроскопическими анализами.

Ключевые слова: стабилизатор, наночастицы, поверхностно-активное вещество, металл.

1. INTRODUCTION:

The main problems of obtaining nanoparticles with a narrow size distribution during precipitation in an aqueous medium are the processes of agglomeration and aggregation and

the further crystalline growth of particles during synthesis. This plays an especially important role in the case of magnetic nanoparticles, the difference between the characteristics ofsurface layer and the core of the particle, and the interaction of internal atoms with external ones can lead to serious changes in the magnetic properties of nanoparticles. It is usually advisable to stabilize the nanoparticles directly in the process of their production in order to have a final product with their properties. To weaken the processes of agglomeration and aggregation, it is necessary to select the optimal parameters at which the precipitation reaction takes place: temperature, pH value, solution stirring speed, stabilizing surfactants and e.t.c. The surfactant molecules dissociate when they enter the solution and become charged. Adsorbed on the surface of particles, surfactant molecules prevent sticking and further aggregation and agglomeration of nanoparticles.

2. EXPERIMENTAL PART:

In this work, cobalt metalnanoparticles, nickel, iron and copper were synthesized. Nanoparticles of iron, cobalt and nickel were obtained by the method of chemical reduction of the corresponding salts of Fe, Co and Ni with sodium tetrahydroborate ($NaBH_4$) in the presence of various surfactant stabilizers.

Synthesis of magnetic iron nanoparticles was carried out in the presence of a sodium oleate stabilizer. To synthesize magnetic iron nanoparticles, 30 ml of 0.5% solution of sodium oleate is added to 100 ml of a 0.1 M solution of $FeCl_3$. The mixture is intensively mixed on a magnetic stirrer at room temperature for 30 minutes. Then a 0.3 M solution of $NaBH_4$ is rapidly added to the initial mixture. The solution turns sharply black, indicating the formation of iron nanoparticles. For another 20 minutes, the mixture is intensively changed on a magnetic stirrer. The black precipitate is separated from the solutionby centrifuge and washed several times with ethyl alcohol to remove extraneous unreacted salt ions. The precipitate is transferred to a Petri dish and dried in the open air during the day [1-3].

Co nanoparticles were synthesized in the presence of a stabilizer-cetylrimethylammonium bromide (CTABr). To this end, 30 ml of a 0.5% CTABr solution is added to 100 ml of 0.1 M $CoCl_3$ solution. The mixture is intensively mixed on a magnetic stirrer at room temperature for 30 minutes. Then 0.3 M solution of $NaBH_4$ is rapidly added to the initial mixture. The solution turns sharply black, indicating the formation of cobalt nanoparticles. Cobalt nanoparticles washed with distilled waterand ethyl alcohol to remove impurities [4-7]. Similarly, nickel nanoparticles were synthesized. As a precursor for the synthesis of nanoparticles, a0.1 M solution of $NaBH_4$ and 0.3 M solution of $NaBH_4$ were selected. The stabilization of nickel nanoparticles was also carried out in the presence of CTABr [8-12].

3. RESULTS AND DISCUSSION:

Figure 1 shows the diffraction patterns of nanoparticles of iron (a), nickel (b) and cobalt (c). As can be seen from fig. 1 (a) the main peaks at 2θ equal to 44.720 (110), 65.100 (200), 82.420 (211), 116.430 (310) belong to iron nanoparticles according to the base (ICDD no.00-006-0696) [1-3]. From Fig. 1 (b) also shows that the main peaks at 2θ equal to 44.40 (111), 51.70 (200) and 76.30 (220) belong to nickel nanoparticles, respectively, to the base (ICDD 01-078-7533). X-ray diffraction analysis of nanoparticles showed that the synthesized cobalt nanoparticles have an amorphous structure (Fig. 1 (c)).

Fig. 1. Diffractograms of nanoparticles of iron (a), nickel (b) and cobalt (c).
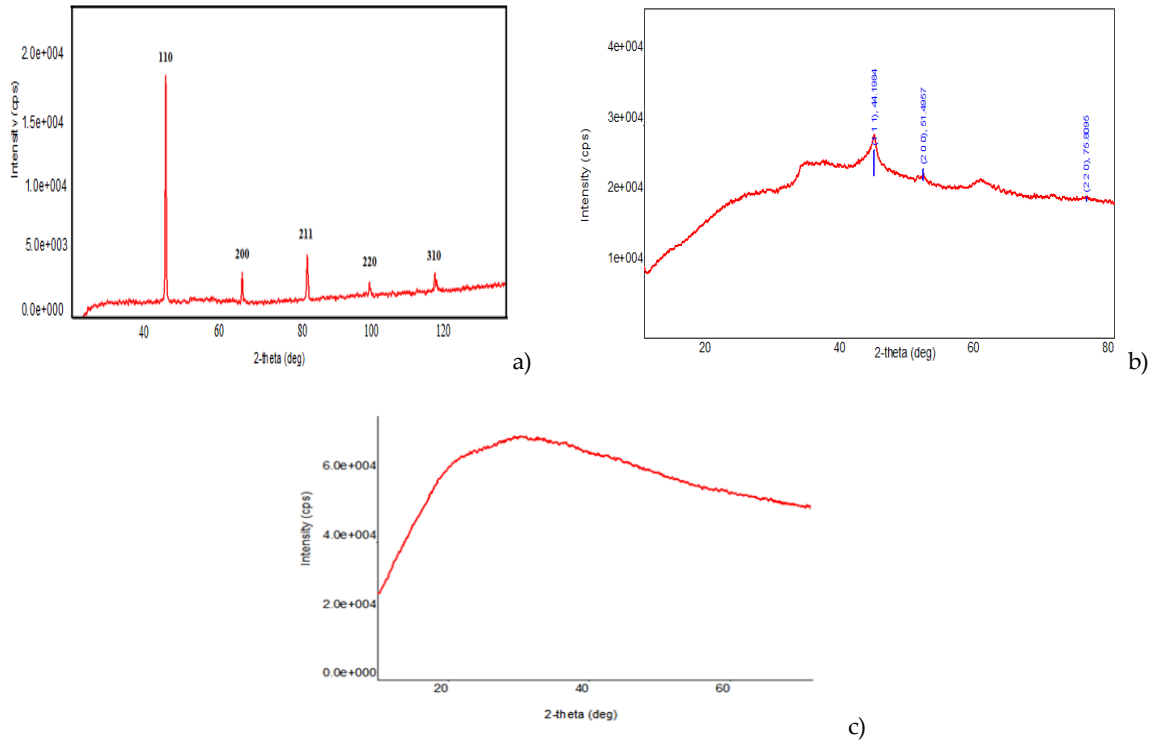
Fig.2. SEM images of iron (a), nickel (b) and cobalt (c)nanoparticles.
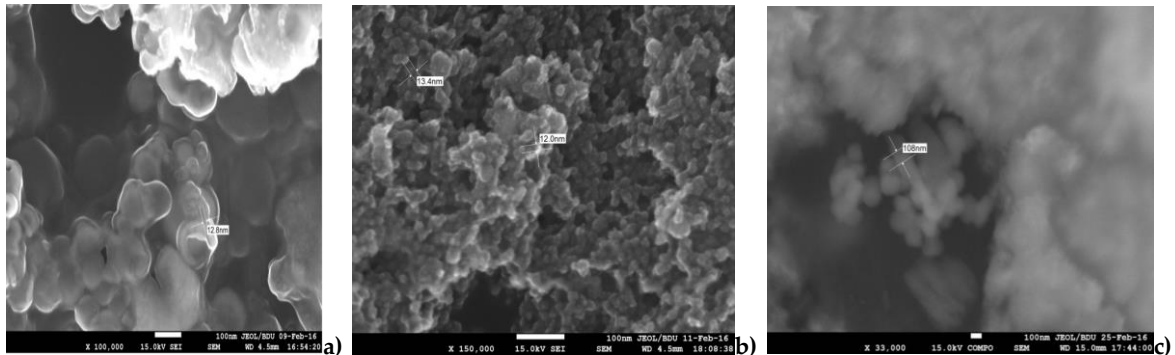
Figure 2 shows SEM images of nanoparticles of iron (a), nickel (b) and cobalt (c). SEM analysis was carried out in SEI and COMPO modes at an accelerating voltage of 15 keV and a working distance of 4.5 and 15 mm. The energy-dispersion spectrum (EDS) was obtained using the SEM-X-Max 50 prefix (Oxford Instruments). As can be seen from Fig. 2, the average size of stabilized iron nanoparticles is 26-50 nm, the average size of nickel nanoparticles is 12 nm, and cobalt is 40-100 nm. As can be seen, the stabilization of metal nanoparticles was carried out well, since metal nanoparticles are prone to agglomeration and aggregation and instantaneously oxidize immediately after production. Figure 3 shows the energy-dispersion spectra of nanoparticles of iron (a), nickel (b) and cobalt (c). As can be seen from Fig. 3, the synthesized nanoparticles have practically no impurities and non-participating ions, i.e. are pure metallic nanoparticles.

Fig.3 EDS spectrum of the iron (a), nickel (b) and cobalt (c) nanoparticles.
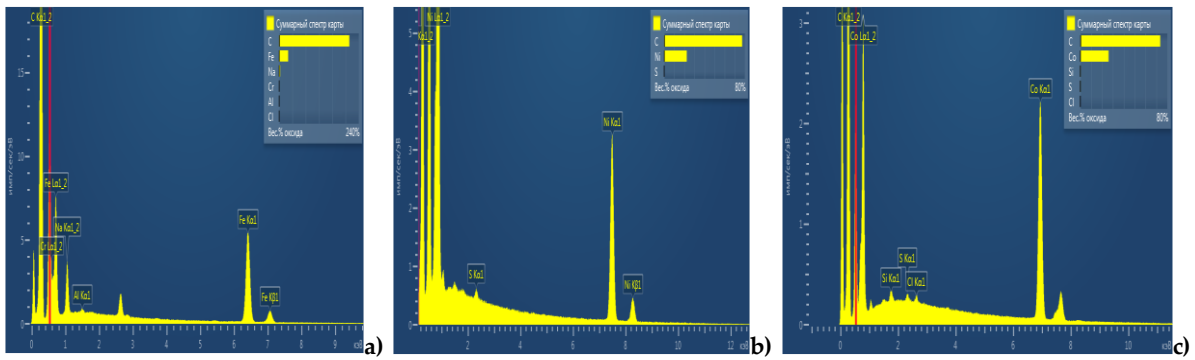
Fig.4. AFM images of iron (a), nickel (b) and cobalt (c) nanoparticles.
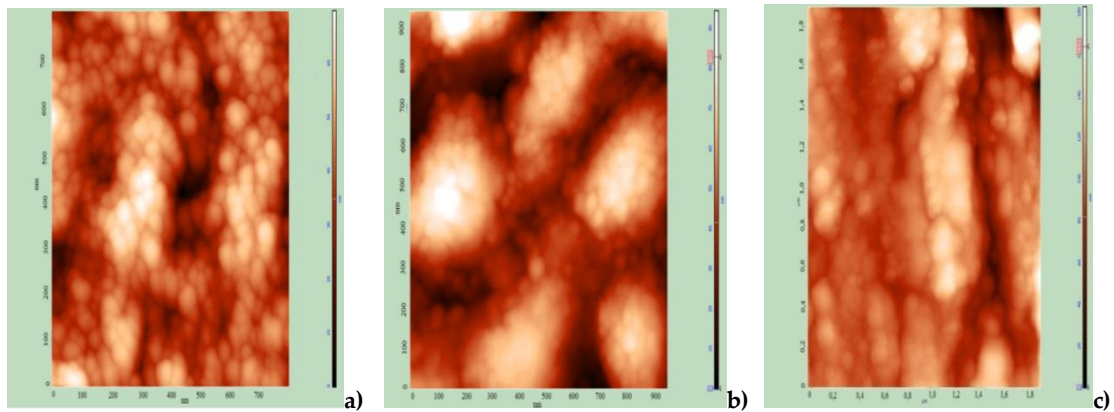
In Fig.4. AFM images of iron (a), nickel (b) and cobalt (c) nanoparticles are shown. The morphology of the nanocomposites was studied using microscopeIntegraPrima 2011 (NT-MDT, Zelenograd). Figure 5 shows histograms of the size-distribution of nanoparticles of iron (a), nickel (b) and cobalt (c). AFM results show that the average size of iron nanoparticles is 12-45 nm, nickel-18-20 nm, and cobalt-44-100 nm. Also, AFM images show that nanoparticles of metal nanoparticles are well distributed and dispersed in stabilized systems. As can be seen, the results of the SEM and AFM studies correlate well with each other.
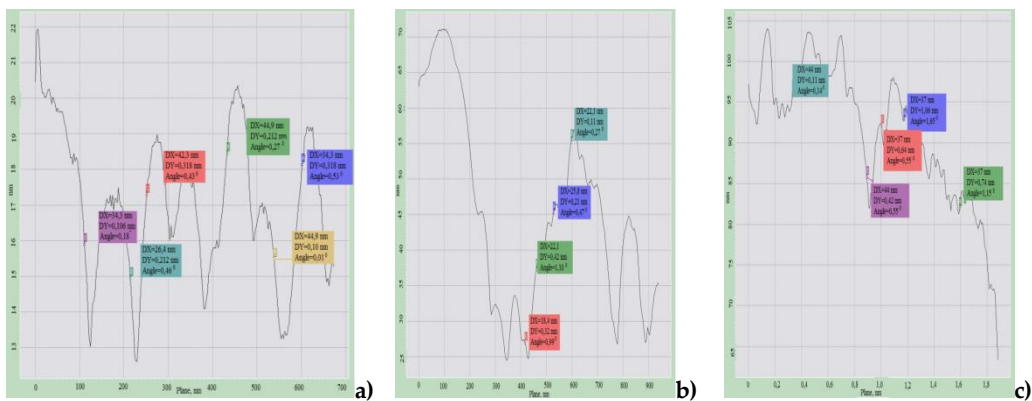
Fig.5 Histogram of the distribution of nanoparticles of iron (a), nickel (b) and cobalt (c) in size.

The main advantage of the space-limitedsystems, that is, the stabilizer in which the nano-phase is formed, is the high degree of monodispersity of the synthesized particles, which is diffi-cult to achieve by other methods. The formation of a spatially limited reaction zone in colloidal systems occurs mainly as a result of non-covalent (lyophilic / lyophobic, van der Vaals,

electrostatic) interaction of organic molecules with each other. It is on this principle that natural nanoreactors and nanocontainers are built: molecular systems, non-covalently interconnected, limit the reaction zone, and organic membranes serve to regulate the flow of a substance. In water, the hydrophobic parts of the surfactant molecules in a polar solvent combine to form a non-polar "island" (usually of a spherical shape). Once in the water, the surfactant molecules first of all fill its surface and form a monomolecular film. In the film, the polar part of the surfactant molecule becomes immersed in the inlet, and the non-polar hydrophobic radical is located in the air, which leads to a decrease in the surface tension of water (hence the term "surfactants"). After the surface is filled, new stabilizer molecules pass into the volume of water, and when a certain concentration is reached — the critical concentration of the micelle formation, the formation of aggregates (ensembles) of molecules occurs quickly.

CONCLUSION:

Therefore, analyzing the above experimental results we can conclude that by varying the deposition conditions: the nature of the surfactant, the surfactant concentration, the concentration of the initial reagents, temperature, solution pH, one can controlthe dispersion, uniformity, dimensionality and purity of the resulting metallic nanoparticles.

REFERENCES:

1. Yuvakkumar R.,ElangoV., Rajendran V.,KannanN. Preparation and characterization of zero valent iron nanoparticles Digest Journal of Nanomaterials and Biostructures Vol. 6, №4, October-December 2011, p. 1771-1776

2. Hu Ping, Kang Lu, Yang Lun, Yang Fan, Wang Kuaishe, Du Jinjing, Yang Zhanlin, Cao Weicheng, Liu Dongxin Synthesis of Fe Nanoparticles via One-Step Reduction Method Rare Metal Materials and EngineeringVolume 45, Issue 12, December 2016, Pages 3112-3114

3. Ruíz-BaltazarA., ClaudiaLópez, R. Pérez and RosasG. Structural Characterization of Iron Nanoparticles Synthesized by Chemical –Methods Mater. Res. Soc. Symp. Proc. Vol. 1372, 2012 Materials Research Society, p.73-77

4. Xiaoming L., Lijun Z. Room-temperature synthesis of air-stable cobalt nanoparticles and their high-efficient adsorption ability for Congo red/Electronic Supplementary Material (ESI) for RSC Advances The Royal Society of Chemistry 2012.

5. Jennifer N. Duggan Michael J. BozackChristopher B. Roberts: The synthesis and arrested oxidation of amorphous cobalt nanoparticles using DMSO as a functional solvent/ Journal of Nanoparticles ResearchNovember 2013, 15:2089

6. Liu Biao, Guan Jian-guo, Wang Qi and Zhang Qing-jie Preparation of Nanometer Cobalt Particles by Polyol Reduction Process and Mechanism Research Materials Transactions, Vol. 46, №8 (2005) pp. 1865 to 1867

7. NordinN.H., NeoY.S., and OngB.H.Synthesis and Characterisation of Pure Cobalt Magnetic Nanoparticle by Metal Reduction AIP Conference Proceedings 1136, 123 (2009)

8. Ankur P., Manivannan R. Chemical reduction technique for the synthesis of nickel nanoparticles/AnkurPandey Int. Journal of Engineering Research and Applications ISSN : 2248-9622, Vol. 5, Issue 4, 2015, pp.96-100

9. Abdel-AalE .A. ,Malekzadeh S.M., Mohamed M R. , El-Midany A.A., El-Shall H. Effect of synthesis conditions on preparation of nickel metal nanopowders via hydrothermal reduction technique January 2007Powder Technology 171(1):63-68

10. Sulekh C., Avdhesh K., Praveen K., Tomar Synthesis of Ni nanoparticles and their characterizations Journal of Saudi Chemical SocietyVolume 18, Issue 5, November 2014, Pages 437-442

11. Yakymovychb A., Ipser H. Synthesis and Characterization of Pure Ni and Ni-Sn Intermetallic Nanoparticles Nanoscale Research Letters December 2017, 12:142

12. *Liang-Hsing C., Wen-Ching H., Maw-Tien L.* On the Preparation of Nickel Nanoparticles by Chemical Reduction Method: X-ray Absorption Spectroscopy Material Science Vol 22, №2 (2016)

HIGGS BOSON RADIATION IN ARBITRARILY POLARIZED LEPTON-ANTILEPTON COLLISIONS

S.K. ABDULLAYEV, M.Sh. GOJAYEV

Baku State University

Baku / AZERBAIJAN

sabdullayev@bsu.edu.az, m_qocayev@mail.ru

ABSTRACT

In the framework of the Standard Model, the Higgs boson and heavy fermion pair production process in electron-positron or muon-antimuon collisions is considered: $e^- e^+ \to H f \bar{f}$, here $f \bar{f}$ – is the lepton pair ($\tau^- \tau^+$) or quark ($b\bar{b}$, $t\bar{t}$) pair. The mechanism of Higgs boson radiation by a heavy fermion pair is investigated in detail. Taking into account the arbitrarily (longitudinal and transverse) polarizations of the lepton-antilepton pair and the longitudinal polarizations of the heavy fermion pair, analytical expressions for the differential and integral cross sections are obtained. The left-right and transverse spin asymmetries, as well as the degree of longitudinal polarization of the fermion are determined. At the energy of the lepton-antilepton pair $\sqrt{s} = 1$ TeV, the dependence of the effective cross section and asymmetries on the energies and angles of departure was studied.

Keywords: Standard Model, electron-positron, Hiqqs boson, fermion coupling, spirality, spin asymmetry.

İXTİYARİ POLYARLAŞMIŞ LEPTON-ANTİLEPTON TOQQUŞMASINDA HİQQS BOZONUN ŞÜALANMASI

XÜLASƏ

Standart Model çərçivəsində elektron-pozitron və ya müon-antimüon toqquşmasında Hiqqs bozonla ağır fermion-antifermion cütünün yaranması prosesinə baxılmışdır: $e^- e^+ \to H f \bar{f}$, burada $f \bar{f}$ – lepton ($\tau^- \tau^+$) və ya kvark ($b\bar{b}$, $t\bar{t}$) cütüdür. Hiqqs bozonun fermion və antifermion tərəfindən şüalanması mexanizmi ətraflı tədqiq edilmişdir. Lepton-antilepton cütünün ixtiyari (uzununa və eninə), fermion cütünün isə uzununa polyarlaşma hallarını nəzərə almaqla prosesin diferensial və inteqral effektiv kəsikləri üçün ümumi ifadələr alınmışdır. Sol-sağ və eninə spin asimmetriyaları və fermionun uzununa polyarlaşma dərəcəsi təyin edilmişdir. Lepron-antilepton cütünün enerjisinin $\sqrt{s} = 1$ TeV qiymətində effektiv kəsiyin və asimmetriyaların bucaqlara və enerjilərə görə paylanmaları öyrənilmişdir.

Açar sözlər: Standart Model, elektron-pozitron, Hiqqs bozon, ağır fermion cütü, spirallıq, spin asimmetriyası.

ИЗЛУЧЕНИЕ ХИГГС БОЗОНА В ПРОИЗВОЛЬНО ПОЛЯРИЗОВАННЫХ ЛЕПТОН-АНТИЛЕПТОННЫХ СТОЛКНОВЕНИЯХ

РЕЗЮМЕ

В рамках Стандартной Модели рассмотрен процесс рождения Хигтс бозона и тяжелой фермионной пары в электрон-позитронных или мюон-антимюонных столкновениях: $e^- e^+ \to H f \bar{f}$, здесь $f \bar{f}$ – лептонная пара ($\tau^- \tau^+$) или кварковая ($b\bar{b}$, $t\bar{t}$) пара. Подробно исследован механизм излучения Хигтс бозона тяжелой фермионной парой. С учетом произвольных (продольных и поперечных) поляризаций лептон-антилептонной пары и продольных поляризаций тяжелой фермионной пары получены аналитические выражения для дифференциального и интегрального сечений. Определены лево-правая и поперечная спиновые асимметрии, а также степень продольной поляризации фермиона. При энергии лептон-антилептонной пары $\sqrt{s} = 1$ ТэВ изучена зависимость эффективного сечения и асимметрий от энергий и углов вылета.

Ключевые слова: Стандартная модель, электрон-позитрон, Hiqqs bozon, тяжелая фермионная пара, спиральность, спиновая асимметрия.

1. Introduction

The standard model (SM) describes well the physics of strong, electromagnetic, and weak interactions between leptons, quarks, and gauge bosons [1–5]. A doublet of scalar fields $\varphi = \begin{pmatrix} \varphi^+ \\ \varphi^0 \end{pmatrix}$ is introduced into the model, the neutral component of which has a nonzero vacuum value. As a result of spontaneous symmetry breaking due to quantum excitations of the scalar field, a new particle appears - the Higgs scalar boson, and due to the interaction with this field, the gauge bosons, quarks and charged leptons gain mass. This mechanism of mass generation of fundamental particles is known as the Higgs mechanism of spontaneous breakdown of gauge symmetry [6–9].

The discovery of the Higgs boson with characteristics corresponding to the predictions of the SM was carried out by the ATLAS and CMS collaborations at the Large Hadron Collider (LHC) in 2012 [10, 11] (see also the reviews [12-14]). In the first experiments conducted in the LHC, the main properties of this particle were established. The Higgs boson is a scalar particle with spin zero, positive parity, nonzero vacuum value, mass about 125 GeV, interacting with $W^\pm$- and Z^0-bosons with a coupling constant proportional to their masses. With the discovery of the Higgs boson, the SM has entered a new stage in the study of the properties of the fundamental interactions of elementary particles. An accurate measurement of all the coupling constants of this particle with fundamental fermions can be an argument in favor of or a counterbalance to the fact that it is in fact a Higgs boson of the SM. In this connection, interest in various channels of the Higgs boson production and decay has greatly increased [1, 15–29].

Determining the main characteristics of the Higgs boson is the main task of the LHC and future high-energy electron-positron (muon-antimuon) colliders. Collisions of electrons and positrons at high energies is an effective method for studying the mechanisms of interaction of elementary particles. This is mainly due to the following two circumstances. First, the interaction of electrons and positrons is described by the SM, so the results obtained are well interpretable. Secondly, since electrons and positrons do not participate in strong interactions, the background conditions of the experiments are significantly improved compared to studies conducted with hadron beams. The latter circumstance is especially significant when studying processes with small cross sections. We only note that experiments carried out with electron-positron beams at LEP and SLC acceleration centers up to energies of $\sqrt{s} = 209$ GeV in the center-of-mass system played an essential role for precision testing of SM [1, 2].

At present, the construction of a new generation of electron-positron colliders has already been designed [23, 30]. In the future, these colliders will allow us to study the physical properties of the standard Higgs boson.

In [16, 27], we investigated the processes of production of the Higgs boson and a light fermion pair in arbitrarily polarized electron-positron collisions. The joint production of the Higgs boson and the heavy fermion pair was first considered in [31]. Here authors consider the electromagnetic mechanism of the production of a heavy fermion pair and the Higgs boson radiation from the fermion line $e^- + e^+ \rightarrow (\gamma^*) \rightarrow f + \bar{f} + H$. In [32] (see also [33]), in the framework of the SM, the production of the Higgs boson H and the heavy $t\bar{t}$-quark pair $e^- + e^+ \rightarrow (\gamma^*; Z^*) \rightarrow H + t + \bar{t}$ was considered. Here, a cross section is obtained, integrated over the angles of emission of particles and characterizing the distribution of the $t\bar{t}$-quark pair by

energy. In recent works [34, 35], we have considered a process $e^- + e^+ \to (\gamma^*) \to H + f + \bar{f}$ with allowance for arbitrary polarizations of the electron-positron pair and the helicities of heavy fermions.

In this paper, we studied the joint production of a standard Higgs boson and a longitudinally polarized heavy fermion pair in arbitrarily polarized electron-positron collisions in the framework of the SM:

$$e^- + e^+ \to (\gamma^*; Z^*) \to H + f + \bar{f}, \tag{1}$$

where $f\bar{f}$ – may be a lepton ($\tau^-\tau^+$) or quark ($b\bar{b}$, $t\bar{t}$) pair. The differential and integral sections of the process are calculated, and the dependences of the cross sections, angular and spin asymmetries on the energies and angles of emission of particles are studied. The possibilities of measuring the interaction constant g_{Hff} are discussed, which is very important for verifying the Higgs sector of the SM.

2. The square of the matrix element of the process $e^-e^+ \to Hf\bar{f}$

According to the SM, process (1) is described by two types of Feynman diagrams, shown in Fig. 1, where 4-particle momenta are written in parentheses. Of these, diagrams a) and b) correspond to the Higgs boson radiation by a heavy fermion pair, and diagram c) describes the radiation of the Higgs boson by the vector Z^0-boson

Fig. 1. Feynman diagrams of reaction $e^-e^+ \to Hf\bar{f}$
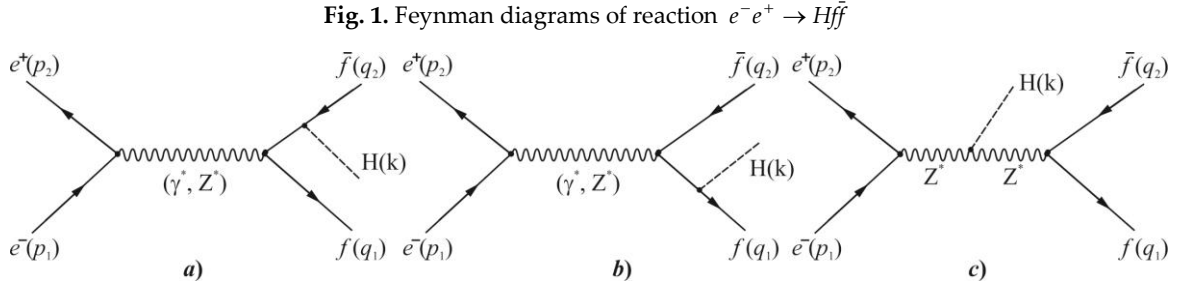
The matrix element corresponding to diagrams a) and b) can be represented as (diagram c) was studied in detail in [16], therefore, it is not considered here):

$$M_{i \to f} = M_{i \to f}^{(\gamma)} + M_{i \to f}^{(Z)}, \tag{2}$$

$$M_{i \to f}^{(\gamma)} = \frac{ie^2 Q_f}{s} g_{Hff} \cdot \ell_\mu^{(\gamma)} \cdot J_\mu^{(\gamma)}, \tag{3}$$

$$M_{i \to f}^{(Z)} = ie^2 D_Z(s) g_{Hff} \cdot \ell_\mu^{(Z)} \cdot J_\mu^{(Z)}. \tag{4}$$

Here Q_f -is the electric charge of the fermion in units of elementary charge e, $g_{Hff} = m_f/\eta$ – is the constant of interaction of the fermion with the Higgs boson, $\eta = 246$ GeV is the vacuum value of the Higgs boson field, $s = (p_1 + p_2)^2$ – is the square of the total energy e^-e^+ -pairs in the center-of-mass system, m_f – is the mass of the fermion, $D_Z(s) = (s - M_Z^2)^{-1}$, M_Z – mass of Z^0 -boson,

$$\ell_\mu^{(\gamma)} = \bar{\upsilon}_e(p_2)\gamma_\mu u_e(p_1), \qquad \ell_\mu^{(Z)} = \bar{\upsilon}_e(p_2)\gamma_\mu[g_V(e) + \gamma_5 g_A(e)]u_e(p_1), \tag{5}$$

$$J_\mu^{(\gamma)} = \bar{u}_f(q_1)\left[\frac{\hat{q}_1 + \hat{k} + m_f}{(q_1+k)^2 - m_f^2}\gamma_\mu - \gamma_\mu\frac{\hat{q}_2 + \hat{k} - m_f}{(q_2+k)^2 - m_f^2}\right]\upsilon_f(q_2),$$

$$J_\mu^{(Z)} = \bar{u}_f(q_1)\left\{\frac{\hat{q}_1 + \hat{k} + m_f}{(q_1+k)^2 - m_f^2}\gamma_\mu[g_V(f) + \gamma_5 g_A(f)] - \gamma_\mu[g_V(f) + \gamma_5 g_A(f)]\frac{\hat{q}_2 + \hat{k} - m_f}{(q_2+k)^2 - m_f^2}\right\}\upsilon_f(q_2),$$

(6)

– electromagnetic and weak currents $e^- e^+$- and $f\bar{f}$-pairs; $g_V(e)$ and $g_A(e)$ ($g_V(f)$ and $g_A(f)$) is the vector and axial-vector coupling constants of the electron (fermion) with the Z^0-boson

$$g_V(e) = \frac{-\frac{1}{2} + 2x_W}{2\sqrt{x_W(1-x_W)}}, \quad g_A(e) = \frac{-\frac{1}{2}}{2\sqrt{x_W(1-x_W)}},$$

$$g_V(f) = \frac{I_3(f) - 2Q_f x_W}{2\sqrt{x_W(1-x_W)}}, \quad g_A(f) = \frac{I_3(f)}{2\sqrt{x_W(1-x_W)}},$$

(7)

$I_3(f) = \pm 1/2$ – the third projection of the weak isospin of the fermion f; $x_W = \sin^2\theta_W$ – the Weinberg parameter.

The square of the matrix element (2) is expressed by the formula

$$\left|M_{i\to f}\right|^2 = \frac{e^4}{s^2}g_{Hff}^2[Q_f^2 L_{\mu\nu}^{(\gamma)} \cdot H_{\mu\nu}^{(\gamma)} - 2Q_f X_Z L_{\mu\nu}^{(i)} \cdot H_{\mu\nu}^{(i)} + X_Z^2 L_{\mu\nu}^{(Z)} \cdot H_{\mu\nu}^{(Z)}],$$

(8)

Where $X_Z = (1 - r_Z)^{-1}$, $r_Z = M_Z^2/s$, $L_{\mu\nu}^{(\gamma)}$ ($H_{\mu\nu}^{(\gamma)}$), $L_{\mu\nu}^{(Z)}$ ($H_{\mu\nu}^{(Z)}$) and $L_{\mu\nu}^{(i)}$ ($H_{\mu\nu}^{(i)}$) – are the electromagnetic, weak, and interference tensors of the electron-positron (heavy fermion) pair. All lepton tensors are preserved:

$$L_{\mu\nu}^{(a)} \cdot p_\mu = L_{\mu\nu}^{(a)} \cdot p_\nu = 0 \; (a = \gamma; i; Z).$$

Due to this, in the center of mass system, only the spatial components of these tensors contribute to the cross section

$$L_{\mu\nu}^{(a)} \cdot H_{\mu\nu}^{(a)} = L_{mr}^{(a)} \cdot H_{mr}^{(a)} \quad (m, r = 1, 2, 3).$$

Tensors $L_{mr}^{(a)}$ are easily calculated on the basis of currents $\ell_\mu^{(\gamma)}$ and $\ell_\mu^{(Z)}$, and in the case of the annihilation of arbitrarily polarized $e^- e^+$-pairs have the following structure [36, 37]:

$$L_{mr}^{(\gamma)} = \ell_m^{(\gamma)}\ell_r^{*(\gamma)} =$$

$$= \frac{s}{2}[(1 - \lambda_1\lambda_2)(\delta_{mr} - N_m N_r) + (\lambda_2 - \lambda_1)i\varepsilon_{mrs}N_s + (\vec{\eta}_1\vec{\eta}_2)(\delta_{mr} - N_m N_r) - \eta_{1m}\eta_{2r} - \eta_{1r}\eta_{2m}],$$

$$L_{mr}^{(i)} = \ell_m^{(\gamma)}\ell_r^{*(Z)} = g_V(e)L_{mr}^{(\gamma)} + \frac{s}{2}g_A(e)[(\lambda_2 - \lambda_1)(\delta_{mr} - N_m N_r) + (1 - \lambda_1\lambda_2)i\varepsilon_{mrs}N_s],$$

(9)

$$L_{mr}^{(Z)} = \ell_m^{(Z)}\ell_r^{*(Z)} = [g_V^2(e) + g_A^2(e)]L_{mr}^{(\gamma)} + \frac{s}{2}\cdot 2g_V(e)g_A(e)[(\lambda_2 - \lambda_1)(\delta_{mr} - N_m N_r) +$$

$$+ (1 - \lambda_1\lambda_2)i\varepsilon_{mrs}N_s] - sg_A^2(e)[(\vec{\eta}_1\vec{\eta}_2)(\delta_{mr} - N_m N_r) - \eta_{1m}\eta_{2r} - \eta_{1r}\eta_{2m}],$$

where λ_1 and λ_2 ($\vec{\eta}_1$ and $\vec{\eta}_2$) – is the helicity (transverse components of the spin vectors) of the electron and positron, $\vec{N}$ – is the unit vector directed along the electron momentum.

From the expressions of lepton tensors, it follows that in the case of annihilation of longitudinally polarized $e^- e^+$-pairs the helicity of the electron and positron must be opposite

$- \lambda_1 = -\lambda_2 = \pm 1$ (the electron is right, and the positron is left $- e_R^- e_L^+$ or electron is left, and the positron is right $- e_L^- e_R^+$). This is due to the law of conservation of the total moment in the transitions $e^- + e^+ \to \gamma*$ and $e^- + e^+ \to Z*$.

As for the fermionic tensors $H_{mr}^{(a)}$, we note that, in general, they have a cumbersome expressions and therefore are not given here. However, at high energies of colliding electron-positron pairs ($\sqrt{s} \geq 1$ TeV), the rations $\dfrac{m_f^2}{s}$ and $\dfrac{M_H^2}{s}$ can be neglected (for example, for the heaviest t-quark at $\sqrt{s} = 1$ TeV, this ratio is $\left(\dfrac{173.2}{1000}\right)^2 = 0.03 \ll 1$). Then neglecting the terms proportional $\dfrac{m_f^2}{s}$ and $\dfrac{M_H^2}{s}$, for fermionic tensors, we have expressions (we assume that the heavy fermion pair is polarized longitudinally):

$$H_{mr}^{(\gamma)} = J_m^{(\gamma)} J_r^{*(\gamma)} = \frac{x_H^2}{2(1-x_1)(1-x_2)}[(1+h_1 h_2)(\delta_{mr} - n_m n_r) + (h_1 + h_2)i\varepsilon_{mrq}n_q],$$

$$H_{mr}^{(i)} = J_m^{(\gamma)} J_r^{*(Z)} =$$

$$= g_V(f)H_{mr}^{(\gamma)} + \frac{1}{4}g_A(f)(1+h_1 h_2)\cdot x_H \cdot i\varepsilon_{mrq}\left[\frac{x_2}{1-x_2}(n_{2q} - n_q) - \frac{x_1}{1-x_1}(n_{1q} - n_q)\right] +$$

$$+ \frac{1}{4}g_A(f)(h_1 + h_2)\left\{\frac{1}{1-x_2}[x_H x_2(n_m n_{2r} + n_r n_{2m}) + 2(1-x_1)\delta_{mr}] -\right.$$

$$\left. - \frac{1}{1-x_1}[x_H x_1(n_m n_{1r} + n_r n_{1m}) + 2(1-x_2)\delta_{mr}]\right\}. \qquad (10)$$

$$H_{mr}^{(Z)} = J_m^{(Z)} J_r^{*(Z)} = [g_V^2(f) + g_A^2(f)]H_{mr}^{(\gamma)} - g_A^2(f)(1+h_1 h_2)(1+x_H)(\delta_{mr} - n_m n_r) -$$

$$- \frac{1}{2}\cdot g_A^2(f)(h_1 + h_2)x_H i\varepsilon_{mrq}\left[\frac{x_2}{1-x_1}(n_{2q} - n_q) - \frac{x_1}{1-x_2}(n_{1q} - n_q)\right] +$$

$$+ \frac{1}{2}g_V(f)g_A(f)(1+h_1 h_2)x_H i\varepsilon_{mrq}\left[\frac{x_2}{1-x_2}(n_{2q} - n_q) - \frac{x_1}{1-x_1}(n_{1q} - n_q)\right] +$$

$$+ \frac{1}{2}g_V(f)g_A(f)(h_1 + h_2)\left\{\frac{1}{1-x_2}[x_H x_2(n_m n_{2r} + n_r n_{2m}) + 2(1-x_1)\delta_{mr}] -\right.$$

$$\left. - \frac{1}{1-x_1}[x_H x_1(n_m n_{1r} + n_r n_{1m}) + 2(1-x_2)\delta_{mr}]\right\}.$$

Here h_1 and h_2 – are the helicities of the fermion and antifermion, $x_1 = \dfrac{2E_1}{\sqrt{s}}$, $x_2 = \dfrac{2E_2}{\sqrt{s}}$ and $x_H = \dfrac{2E_H}{\sqrt{s}} = 2 - x_1 - x_2$ – are the scaling energies of the fermion, antifermion and Higgs boson, respectively, $\vec{n}$, $\vec{n}_1$ and $\vec{n}_2$ – are the unit vectors along the Higgs boson, fermion and antifermion momentum.

From the fermionic tensors (9) it can be seen that, in contrast to the helicity of the electron-positron pair, the helicity of the fermion and the antifermion must be the same $h_1 = h_2 = \pm 1$ (the fermion and the antifermion are right $- f_R \bar{f}_R$ or left $- f_L \bar{f}_L$ handed).

We use a coordinate system in which the OXZ plane coincides with the particle production plane $\vec{q}_1 + \vec{q}_2 + \vec{k} = 0$, and we introduce angles θ, χ and φ, where θ – is the polar angle between the Z axis and the direction of the electron beam, χ – is the azimuth angle between the birth plane and the plane defined by the Z axis and the electron beam, φ – the azimuth angle between the planes of birth and transverse polarization of the electron.

We introduce the so-called correlation functions $\sigma_k \, (k = 1 \div 9)$, by means of the relations:

$$\sigma_1 = H_{11}^{(S)} + H_{22}^{(S)}, \qquad \sigma_2 = \frac{1}{2}(H_{22}^{(S)} - H_{11}^{(S)}), \quad \sigma_3 = H_{33}^{(S)},$$

$$\sigma_4 = \frac{1}{2}(H_{13}^{(S)} + H_{31}^{(S)}), \quad \sigma_5 = \frac{1}{2}(H_{23}^{(S)} + H_{32}^{(S)}), \quad \sigma_6 = \frac{1}{2}(H_{12}^{(S)} + H_{21}^{(S)}), \tag{11}$$

$$\sigma_7 = i(H_{12}^{(A)} - H_{21}^{(A)}), \quad \sigma_8 = \frac{i}{2}(H_{23}^{(A)} - H_{32}^{(A)}), \quad \sigma_9 = \frac{i}{2}(H_{31}^{(A)} - H_{13}^{(A)}).$$

Here $H_{mr}^{(S)}$ – is the symmetric, and $H_{mr}^{(A)}$ – is the antisymmetric part of the tensors. Then the product of the electron-positron and fermionic tensors can be represented as:

$$L_{mr}^{(S)} \cdot H_{mr}^{(S)} = \frac{1}{2}(L_{11}^{(S)} + L_{22}^{(S)}) \cdot \sigma_1 + (L_{22}^{(S)} - L_{11}^{(S)}) \cdot \sigma_2 + L_{33}^{(S)} \cdot \sigma_3 + (L_{13}^{(S)} + L_{31}^{(S)}) \cdot \sigma_4 +$$

$$+ (L_{23}^{(S)} + L_{32}^{(S)}) \cdot \sigma_5 + (L_{12}^{(S)} + L_{21}^{(S)}) \cdot \sigma_6, \tag{12}$$

$$L_{mr}^{(A)} \cdot H_{mr}^{(A)} = -\frac{i}{2}(L_{12}^{(A)} - L_{21}^{(A)}) \cdot \sigma_7 - i(L_{23}^{(A)} - L_{32}^{(A)}) \cdot \sigma_8 - i(L_{31}^{(A)} - L_{13}^{(A)}) \cdot \sigma_9,$$

where $L_{mr}^{(S)}$ and $L_{mr}^{(A)}$ – are the symmetric and antisymmetric parts of the lepton tensors.

3. Angular distribution of particles in the reaction $e^- e^+ \to H f \bar{f}$

First, consider the angular distribution of particles θ and χ in the case of unpolarized particles. In this case, for the differential cross section of the reaction (1), the expression

$$\frac{d^4\sigma}{d\chi d(\cos\theta) dx_1 dx_2} = \frac{\alpha_{\text{QED}}^2 N_C}{128\pi^2 s} g_{Hff}^2 [G_A \cdot \sigma_A + G_B \cdot \sigma_B + G_C \cdot \sigma_C]. \tag{13}$$

Here N_C – is the color factor (in the case of the production of a lepton pair $\tau^- \tau^+$ $N_C = 1$, and in the case of the production of a quark pair $b\bar{b}$ or $t\bar{t}$ $N_C = 3$), the notation

$$G_A = Q_f^2 - 2Q_f g_V(e) g_V(f) X_Z + [g_V^2(e) + g_A^2(e)][g_V^2(f) + g_A^2(f)] X_Z^2,$$

$$G_B = 2g_A(e) g_A(f)[-Q_f + 2g_V(e) g_V(f) X_Z] X_Z, \tag{14}$$

$$G_C = [g_V^2(e) + g_A^2(e)] g_A^2(f) X_Z^2,$$

$$\sigma_A = \frac{1}{2}(1 + \cos^2\theta) \cdot \sigma_1 + \sin^2\theta(\cos 2\chi \cdot \sigma_2 + \sigma_3 + \sin 2\chi \cdot \sigma_4) + \sin 2\theta(\sin\chi \cdot \sigma_5 + \cos\chi \cdot \sigma_6),$$

$$\sigma_B = \cos\theta \cdot \sigma_7 + 2\sin\theta(\cos\chi \cdot \sigma_8 + \sin\chi \cdot \sigma_9), \tag{15}$$

$$\sigma_C = \frac{1}{2}(1 + \cos^2\theta) \cdot \sigma_1' + \sin^2\theta(\cos 2\chi \cdot \sigma_2' + \sigma_3' + \sin 2\chi \cdot \sigma_4') + \sin 2\theta(\sin\chi \cdot \sigma_5' + \cos\chi \cdot \sigma_6').$$

Correlation functions σ_k and σ_k', entering in (15), depend on scaling energies x_1 and x_2 ($x_H = 2 - x_1 - x_2$) and they are easily determined on the basis of fermionic tensors (10):

$$\sigma_1 = \frac{2x_H^2}{(1-x_1)(1-x_2)}(2-n_x^2), \qquad \sigma_2 = \frac{x_H^2}{(1-x_1)(1-x_2)}n_x^2,$$

$$\sigma_3 = \frac{2x_H^2}{(1-x_1)(1-x_2)}(1-n_z^2), \qquad \sigma_4 = -\frac{2x_H^2}{(1-x_1)(1-x_2)}\cdot n_x n_z,$$

$$\sigma_7 = 2x_H\left[\frac{x_2}{1-x_2}(n_z - n_{2z}) - \frac{x_1}{1-x_1}(n_z - n_{1z})\right], \quad \sigma_8 = x_H\left[\frac{x_2}{1-x_2}(n_x - n_{2x}) - \frac{x_1}{1-x_1}(n_x - n_{1x})\right],$$

$$\sigma_5 = \sigma_6 = \sigma_9 = 0. \tag{16}$$

$$\sigma_1' = -4(1+x_H)(2-n_x^2), \quad \sigma_2' = -2(1+x_H)n_x^2,$$
$$\sigma_3' = -4(1+x_H)(2-n_z^2), \quad \sigma_4' = 4(1+x_H)n_x n_z, \qquad \sigma_5' = \sigma_6' = 0.$$

As can be seen, due to the orthogonality of the Y axis to the particle production plane, the correlation functions σ_5, σ_6, σ_9, σ_5' and σ_6' vanish.

The distribution of particles in the Dalitz diagram is determined by the laws of conservation of energy and momentum:

$$x_1 + x_2 + x_H = 2, \quad x_1\vec{n}_1 + x_2\vec{n}_2 + x_H\vec{n} = 0.$$

The boundaries of the allowed area of the Dalitz diagram are determined by the equations

$$x_k = |x_i \pm x_j| \quad (i \neq j \neq k)$$

and lines $x_1 = x_2$, $x_1 = x_H$ and $x_2 = x_H$ divide this diagram into six different areas. In the region of $(i; j)$ the scaling energies of the particles x_i and x_j satisfy the conditions

$$x_i \geq x_j \geq x_k \quad (i \neq j \neq k).$$

We can direct the axis Z along the impulse of the most energetic particle and choose an X axis so that the x-th projection of the impulse of the second more energetic particle becomes positive. Then the following areas of the Dalitz diagram are obtained:

Ib(1; 3): $\vec{n}_1 = (0, 0, 1)$, $\vec{n}_2 = (-s_{12}, 0, c_{12})$, $\vec{n} = (s_{13}, 0, c_{13})$;

Ib(1; 2): $\vec{n}_1 = (0, 0, 1)$, $\vec{n}_2 = (s_{12}, 0, c_{12})$, $\vec{n} = (-s_{13}, 0, c_{13})$;

IIa(2; 3): $\vec{n}_2 = (0, 0, 1)$, $\vec{n}_1 = (-s_{21}, 0, c_{21})$, $\vec{n} = (s_{23}, 0, c_{23})$.

IIb(2; 1): $\vec{n}_2 = (0, 0, 1)$, $\vec{n}_1 = (s_{21}, 0, c_{21})$, $\vec{n} = (-s_{23}, 0, c_{23})$;

IIIa(3; 1): $\vec{n}_1 = (0, 0, 1)$, $\vec{n}_1 = (s_{31}, 0, c_{31})$, $\vec{n}_2 = (-s_{32}, 0, c_{32})$.

IIIb(3; 2): $\vec{n} = (0, 0, 1)$, $\vec{n}_1 = (-s_{31}, 0, c_{31})$, $\vec{n}_2 = (s_{32}, 0, c_{32})$.

Note that in region Ia (1; 3), the axis Z is directed along the impulse of the more energetic fermion, and the impulse of the second energetic Higgs boson has a positive x-projection (see Fig. 2a).

Here, the notation $s_{ij} = \sin\theta_{ij}$ and $c_{ij} = \cos\theta_{ij}$, where θ_{ij} – the angle between the directions of the particle momenta i and j. These angles depend on the scaling energies of the particles

$$\sin\theta_{ij} = \frac{2\sqrt{(1-x_1)(1-x_2)(1-x_H)}}{x_i x_j}, \quad \cos\theta_{ij} = 1 - \frac{2(x_i + x_j - 1)}{x_i x_j}. \tag{17}$$

Fig. 2. Coordinate systems Ia, IIa and IIIa.
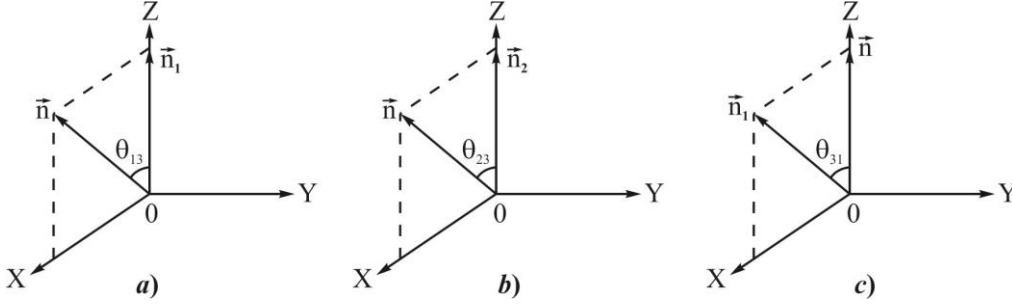
Using these expressions, it is easy to determine the correlation functions in each area of the Dalitz diagram. Here we present the correlation functions in the coordinate systems Ia and Ib (the upper sign corresponds to the system Ia, and the lower sign to the system Ib):

$$\sigma_1 = \frac{2x_H^2}{(1-x_1)(1-x_2)}(2 - s_{13}^2), \quad \sigma_2 = \frac{x_H^2}{(1-x_1)(1-x_2)}s_{13}^2,$$

$$\sigma_3 = \frac{2x_H^2}{(1-x_1)(1-x_2)}(1 - c_{13}^2), \quad \sigma_4 = \mp\frac{2x_H^2}{(1-x_1)(1-x_2)}\cdot s_{13}c_{13}, \tag{18}$$

$$\sigma_7 = 2x_H\left[\frac{x_2}{1-x_2}(c_{13} - c_{12}) + \frac{x_1}{1-x_1}(1 - c_{13})\right], \quad \sigma_8 = x_H\left[\frac{x_2}{1-x_2}(s_{13} + s_{12}) - \frac{x_1}{1-x_1}s_{13}\right],$$

$$\sigma_1' = -4(1+x_H)(2-s_{13}^2), \quad \sigma_2' = -2(1+x_H)s_{13}^2,$$

$$\sigma_3' = -4(1+x_H)(1-c_{13}^2), \quad \sigma_4' = \mp4(1+x_H)s_{13}c_{13}, \qquad \sigma_5' = \sigma_6' = 0.$$

Expressions of correlation functions in the coordinate systems IIa, b and IIIa, b are given in the Appendix.

The angular distributions of particles are:

$$\frac{d^4\sigma}{d\chi d(\cos\theta)dx_1 dx_2} = \frac{\alpha_{\text{QED}}^2 N_C}{128\pi^2 s}g_{Hff}^2 G_A(\sigma_1 + 2\sigma_3)(1+\alpha_0)[1 + \alpha_1\cos^2\theta +$$

$$+ \alpha_2\sin^2\theta\cos 2\chi + \alpha_4\sin^2\theta\sin 2\chi + \alpha_7\cos\theta + \alpha_8\sin\theta\cos\chi]. \tag{19}$$

Here the coefficients of angular distributions of particles are introduced:

$$\alpha_0 = \frac{G_C}{G_A}\cdot\frac{\sigma_1' + 2\sigma_3'}{\sigma_1 + 2\sigma_3}, \qquad\qquad \alpha_1 = \frac{1}{1+\alpha_0}\cdot\left[\frac{\sigma_1 - 2\sigma_3}{\sigma_1 + 2\sigma_3} + \frac{G_C}{G_A}\cdot\frac{\sigma_1' - 2\sigma_3'}{\sigma_1 + 2\sigma_3}\right],$$

$$\alpha_2 = \frac{1}{1+\alpha_0}\cdot\left[\frac{2\sigma_2}{\sigma_1 + 2\sigma_3} + \frac{G_C}{G_A}\cdot\frac{2\sigma_2'}{\sigma_1 + 2\sigma_3}\right], \quad \alpha_4 = \frac{1}{1+\alpha_0}\cdot\left[\frac{2\sigma_4}{\sigma_1 + 2\sigma_3} + \frac{G_C}{G_A}\cdot\frac{2\sigma_4'}{\sigma_1 + 2\sigma_3}\right], \tag{20}$$

$$\alpha_7 = \frac{1}{1+\alpha_0}\cdot\frac{G_B}{G_A}\cdot\frac{2\sigma_7}{\sigma_1 + 2\sigma_3}, \qquad\qquad \alpha_8 = \frac{1}{1+\alpha_0}\cdot\frac{G_B}{G_A}\cdot\frac{4\sigma_8}{\sigma_1 + 2\sigma_3}.$$

We present estimates of the coefficients of the angular distributions of particles α_k ($k = 1$, 2, 4, 7, 8) in the coordinate system Ia (1; 3), where these coefficients have the form

$$\alpha_0 = -\frac{G_C}{G_A} \cdot \frac{2}{x_H^2}(1+x_H)(1-x_1)(1-x_2), \quad \alpha_1 = \frac{3c_{13}^2-1}{3-c_{13}^2} \cdot \frac{1-\alpha_0}{1+\alpha_0},$$

$$\alpha_2 = \frac{s_{13}^2}{3-c_{13}^2} \cdot \frac{1-\alpha_0}{1+\alpha_0}, \qquad \alpha_4 = -\frac{2s_{13}c_{13}}{3-c_{13}^2} \cdot \frac{1-\alpha_0}{1+\alpha_0},$$

$$\alpha_7 = \frac{G_B}{G_A}\frac{1}{1+\alpha_0}\frac{2[x_2(1-x_1)(c_{13}-c_{12})+x_1(1-x_2)(1-c_{13})]}{x_H(3-c_{13}^2)}, \qquad (21)$$

$$\alpha_8 = \frac{G_B}{G_A}\frac{1}{1+\alpha_0}\frac{2[x_2(1-x_1)(s_{13}+s_{12})-x_1(1-x_2)s_{13}]}{x_H(3-c_{13}^2)}.$$

The results of estimates of the coefficients of angular distributions are presented in Fig. 3, which illustrates the dependence of the coefficients α_k ($k = 1, 2, 4, 7, 8$) on the variable x_2 at a fixed scaling energy $x_1 = 0.9$ in the reaction $e^- + e^+ \to H + \tau^- + \tau^+$. As can be seen, the coefficient α_1 (α_8) at the beginning of the energy spectrum is positive (negative) and monotonously decreases (increases) with increasing energy x_2, takes negative (positive) values at the end of the energy spectrum. The coefficients of the angular distributions α_2, α_4 and α_7 positive, with increasing energy x_2, the coefficient α_2 increases, and the coefficients α_4 and α_7 decreases.

Fig. 3. The dependence of the angular distributions coefficients on x_2 in the reaction $e^-e^+ \to H\tau^-\tau^+$
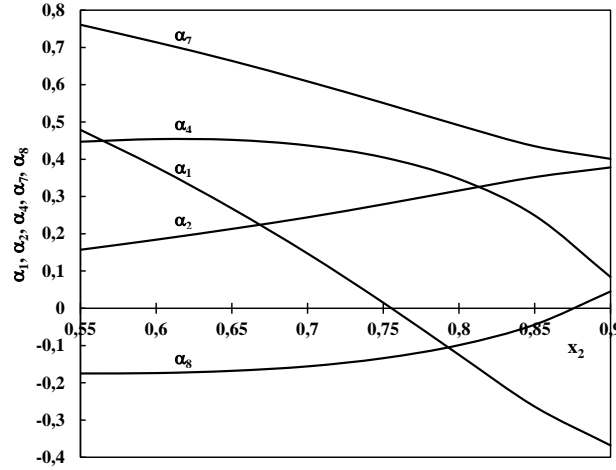
4. Left-right and transverse spin asymmetries and the degree of longitudinal polarization of the fermion

When annihilating electron-positron pair a longitudinally polarized, the differential cross section of reaction (1), integrated over the angles θ and χ, can be represented as:

$$\frac{d^2\sigma(\lambda_1,\lambda_2)}{dx_1 dx_2} = \frac{d^2\sigma_0}{dx_1 dx_2}[1-\lambda_1\lambda_2+(\lambda_2-\lambda_1)A_{LR}]. \qquad (22)$$

Here

$$\frac{d^2\sigma_0}{dx_1 dx_2} = \frac{\alpha_{QED}^2 N_C}{12\pi s}g_{Hff}^2\left\{G_A\frac{x_H^2}{(1-x_1)(1-x_2)}-2[g_V^2(e)+g_A^2(e)]g_A^2(f)(1+x_H)X_Z^2\right\} \qquad (23)$$

– differential cross section of this process in the case of unpolarized particles, and

$$A_{LR} = \frac{G_D x_H^2 - 4g_V(e)g_A(e)g_A^2(f)(1+x_H)(1-x_1)(1-x_2)X_Z^2}{G_D x_H^2 - 2[g_V^2(e)+g_A^2(e)]g_A^2(f)(1+x_H)(1-x_1)(1-x_2)X_Z^2} \qquad (24)$$

– the left-right spin asymmetry due to the longitudinal polarization of the electron and the designation introduced

$$G_D = 2Q_e Q_f g_A(e)g_V(f)X_Z + 2g_V(e)g_A(e)[g_V^2(f)+g_A^2(f)]X_Z^2 .$$

The left-right spin asymmetry A_{LR} in the process $e^- + e^+ \to H + \tau^- + \tau^+$ at $x_2 = 0.9$ about 5.1% and slightly increases with growth x_1, remaining almost constant. The same character is the left-right spin asymmetry in the process $e^- + e^+ \to H + t + \bar{t}$. However, in this process $e^- + e^+ \to H + \tau^- + \tau^+$, the left-right spin asymmetry is almost three times greater than in the process.

Due to the weak interaction in the process $e^- + e^+ \to H + f + \bar{f}$ under consideration, fermion and antifermion can be produced longitudinally polarized. Taking into account the longitudinal polarizations of the heavy fermion pair, the differential cross section integrated over the emission angles is:

$$\frac{d^2\sigma(h_1,h_2)}{dx_1 dx_2} = \frac{1}{4} \cdot \frac{d^2\sigma_0}{dx_1 dx_2}[1+h_1 h_2 +(h_1+h_2)P_f] . \qquad (25)$$

Here

$$\begin{aligned} P_f = &\{-Q_f g_V(e)g_A(e)X_Z +[g_V^2(e)+g_A^2(e)]g_V(f)g_A(f)X_Z^2\} \times \\ &\times \{(1-x_1)[x_H x_2 c_{13} + 3(1-x_1)] - (1-x_2)[x_H x_1(c_{13}c_{12}-s_{13}s_{12})+3(1-x_2)]\} \times . \\ &\times \{G_A x_H^2 - 2(1-x_1)(1-x_2)[g_V^2(e)+g_A^2(e)]g_A^2(f)(1+x_H)X_Z^2\}^{-1} \end{aligned} \qquad (26)$$

– the degree of longitudinal polarization of the fermion or antifermion in the coordinate system Ia.

The degree of longitudinal polarization (20) is convenient to investigate in the process $e^- + e^+ \to H + \tau^- + \tau^+$, since decay widths $\tau^- \to \pi^- + \nu_\tau$, $\tau^- \to K^- + \nu_\tau$ and $\tau^- \to \rho^- + \nu_\tau$ are sensitive to τ-lepton polarization and exploring these decay channels it is possible to experimentally measure its degree of longitudinal polarization.

In fig. 4 illustrates the dependence of the degree of longitudinal polarization of a τ-lepton on a variable x_1 with a fixed $x_2 = 0.9$ and $x_2 = 0.95$. With an increase in the scaling energy x_1, the degree of longitudinal polarization of the τ-lepton monotonously decreases, and an increase in energy x_2 with a fixed x_1 one leads to an increase in the degree of longitudinal polarization.

Now consider the distribution of particles in the angles θ and φ. In this case, the annihilation cross section of the transversely polarized electron-positron pair, integrated over the azimuth angle χ, has the form:

Fig. 4. Energy dependence of the degree of longitudinal polarization P_f in the process $e^- e^+ \to H \tau^- \tau^+$.
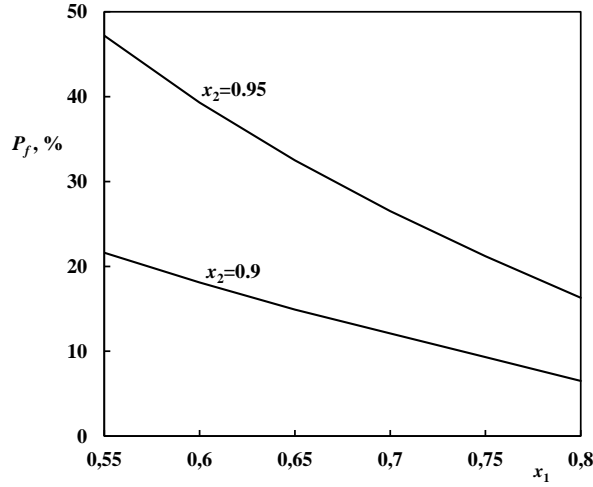
$$\frac{d^4\sigma(\eta_1,\eta_2)}{d\varphi d(\cos\theta)dx_1 dx_2} = \frac{d^4\sigma_0}{d\varphi d(\cos\theta)dx_1 dx_2}[1 + A_\perp \eta_1 \eta_2 \cos 2\varphi], \quad (27)$$

where

$$\frac{d^4\sigma_0}{d\varphi d(\cos\theta)dx_1 dx_2} = \frac{\alpha_{QED}^2 N_C}{128\pi^2 s} g_{Hff}^2 G_A (\sigma_1 + 2\sigma_3)(1+\alpha_0)(1+\alpha_1 \cos^2\theta) \quad (28)$$

– differential cross section of this process in the case of unpolarized particles,

$$A_\perp = \frac{\beta_1 \sin^2\theta}{1 + \beta_1 \cos^2\theta} \cdot \frac{F_B}{F_A} \quad (29)$$

– transverse spin asymmetry due to transverse polarizations of the electron-positron pair. The notation is entered here:

$$\beta_1 = \frac{\sigma_1 - 2\sigma_3}{\sigma_1 + 2\sigma_3},$$

$$F_A = G_A \frac{x_H^2}{2(1-x_1)(1-x_2)} - [g_V^2(e) + g_A^2(e)]g_A^2(f)(1+x_H)X_Z^2, \quad (30)$$

$$F_B = \frac{x_H^2}{2(1-x_1)(1-x_2)}\{Q_e^2 Q_f^2 + 2Q_e Q_f X_Z g_V(e)g_V(f) + X_Z^2[g_V^2(e) - g_A^2(e)][g_V^2(f) + g_A^2(f)]\} -$$

$$- X_Z^2[g_V^2(e) - g_A^2(e)]g_A^2(f)(1 + x_H),$$

In fig. 5 illustrates the angular dependence of the transverse spin asymmetry (29) in the process $e^- + e^+ \to H + \tau^- + \tau^+$ with $x_1 = 0.95$ and three values of the variable $x_2 = 0.55$, 0.6 and 0.65.

With an increase in the angle θ, the transverse spin asymmetry increases and reaches a maximum at an angle of $\theta = 90°$, a further increase in the angle θ leads to a decrease in the transverse spin asymmetry, at the end of the angular spectrum the transverse spin asymmetry vanishes. An increase in energy x_2 leads to a decrease in transverse spin asymmetry.

Fig. 5. Dependence of the transverse spin asymmetry on the angle θ in the reaction $e^- e^+ \to H\tau^- \tau^+$
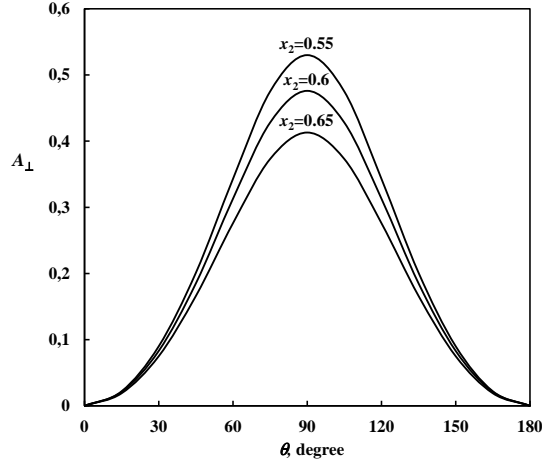
5. The distribution of particles in a variable T

The distribution of fermion and antifermion in variables x_1 and x_2 is expressed by the formula:

$$\frac{d^2\sigma_0}{dx_1 dx_2} = \frac{\alpha_{\text{QED}}^2 N_C}{12\pi s} g_{Hff}^2 \left\{ G_A \left[2 + \frac{1-x_1}{1-x_2} + \frac{1-x_2}{1-x_1} \right] - 2[g_V^2(e) + g_A^2(e)] g_A^2(f)(1+x_H) X_Z^2 \right\}. \tag{31}$$

We introduce new variables $T = \max(x_1, x_2, x_H)$, T_1 and T_2 so that inequalities $T \geq T_1 \geq T_2 = 2 - T - T_2$ are satisfied. We direct the axis Z along the impulse of the most energetic particle and integrate the section in a variable T_1 with a fixed T one. Then we get the results below:

1) at $x_H = T$ and $x_1 = T_1$ (or $x_2 = T_1$)

$$\frac{d\sigma}{dT} = \frac{\alpha_{\text{QED}}^2 N_C}{12\pi s} g_{Hff}^2 \left\{ G_A T \ln\left(\frac{1-T}{T}\right) - \frac{1}{4}[g_V^2(e) + g_A^2(e)] g_A^2(f)(1+x_H) X_Z^2 (12 - 5T)(3T - 2) \right\}; \tag{32}$$

2) at $x_1 = T$ and $x_2 = T_1$ (or at $x_2 = T$ and $x_1 = T_1$):

$$\frac{d\sigma}{dT} = \frac{\alpha_{\text{QED}}^2 N_C}{12\pi s} g_{Hff}^2 \left\{ G_A \left[\frac{(3T-2)(6-5T)}{2(1-T)} - (1-T)\ln\left(\frac{2T-1}{1-T}\right) \right] - \right.$$
$$\left. - \frac{1}{4}[g_V^2(e) + g_A^2(e)] g_A^2(f) X_Z^2 (12 - 5T)(3T - 2) \right\}; \tag{33}$$

3) at $x_1 = T$ and $x_H = T_1$ (or at $x_2 = T$ and $x_H = T_1$)

$$\frac{d\sigma}{dT} = \frac{\alpha_{\text{QED}}^2 N_C}{12\pi s} g_{Hff}^2 \left\{ G_A \left[\frac{(3T-2)(2-T)}{2(1-T)} + (1-T)\ln\left(\frac{2T-1}{1-T}\right) \right] - \right.$$
$$\left. - \frac{1}{4}[g_V^2(e) + g_A^2(e)] g_A^2(f) X_Z^2 (12 - 5T)(3T - 2) \right\}; \tag{34}$$

By adding the contributions to the cross section of individual regions of the Dalitz diagram, we obtain a cross section characterizing the distribution of the most energetic particle on a variable T:

$$\frac{d\sigma}{dT} = \frac{\alpha_{\text{QED}}^2 N_C}{12\pi s} g_{Hff}^2 \left\{ G_A \left[\frac{(3T-2)(4-3T)}{(1-T)} + \ln\left(\frac{2T-1}{T} \right) \right] - \right.$$

$$\left. - \frac{3}{4} [g_V^2(e) + g_A^2(e)] g_A^2(f) X_Z^2 (12-5T)(3T-2) \right\}.$$

(35)

In Fig. 6 shows the dependence of cross section of the reaction $e^- + e^+ \to H + t + \bar{t}$ on the variable T at $\sqrt{s} = 1$ TeV and $m_t = 173.2$ GeV. The growth of a variable T from 0.725 to 0.9 leads to a monotonic increase in the reaction cross section from 0.252 pbarn to 4.529 pbarn.

Fig. 6. The dependence cross-section of the process $e^- e^+ \to H t \bar{t}$ of the variable T
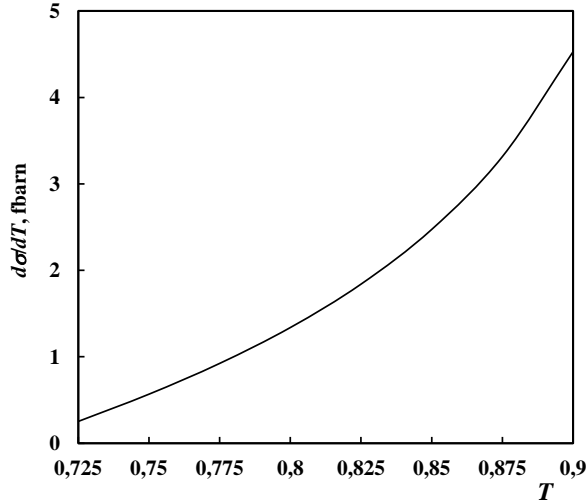
Experimental study of the reaction $e^- + e^+ \to H + f + \bar{f}$ is of particular interest, since it allows you to accurately measure the coupling constant g_{Htt}.

Conclusion

Thus, we discussed the process of the associated production of the Higgs boson and a longitudinally polarized heavy fermion pair in the collision of an arbitrarily polarized electron-positron pair $e^- + e^+ \to (\gamma^*; Z^*) \to H + f + \bar{f}$. An analytical expression for the differential cross section is obtained; the behavior of the cross section, the angular correlations of particles, the left-right spin asymmetry A_{LR}, the transverse spin asymmetry $A_\perp$, and the degree of longitudinal polarization of the fermion P_f are investigated. The calculation results are illustrated with graphs.

Appendix

Here we give the expressions for the correlation functions in the coordinate systems IIa, b and IIIa, b.

1) In systems IIa and IIb (upper (lower) sign corresponds to system IIa (IIb)):

$$\sigma_1 = \frac{2x_H^2}{(1-x_1)(1-x_2)}\,(2-s_{23}^2), \qquad\qquad \sigma_2 = \frac{x_H^2}{(1-x_1)(1-x_2)}\cdot s_{23}^2,$$

$$\sigma_3 = \frac{2x_H^2}{(1-x_1)(1-x_2)}\,(1-c_{23}^2), \qquad\qquad \sigma_4 = \mp\frac{2x_H^2}{(1-x_1)(1-x_2)}\cdot s_{23}c_{23},$$

$$\sigma_7 = 2x_H\left[\frac{x_2}{1-x_2}(c_{23}-1)-\frac{x_1}{1-x_1}(c_{23}-c_{21})\right], \quad \sigma_8 = x_H\left[\pm\frac{x_2}{1-x_2}s_{23}-\frac{x_1}{1-x_1}(\pm s_{23}\mp s_{21})\right],$$

$$\sigma_1' = -4(1+x_H)\,(2-s_{23}^2), \qquad \sigma_2' = -2(1+x_H)s_{23}^2,$$

$$\sigma_3' = -4(1+x_H)\,(1-c_{23}^2), \qquad \sigma_4' = \pm 4(1+x_H)\cdot s_{23}c_{23};$$

2) In systems IIIa and IIIb:

$$\sigma_1 = \frac{x_H^2}{(1-x_1)(1-x_2)}, \quad \sigma_2 = \sigma_3 = \sigma_4 = 0,$$

$$\sigma_7 = 2x_H\left[\frac{x_2}{1-x_2}(1-c_{32})-\frac{x_1}{1-x_1}(1-c_{31})\right], \quad \sigma_8 = x_H\left[\mp\frac{x_2}{1-x_2}s_{32}\pm\frac{x_1}{1-x_1}s_{31}\right],$$

$$\sigma_1' = -8(1+x_H), \ \ \sigma_2' = \sigma_3' = \sigma_4' = 0$$

REFERENCES

1. Djouadi A. The Anatomy of Electro-Weak Symmetry Breaking. Tome I: The Higgs boson in the Standard Model. arXiv: hep-ph/0503172v2, 2005; DOI: 10.1016/j.physrep.2007.10.004

2. Abdullaev S.K. Standard model, properties of leptons and quarks. Baku, 2017, 276p. (in Azerbaijan).

3. Emelyanov V.M. Standard Model and its extensions, Moscow, FIZMATLIT, 2007, 584p. (in Russian).

4. Langacker P. The Standard Model and Beyond. CRS Press, 2010, 635 p. DOI: http://dx.doi.org/10.1063/1.36182

5. Partignani C. et al. (Particle Data Group), Chin. Phys. C, 2016. 40. p.100001.

6. Englert F., Brout R. Broken Symmetry and the Mass of Gauge Vector Mesons // Phys. Rev. Lett., 1964, V. 13, p.321.

7. Higgs P.W. Broken Symmetries and the Masses of Gauge Bosons // Phys. Rev. Lett., 1964, V. 13, p.508.

8. Higgs P.W. Spontaneous Symmetry Breakdown without Massless Bosons // Phys. Rev., 1966, V. 145, p.1156.

9. Guralnik G.S., Hagen C.R., Kibble T.W. Global Conservation Laws and Massless Particles // Phys. Rev. Lett., 1964, V. 13, p. 585.

10. ATLAS Collaboration. Observation of a new particle in the search for the Standard Model Higgs boson with the ATLAS detector at the LHC // Phys. Letters, 2012, B716, p. 1.

11. CMS Collaboration – Observation of a new boson at a mass of 125 GeV with the CMS experiment at the LHC // Phys. Letters, 2012, B716, p. 30.

12. Rubakov V.A. Large Hadron Collider's discovery of a new particle with Higgs boson properties // Phys. Usp., 2012, 55 (10), p. 949; DOI: 10.3367/UFNe.0182.201210a.1017

13. Lanyov A.B. CMS collaboration results: Higgs boson and search for new physics // Phys. Usp., 2014, V. 57, No 9, p.923; DOI: 10.3367/UFNe.0184.201409i.0996

14. Kazakov D.I. The Higgs boson is found: what is next? // Phys. Usp., 2014, V. 57, No 9, p.930; DOI: 10.3367/UFNe.0184.201409j.1004

15. Abdullayev S. K., Gojayev M.Sh., Saddigh F.A. Decay channels of the standard Higgs boson // Moscow University Physics Bulletin. 2017, V. 72, No 4, p. 329.

16. Abdullayev S.K., Gojayev M.Sh., Nasibova N.A. Production of a Scalar Boson and a Fermion Pair in Arbitrarily Polarized e^-e^+-Beams // Russian Physics Journal, 2018, V. 61, No 1, p.94.

17. Abdullayev S.K., Gojayev M.Sh. The Higgs bosons production in arbitrary polarized electron–positron colliding beams // UZFF Moskovskoqo Universiteta, 2018. No 1. c.1810101-1.

18. Nath P. Higgs Physics and Supersymmetry // Int. J. Mod. Phys. A. 2012. V. 27. No 28. p. 1230029.

19. Barman R. K. et al. Current status of MSSM Higgs sector with LHC 13 TeV data // arXiv: 1608.02573v3 [hep-ph]. 2017.

20. Hioki Z., Konishi T., Ohkuma K. Studying possible CP-violating Higgs couplings through top-quark pair productions at muon colliders // Journal of High Energy Physics, 7, No 07; arXiv: 0706.4346v2 [hep-ph]. 2017.

21. Greco M. On the study of the Higgs properties at a muon collider // Mod. Phys. Lett. 2015. V. A30, No 39. p. 1530031.

22. Jadach S., Kycia R.A. Lineshape of the Higgs boson in future lepton colliders // Phys. Lett. 2016. B755. p.58-63 [arXiv: 1509.02406].

23. Peters K. Prospects for beyond Standard Model. Higgs boson searches at future LHC runs and other machines // arXiv: 1701.05124v2 [hep-ex]. 2017.

24. Abdullayev S.K., Agamaliyeva L.A., Qocayev M.Sh., Saddigh F.A. İssledovaniye rojdeniya higgsovskix bozonov v lepton-antileptonnıx stolknoveniyax // GESJ: Physics, 2015, V. 1, No 13, p. 36 (in Russian)

25. Abdullayev S.K., Agamaliyeva L.A., Qocayev M.Sh. İssledovaniye rojdeniya higgsovskoqo bozona v qlubokoneupruqom lepton-nuklonnom rasseyanii // GESJ: Physics, 2015, V. 2, No 14, p.28 (in Russian).

26. Abdullayev S.K., Gojayev M.Sh., Saddigh F.A. Higgs boson decay channels: $H\rightarrow\gamma\gamma$, $H\rightarrow\gamma Z$, $H\rightarrow gg$ // AJP: Fizika, 2015, XXI, No 2, p. 17.

27. Abdullayev S.K., Gojayev M.Sh., Nesibova N.E. Production of scalar boson and neutrino pair in longitudinally polarized electron-positron colliding beams // AJP: Fizika, 2017, XXII, No 3, p. 45.

28. Abdullayev S.K., Gojayev M.Sh. Production and Decay of higgs bosons in muon colliders // X International conference «Modern trends in Physics», Baku, 2017, 20-22 April.

29. LHC Higgs Cross Section Working Group Collaboration, de Florian D. et al. «Handbook of LHC Higgs Gross Sections: 4. Deciphering the nature of the Higgs Sector»// arXiv: 1610.07922v1[hep-ph]. 2016.

30. Shiltsev D.V. High energy particle colliders: past 20 years, next 20 years and beyond // Phys. Usp., 2012, V. 55, No 10, p. 965; DOI: 10.3367/UFNe.0182.201210d.1033

31. Gaemers K.J.F., Gounaris G. J. Bremsstrahlung production of Higgs bosons in e⁺e⁻-collisions // Phys. Lett., 1978, B77, No 4, 5. p.379.

32. Djouadi A., Kalinowski J., Zerwas P. Measuring the $Ht\bar{t}$ coupling in e⁺e⁻-collisions // Mod. Phys. Lett., 1992, A7, p.1765.

33. Djouadi A. The Anatomy of Electro-Weak Symmetry Breaking. Tome II: arXiv: hep-ph/0503173v2, 2003; DOI: 10.1016/j.physrep.2007.10.005

34. Abdullayev S.K., Gojayev M.Sh. The production of higgs boson and heavy fermion pair in electron-positron collisions // AJP: Fizika, 2018, XXIV, No 4, p. 11.

35. Abdullayev S.K., Gojayev M.Sh. // Moscow University Physics Bulletin, 2019, V. 74, No 1, p.24.

36. Abdullaev S.K., Mukhtarov A.I. Superstring Z'-Boson In E⁻E⁺-Annihilation // PEPAN, 1995. V. 26, No 5. p. 1264.

37. Abdullaev S.K., Mukhtarov A.I. Effects of superstring Z'-boson in the reactions $e^-e^+ \rightarrow q\bar{q}g$, $e^-e^+ \rightarrow \bar{q}\bar{q}g$ // Physics of Atomic Nuclei. 1997. V. 60, No 11. p. 1901.

38. Hamilton S.F. Measurement of the longitudinal polarization of the top quark in top-antitop events using the ATLAS detector // CERN-THESIS-2014-008, 2014, 279p.

CONFORMATIONAL PARTICULARITIES OF BOVINE LACTOFERRIN-DERIVED ACE INHIBITORY TRIPEPTIDE LRP

G.A.AGAEVA* [1], U.T.AGAEVA[1], N.M.GODJAEV[1,2]

Baku State University[1], Z.Khalilov str., 23,

Baku, AZERBAIJAN

Baku Engineering University

Baku -Sumqait Road,16 km, Azerbaijan

gulshen@mail.ru, nqocayev@beu.edu.az

ABSTRACT

By molecular mechanics method have been investigated the conformational properties of bovine lactoferrin derived ACE inhibitory tripeptide Leu-Arg-Pro (LRP). It is shown that the spatial structure of this tripeptide can be described by set of low-energy conformations. Calculations produced the values of all dihedral angles of the backbone and side chains of the optimal conformations as well as intra- and inter-residue interaction energies. Based on theoretical calculations were obtained all energy and geometry parameters and determined the molecular models of the most stable conformations of tripeptide molecule.

Keywords: ACE Inhibitory tripeptide, conformation, molecular mechanics method.

КОНФОРМАЦИОННЫЕ ОСОБЕННОСТИ АПФ ИНГИБИРУЮЩЕГО ТРИПЕПТИДА LRP, ПРОИЗВОДНОГО ИЗ МОЛЕКУЛЫ БЫЧЬЕГО ЛАКТОФЕРРИНА

РЕЗЮМЕ

Методом молекулярной механики были исследованы пространственное строение и конформационные особенности АПФ ингибирующего трипептида LRP (Leu-Arg-Pro), производного из молекулы бычьего лактоферрина. Конформационный анализ всей молекулы выявил ограниченный набор энергетически предпочтительных конформационных состояний молекулы трипептида в определенном интервале относительной энергии. В результате исследования были также определены энергетически предпочтительные области величин двугранных углов , величины энергетических вкладов межостаточных взаимодействий и водородных связей, а также взаимное расположение остатков и их боковых цепей в низкоэнергетических конформациях LRP. На основе полученных параметров были представлены пространственные структуры энергетически предпочтительных конформаций трипептида.

Ключевые слова: АПФ ингибирующий трипептид , конформация, метод молекулярной механики.

BUĞA LAKTOFERRIN MOLEKULUNDAN ALINMIŞ, AKF-NIN TRIPEPTID INHIBITORUNUN KONFORMASIYA XÜSUSIYYƏTLƏRI

XÜLASƏ

Molkulyar mexanika üsulu vasitəsilə LRP (Leu-Arg-Pro) tripeptid molekulunun fəza və konformasiya xüsusiyyətləri tədqiq olunmuşdur. LRP tripeptid molekulu angiotenzin konvertasiya fermentinin (AKF) inhibitoru kimi təsir göstərir. Molekulunun konformasiya tədqiqi ayrı-ayrı monopeptidlərin aşağı-enerjili konformasiyaları əsasında aparılmışdır. Hesablamalar nəticəsində molekulunun daxilində əmələ gələn qalıqlar arası qarşılıqlı təsirlərin enerji payları müəyyən edilmişdir. Alınan nəticələr əsasında tripeptidinin bütün enerji və həndəsi parametrləri hesablanmışdır. Molekulunun nəzəri konformasiya analizi nəticəsində enerji cəhətdən ən əlverişli konformasiyalarını stabilləşdirən qüvvəərin təbiəti və enerji payları müəyyən edilmişdir . Əldə olunan parametrlərə əsasən, tripeptidin enerji cəhətdən konformasiyalarının molekulyar modeli hazırlanmışdır.

Açar sözlər: angiotenzin konvertasiya fermentinin (AKF) inhibitoru, tripeptid, konformasiya, molekulyar mexanika üsulu.

INTRODUCTION

Angiotensin converting enzyme (ACE) is an important factor in the regulation of blood pressure. ACE inhibitors are widely prescribed for cardiovascular diseases, including high blood pressure, heart failure, and kidney failure. Angiotensin-converting enzyme (ACE) plays a critical role in blood pressure control systems (renin-angiotensin system) as it converts angiotensin I into angiotensin II, leading to the development of hypertension. Therefore, it is quite essential to study the inhibition of ACE in order to prevent and manage hypertension. ACE-inhibitory peptides, which are safer than synthetic ACE inhibitors, have been shown to be useful as antihypertensive drugs. Structural bioinformatics show that the activity of ACE-inhibitory peptides is related to both their molecular masses and amino acid sequences. Some studies showed that short-chain polypeptides with low molecular masses exhibited high ACE-inhibitory activity. The majority of ACE inhibitory di- and tripeptides have Pro in the C-terminal position and a branched chain amino acid, I, L, or V, in the N-terminal position. In the work [1] have been investigated the ACE inhibitory peptides from bovine lactoferrin and to explore their potential antioxidative and anti-inflammatory activities. So, 8 peptides were identified and tripeptide Leu-Arg-Pro, LRP (IC$_{50}$ = 1.2 ± 0.05 µM) showed the highest ACE inhibitory activity. LRP (50 µM) significantly inhibited tumor necrosis factor-alpha (TNF-α)-stimulated inflammation in endothelial cells. LRP (20 and 50 µM) also significantly reduced superoxide level in basal oxidation test. The results indicated that ACE inhibitory tripeptide LRP also showed antioxidative and anti-inflammatory activities, suggesting its potential application against hypertension. For understanding of the mechanism of action of pharmacologically active peptide is necessary knowledge their preferred conformational particuliarities. The major aim of the present article is the investigation of the preferred conformations of LRP tripeptide with the purpose of getting insight into basic structural requirement that determine ligand-receptor interaction. The comparative conformational analysis of this tripeptide have been carried out by molecular mechanic method, which allow to determine a whole sets of energetically preferred conformers of peptide molecule.

METHOD

This investigation were carried out using molecular mechanics method as described in Refs.[2,3]. Computations were carried out on the computer using universal programs complex [4]. This program calculates the conformational energy of a peptide as a sum of nonbonded, hydrogen-bonded and electrostatic energies for pairwise atomic interactions and torsional potential energies for rotation about bonds. Bond lengths and bond angles are fixed at standard values, and only dihedral angles are allowed to vary. For a stable conformation, the φ, ψ, ω, χ dihedral angles of backbone chain are located in a low energy regions: R (φ, ψ = - 180°-0°) ,B (φ =- 180°-0°, ψ = 0°-180°), L (φ, ψ =0°-180°) and P (φ =0°-180°, ψ =-180°-0°). The conformational state of each amino acid residue is conveniently described by backbone φ, ψ, ω and side chain χ_n dihedral angles. All backbone forms of a dipeptide can be classified into two types, referred to as shapes: folded (*f*) and extend (*e*) . For a tripeptide, all possible backbone forms may be specified by four shapes, i.e. ff, fe, ef and ee. The number of forms in each shape depends on possible combinations of R,B,L and P forms are possible for glycine, R,B, and L forms occur with alanine-type residues, but only R and B for proline. The dihedral angle values corresponding to the lowest energy states of monopeptides were used as starting conformations. The conventions used for torsion angles are those of IUPAC-IUB Commission [5].

RESULTS AND DISCUSSION

Three-dimensional structure of the Leu-Arg-Pro have been investigated basing on the low-energy conformations of constitutive monopeptides. The starting conformations of the Leu-Arg-Pro tripeptide were obtained by combining the low-energy structures of all of residues. The residues of the tripeptide have different side chain possibilities. It should be noted that the N-terminal residue of this tripeptide has large hydrophobe side chain and thefore its side chain is relatively flexible, but second residue Arg has large positive charged side chain. The Pro residue is known to significantly limit the conformational possibilities of a peptide molecule. Unlike other residues, Pro cannot realize conformations with the *L*-form of the backbone due to the rigidly fixed bond. Moreover, only the *B* form of the backbone is conformationally stable for the residue that precedes Pro [6]. For the second residue, the values of dihedral angles of the peptide backbone were taken in the *B*-area. As a consequence, only two (*ee* and *ef*) of the four shapes possible for a tripeptide are allowed for these sequences. In practice, only the positions of side chains of the amino acid residues adjacent to Pro were varied, because Pro has no flexible side chain. The starting structural approximations for the *N*-terminal tripeptides were chosen with regard to the limitations associated with the Pro residue. For Pro, the angles were taken from the *B* and *R* areas, and the *B*-, *R*-, and *L*-areas, for the first residue. The values of dihedral angles of the side chains were taken to be 60, 180, and -60^0 for Leu and Arg residues. The angles of side chain of Arg χ_3 and χ_4, were taken to be equal to 180^0. These starting variants exhibit 396 conformers for a tripeptide Leu-Arg-Pro belonging to only 2 shapes. The energy minimization of the obtained set of the structural variations for this tripeptide, revealed a remarkable energy differentiation among the optimal conformations. After energy minimization had been performed a rather limited number of conformations lay in the 0-4 kcal/mole ΔE energy interval. Tables 1 demonstrate the values of the relative energy of optimal conformations of the optimal conformers obtained after energy minimization for tripeptide Leu-Arg-Pro. Table 2 show the values of the energy contributions of different forces in the most stable conformers obtained after energy minimization for tripeptide. The spatial structures of the lowest energy conformations of this tripeptide are shown in Fig.1. The effective interactions of the opposite charged atom groups of the residues and terminal groups was possible in these conformations. This contact has the electrostatic nature. The interaction of side chains is less effective in the other forms of this tripeptide. Calculations showed that in global conformation of the the Leu-Arg-Pro side chain of Leu is formed the effective interactions with Arg side chain and C-terminal end group. The energy contributions of these interactions are presented in Table 3. This investigation demonstrated a definite conformational possibilities of this tripeptide. The values of energy contributions of intra- and inter-residues interactions of backbone and side chains of lowest energy conformations of tripeptide Leu-Arg-Pro are given in Tables 4. The values of dihedral angles of the three more stable conformations of this tripeptide are given in Table 4.

Table 1. The optimal conformations of tripeptide Leu-Arg-Pro in relative energy interval 0-4 kcal/mole)

№	Shape	Backbone form	The relative energy interval (kcal/mole)				
			0÷1	1÷2	2÷3	3÷4	>4
1	ee	BBB	1	3	2	6	150
		LBB	-	-	-	2	70
2	fe	RBB	-	-	-	2	160

Table 2. Energy contributions of preferred conformations of all possible structured types of the tripeptides Leu-Arg-Pro

№	Conformation	Energy contributions (kcal/mol)				E_{rel}
		E_{nb}	E_{el}	$E_{tor.}$	$E_{abs.}$	
1.	$B_{21}B_{23}B$	-10.7	-3.5	3.7	-10.6	0
2.	$B_{21}B_{22}B$	-8.8	-0.2	1.4	-7.6	3.0
3.	$B_{21}B_{21}B$	-8.4	0.1	1.5	-6.8	3.8
4.	$R_{21}B_{12}B$	-9.6	0.1	1.7	-7.8	2.8
5.	$R_{21}B_{12}B$	-10.5	1.6	1.6	-7.3	3.3
6.	$R_{21}B_{12}B$	-8.6	0.1	2.5	-6.1	4.5
7.	$L_{21}B_{23}B$	-9.1	0.2	1.5	-7.5	3.1
8.	$L_{22}B_{23}B$	-8.2	-2.6	3.7	-7.1	3.5
9.	$L_{21}B_{21}B$	-8.9	0.4	1.6	-6.9	3.7

Table 3. The energy contributions of the intra- and inter-residues interactions of the stable conformations of Leu-Arg-Pro tripeptide

№ conformation	Leu	Arg	Pro	
I-$B_{21}B_{23}B$	0.4	0.7	-4.5	
II- $B_{21}B_{22}B$	-0.3	0.8	-4.4	
III- $B_{21}B_{21}B$	0.1	0.8	-4.5	
IV- $R_{21}B_{12}B$	0.3	-0.9	-3.0	
V- $R_{21}B_{33}B$	0.3	-2.8	-3.5	Leu
VI- $R_{22}B_{12}B$	1.2	-0.8	-3.1	
VII- $L_{21}B_{23}B$	-0.1	1.0	-4.8	
VIII- $L_{22}B_{23}B$	1.1	0.6	-4.3	
IX- $L_{21}B_{21}B$	-0.2	0.9	-4.6	
I		2.1	-13.7	
II		0.2	-6.3	
III		1.5	-7.1	
IV		-0.3	-6.6	
V		0.3	-4.1	Arg
VI		-0.3	-6.7	
VII		0.7	-6.8	
VIII		1.9	-11.3	
IX		1.6	-7.1	
I			1.1	
II			0.9	
III			1.0	
IV			1.0	
V			0.9	Pro
VI			1.1	
VII			1.0	
VIII			1.1	
IX			0.9	

Table 4. The values of dihedral angles of the three more stable conformations of tripeptide Leu-Arg-Pro

Residue	Conformation	Backbone angles			Side chain angles			
		φ	ψ	ω	χ1	χ2	χ3	χ4
Leu	$B_{21}B_{23}B$	-70	141	178	178	70	180	178
	$R_{21}B_{12}B$	-62	-74	181	172	65	179	177
	$L_{21}B_{23}B$	57	101	179	173	58	179	176
Arg	$B_{21}B_{23}B$	-120	92	167	190	-74	194	179
	$R_{21}B_{12}B$	-143	52	173	60	183	181	179
	$L_{21}B_{23}B$	-132	82	178	187	-170	179	181
Pro	$B_{21}B_{23}B$	-60	105	-	-	-	-	-
	$R_{21}B_{12}B$	-60	128	-	-	-	-	-
	$L_{21}B_{23}B$	-60	128	-	-	-	-	-

Figure1. The spatial structure of three different low-energy conformations
of tripeptide Leu-Arg-Pro; a) $B_{21}B_{23}B$; b) $R_{21}B_{12}B$; c) $L_{21}B_{23}B$

a)

b)

c)
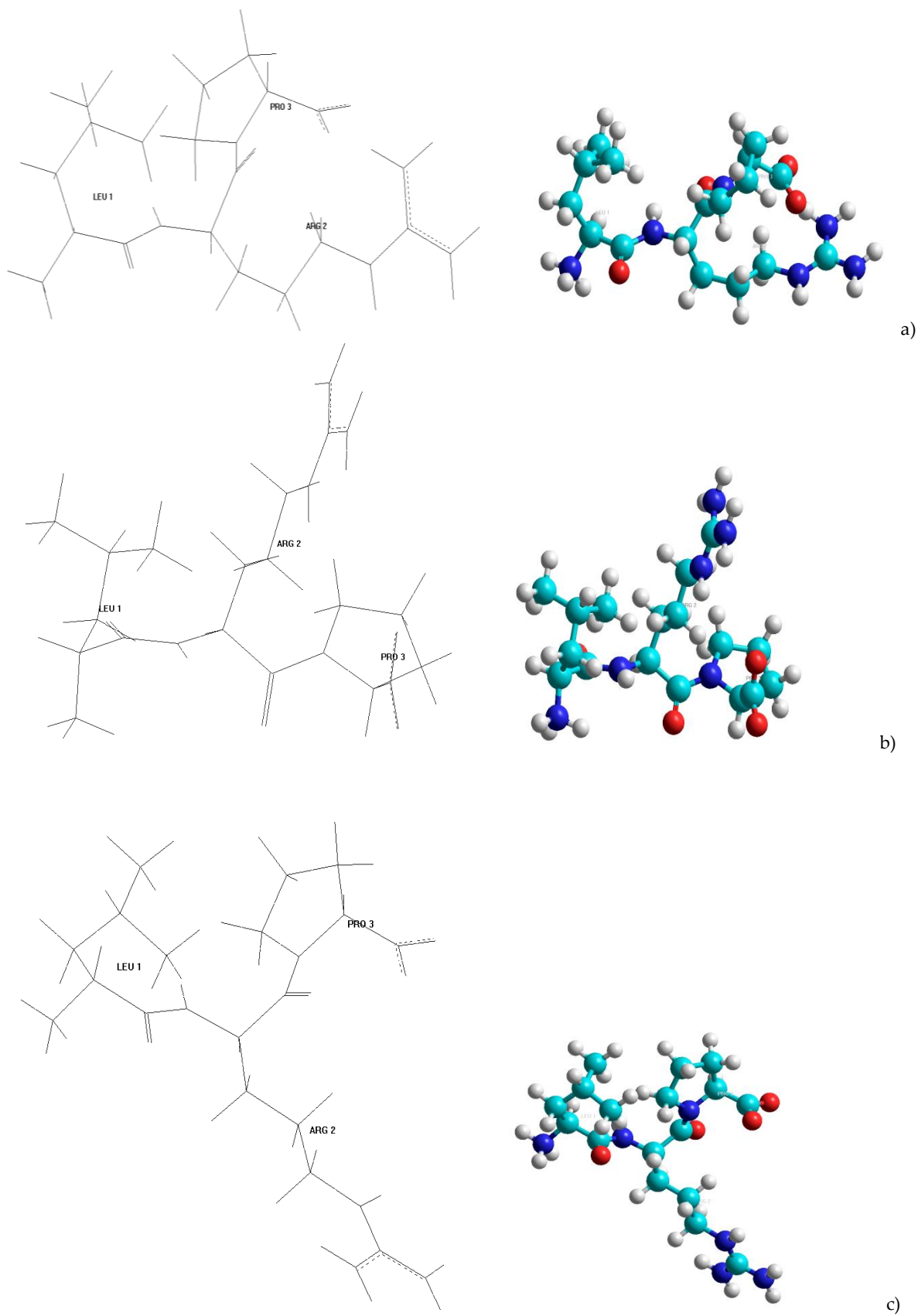
CONCLUSION

Our calculations of the spatial structures of biologically active tripeptide Leu-Arg-Pro demonstrated this molecule has a limited set of the stable structures that are characterized by the extended backbone form. The conformational analysis helped reveal a number of special features of spatial arrangement of these drug-based tripeptide, which may be useful as a base for a directed search and synthesis of their more effective structural analogs.

REFERENCES

1. Gu Y., Wu **J.,** Bovine lactoferrin-derived ACE inhibitory tripeptide LRP also shows antioxidative and anti-inflammatory activities in endothelial cells**.** Journal of Functional Foods, 2016, vol. 25, p. 375-384.

2. Popov E.M., Quantative approach to conformations, Int. J. Quantum Chem. 1979 ,vol.16, p.707-737.

3. Agaeva G.A., ,Agaeva U.T., N.M Godjaev N.M. The spatial organization of human hemokinin-1 and mouse/ rat hemokinin-1 molecules, Biophysics (Russian),2015, vol.60, p.365-377.

4. Maksumov I.S., Ismailova L.I., Godjaev N.M. The program for semiempirical calculation of conformations of the molecular complexes J.Struct.Khim.(Russian), 1983,vol.24,p.147-148.

5. IUPAC-IUB Quantity. Units and Symbols in Physical Chemistry, 1988, vol. 39, Blackwell Scientific Publications, Oxford.

6. Schimmel, P.R. and Flory, P.J. Conformational energies and conformational statistics of copolypepides containing L-proline., J. Mol. Biol., 1968,vol. 34, p. 105–110.

RADIATION OF NOTE SEMICONDUCTORS IN EXTERNAL ELECTRIC FIELD

E.R. HASANOV[1,2], R.K.MUSTAFAYEVA[3]

[1]BSU, Institute of Physics Problems Az- 1143, Baku, Z.Khalilov street, 23,

[2]Institute of Physics, Azerbaijan National Academy of Sciences, Baku, Azerbaijan, Az- 1143, H.Javid ave.,

[3]Baku State University, Baku, Az-1145, Z.Halilov str., 23

Ruhi-qrk@mail.ru

ABSTRACT

Fluctuations of a current in spending environments arise at availability external influences. It can take place, if the spending environment is in an external electric floor, in external electric and magnetic fields and even at availability of a gradient of temperature in the environment. In semiconductors (electronic type, electronically-hole type) carriers of a charge from external influences are accelerated or slowed down impurity by the centers and consequently distribution of a charge in the semiconductor deviates equilibrium values and thus inside of the semiconductor there are areas with different values of an electric field. These sites (them name domains) move on all image and then there are fluctuations of a current in-external a circuit [2].

Key words: semiconductors, electric, field, electric field, radiation.

ИЗЛУЧЕНИЯ ПРИМЕСНЫХ ПОЛУПРОВОДНИКОВ ВО ВНЕШНЕМ ЭЛЕКТРИЧЕСКОМ ПОЛЕ

РЕЗЮМЕ

Показано, что в примесных полупроводниках с двумя типами носителей заряда во-внешнем электрическом поле возникает колебания с определенной частотой. Доказано, что контакты полупроводника сильно влияет на колебания тока в цепи. Инжекция носителей через контакты изменяет знак импеданса образца. Показано, что в образце в зависимости от знаков носителей заряда просходить колебания тока в восьми предельных случаях. В этих предельных случаях получены аналитические формулы для электрического поля и для частоты колебания тока в цепи. Получены значения электрического поля для частотыколебания тока, когда частота колебания больше всех характерных частот, а также когда частота колебания тока, больше чем все характерные частоты. Доказано, что в цепи возможно возникновения емосильного и индуктивного характера сопротивления.

Ключевые слова: полупроводники, электричество, поле, электрическое поле, излучение.

AŞQARLI YARIMKECIRILƏRIN XARICI ELEKTRIK SAHƏSINDƏ ŞÜALANMASI

XÜLASƏ

İsbat olunmuşdur ki, iki tip keçiriciliyə malik aşqarlı yarımkeçiricilərdə xarici elektrik sahəsində müəyyən tezlikli rəqslər yaranır. Göstərilmişdir ki, yarımkeçiricinin kontaktları dövrəcə cərəyan rəqslərinə ciddi təsir edir. Kontaktlarda olan yükdaşıyıcıların injeksiyası nümunənin impedansının işarəsini dəyişdirir. İsbat olunmuşdur ki, nümunənin daxilində yükdaşıyıcıların işarəsindən asılı olaraq səkkiz halda rəqs yarana bilər. Bu halların hamısında elektrik sahəsi və tezlik üçün analitik düsturlar alınmışdır. Rəqsin tezliyinin xarakterik tezliklərdən böyük və kiçik qiymətlərində elektrik sahəsi və rəqs tezliyinin ifadələri alınmışdır. İsbat olunmuşdur ki, dövrədə induktiv və tutum müqavimətləri yaranır.

Açar sözlər: yarımkeçiricilər, elektrik, sahə, elektrik sahəsi, şüalanma.

In impurity semiconductors recombination and generation of carriers of a current impurity the centers lead to fluctuation of a current in the sample. Availability impurity the centers and their charging conditions causes occurrence of fluctuation of a current in impurity semiconduc-

tors. Some impurity in semiconductors create the centers, capable to be in the several charged conditions (unitary, twice, it is triple positively or negatively charged). For example, atoms of gold in Germany to the order a neutral condition, can be unitary positive also charged or unitary, twice and is triple the negative charged centers; atoms of copper in Germany to the order a neutral condition, can be also unitary, twice and is triple the negative charged centers; atoms of copper in Germany to the order a neutral condition, can be also unitary, twice and is triple the negative charged centers. These impurity have different power levels in the forbidden zone. In dependence of removal of these levels on a valent zone (or from a bottom of a zone of conductivity) them name deep levels. These deep traps are capable to grasp electrons and holes depending on their charging conditions. Variations of concentration of electrons in a zone of conductivity and holes in a valent zone lead to variation of the general electrical conductivity the semiconductor. Depending on an experimental situation these deep traps possess a different degree of activity. In electric floor E electrons (as well as holes) receive energy eEl (where, e – a positive elementary charge, l-length of free run of electron). Therefore electrons can overcome Coulombic a barrier of unitary charged center and to be grasped, i.e. recombine it. Also generating electrons in deep traps of a zone of conductivity is possible. Besides electrons mightily to be generated from deep traps in a zone of conductivity. At capture of electrons by deep traps in a valent zone, the quantity of holes increases. At capture of electrons from deep traps holes, the quantity of holes decreases.

In the presented theoretical work we shall construct the theory of external instability in semiconductors with two types of carriers of a charge (electrons and holes) and the certain deep traps at availability of a constant external electric field.

The theory of fluctuations in view of a relaxation of carriers of a charge is constructed in work.

In the further we shall have to a type, that the semiconductor possesses carriers of both signs (electrons and holes), with concentration accordingly equal and. Concentration of negatively charged traps we shall designate. Let concentration of unitary negatively charged traps equally, and twice negatively charged traps -. Total of negatively charged traps we shall designate it is defined as the sum and:

$$N_0 = N + N_- \tag{1}$$

In the model of the semiconductor chosen by us at availability of external constant electric field E0, inside of the sample there is eltrastic a field

$$\vec{E} = \vec{E}_0 + \vec{E}' . \tag{2}$$

Thus concentration of carriers of a charge are defined under formulas

$$n_- = n_0 + n' \, ; n_+ = n_+^0 + n_+' . \tag{3}$$

In the semiconductor described in the above-stated parameters occurs fluctuations of carriers of a charge and an electric current. If thus in an external circuit the full current is equal

$$I = I_+ + I_- = const , \tag{4}$$

That fluctuations inside of the sample can grow (because of availability of internal instability).

With occurrence in an external circuit of a part of a current

$$I' \neq 0, \tag{5}$$

There is an external instability. Available instability frequency and a wave vector of fluctuation have a following appearance:

$$k = \frac{2\pi}{L} \cdot m. \; (m = 0, \pm 1, \pm 2, \ldots), \tag{6}$$

$$\omega = \omega_0 + i \cdot \omega_1. \tag{7}$$

Where, L-the size of the sample, - and - material and imaginary parts of frequency of fluctuation inside of the sample accordingly.

At external instability of a condition (6) and (7) look like:

$$\omega = \omega_0, \; k = k_0 + i \cdot k_1. \tag{8}$$

In the given work to us analyzed conditions of external instability (i.e. conditions of fluctuation of a current in an external circuit) in the above-stated semiconductor in a constant external electric floor.

At the theoretical analysis of external instability it is necessary to calculate an impedance of the sample. Voltampernaya the characteristic of the sample in conditions of external instability has a falling site and consequently the actual part of an impedance is negative. From the equation

$$\operatorname{Re} Z + R = 0 \tag{9}$$

Frequency of fluctuation of a current or value of an electric field in conditions of external instability is defined. In the equation (9) R - ohmic resistance in a circuit. The imaginary part of an impedance in a falling site can have a positive or negative sign. Then from the equation

$$\operatorname{Im} Z + R_1 = 0 \tag{10}$$

It is defined either frequency, or an electric field. In the given equation R_1 - resistance of capacitor or inductive character.

The basic equations of a problem

The equation of indissolubility for electrons in the semiconductor with the above-stated types of traps looks like [1]:

$$\frac{\partial n}{\partial t} + divj_- = \gamma_-(0)n_{1\_}N_- - \gamma_-(E)n_-N = \left(\frac{\partial n_-}{\partial t}\right)_{rek} \tag{11}$$

Here, - density of a stream of electrons:

$$j_- = -n_- \cdot \mu_-(E) - D_- \cdot \nabla n_-, \tag{12}$$

- Factor of emission of electrons twice negatively charged traps in absence of an electric field (it can be named factor of thermal generation). In non-degenerate the semiconductor the given factor from an electric field does not depend $\gamma_-(E)$- factor of capture of electrons unitary negatively charged traps at availability of an electric field. Concentration - is defined from condition $\left(\frac{\partial n_-}{\partial t}\right)_{rek} = 0$ [3]

$$n_{1-} = \frac{n^0 N_0}{N_-^0} \tag{13}$$

- The mobility of electrons depending on an electric field, factor of diffusion of electrons.

The equation of indissolubility for holes will look like [2, 3, 4, 5]:

$$\frac{\partial n_+}{\partial t} + div j_+ = \gamma_+(E) n_{1+} N - \gamma_+(0) n_+ N = \left(\frac{\partial n_+}{\partial t} \right)_{rek} \tag{14}$$

$$j_+ = n_+ \cdot \mu_+(E) \cdot \vec{E} - D_+ \nabla n_+ \tag{15}$$

$$n_{1+} = \frac{n_+^0 \cdot N_-^0}{N_0} \tag{16}$$

Owing to recombination and generation, the number of twice and unitary negatively charged traps changes (the total number of traps remains constant). The equation defining variation of traps in due course looks like [2, 3]:

$$\frac{\partial N_-}{\partial t} = \left(\frac{\partial n_+}{\partial t} \right)_{rek} + \left(\frac{\partial n_-}{\partial t} \right)_{rek}. \tag{17}$$

To these equations it is necessary to add a condition quasineutrality

$$div j = e \cdot div(j_+ - j_-) \tag{18}$$

According to the expression (18), the full current does not depend on coordinates, but depends on time.

THE THEORY

The equations (11), (14), (17), (18) should be solved in common. At linear approximation and from formulas (11), (14), (17), (18) we shall easily receive

$$\Delta n_{\pm} = \Delta n_{\pm}' \cdot e^{-i\omega t} + \Delta n_{\pm}'' \cdot e^{i(kx-\omega t)}, \quad E' = \Delta E' + \Delta E'' \tag{19}$$

$$\begin{cases} \Omega_1 \Delta n'' + \Omega_2 \Delta E'' + \Omega_3 \Delta N_-'' = 0 \\ \theta_1 \Delta n_+'' + \theta_2 \cdot \Delta E'' + \theta_3 \Delta N_-'' = 0 \\ \Delta N_-'' = A \Delta n_-'' + B \Delta n_+'' + C \Delta E'' \\ \Delta E'' = A_1 \Delta n_-'' + B_1 \Delta n_+'' \end{cases} \tag{20}$$

$$\begin{cases} \Omega_1' \Delta n' + \Omega_2' \Delta E' + \Omega_3' \Delta N_-' = 0 \\ \theta_1' \Delta n_+' + \theta_2' \cdot \Delta n_-' + \theta_3' \Delta E' = 0 \\ \Delta N_-'' = A \Delta n_-'' + B \Delta n_+'' + C' \Delta E' \end{cases} \tag{21}$$

The coefficients Ω, θ, A, B, C depend on the equilibrium values of physical quantities.

At reception of formulas (19) and (20) following designations have been entered:

$\nu_- = \gamma_-(E_0) \cdot N_0$ - Frequency of capture of electrons unitary charged traps,

$v_+^E = \gamma_+(E_0) \cdot N_0$ - Frequency of emission of holes unitary charged traps,

$v_+ = \gamma_+(0) \cdot N_-^0$ - Frequency of capture of holes twice charged traps,

$v'_+ = \gamma_+(0) \cdot n_+^0 + \gamma_+(E_0) \cdot n_{1+}$ - The combined frequency of capture and emission of holes by nonequilibrium traps

$v'_- = \gamma_-(0) \cdot n_{1-} + \gamma_-(E_0) \cdot n_-^0$ - The combined frequency of capture and emission of electrons by nonequilibrium traps

$$v = v'_+ + v'_-; \quad \beta_\pm = 2 \cdot \frac{d \ln \gamma_+(E_0)}{d \ln(E_0^2)}.$$

Except for these designations are used $D_\pm = \dfrac{T}{e} \cdot \mu_\pm$ - Einstein's parity.

$$n_\pm^0 \ll N_0, N_-^0; \quad \upsilon_\pm^0 = \mu_\pm^0 \cdot E_0 = \upsilon_\pm; \quad n_\pm^0 = n_\pm$$

Excepting $\Delta N'_-, \Delta N''_-, \Delta E', \Delta E''$ from the equations (20) and (21), we shall receive following systems of the equations for definition and a wave vector to:

$$\begin{cases} f_- \Delta n''_- + f_+(k) \cdot \Delta n''_+ = 0 \\ F_-(k) \Delta n''_- + F_+ \Delta n''_+ = 0 \end{cases} \tag{22}$$

$$\begin{cases} f_-(0) \cdot \Delta n'_- + f_+(0) \cdot \Delta n'_+ + f\Delta I = 0 \\ F_-(0) \cdot \Delta n'_- + F_+(0) \cdot + F\Delta I = 0 \end{cases} \tag{23}$$

Values f_-, f_+, F_-, F_+ are easily obtained from (20), (21)

Expressions $U_\pm(k)$, $U_\pm(0)$, $\Phi_\pm(k)$, $\Phi_\pm(0)$ easily turn out from formulas (20) and (21). Therefore their expressions it is not written out. Solving (23) it is defined in a following type:

$$\Delta n'_- = \frac{F_-(0) \cdot f - f_+(0) \cdot F}{f_-(0) \cdot F_+(0) - f_+(0) \cdot F_-(0)} = c_- \cdot \Delta j,$$

$$\Delta n'_+ = \frac{f_-(0) \cdot F - F_-(0) \cdot f}{f_-(0) \cdot F_+(0) - f_+(0) \cdot F_-(0)} = c_+ \Delta j \tag{24}$$

For definition of a wave vector (22) we should solve the dispersive equation received from a determinant, made of factors $U_\pm(k)$, $\Phi_\pm(k)$:

$$f_-(k) \cdot F_+(k) - f_+(k) \cdot F_-(k) = 0 \tag{25}$$

1) High-frequency case i.e. $\sigma = \sigma_+ + \sigma_-$

$$\frac{v'_\pm}{v_\pm} \ll 1, \quad \frac{T v_\pm}{e E_0 \upsilon_\pm} \ll 1, \quad \frac{T}{e E_0 l} \ll 1,$$

At the decision of the dispersive equation (25) we used small parameters, Where l – length of a crystal.

2) a low-frequency case, i.e.

$$k_1 = k_{10} + ik'_1$$
$$k_2 = k_{20} + ik'_{21} \tag{26}$$

After a finding of expression of wave vectors к1 and к2 by means of the formula (26) it is possible to calculate an impedance of a crystal, representing expression catch

Let's receive for an impedance expression

For definition of constants we should use boundary conditions of deviations from equilibrium conditions. In dependence by-pass directions of both contacts it is possible to distinguish two types of boundary conditions:

1) On both contacts particles of an identical sign are injected

$$\Delta E(x,t) = \frac{1}{\sigma}\left(\Delta J - e\upsilon_-\Delta n_- + e\upsilon_+\Delta n_+ + \frac{T}{e}\mu_+\nabla n_+ - \frac{T}{e}\mu_-\nabla n_-\right) \tag{27}$$

where, $\Delta n_+ = c_1^+ e^{ik_1 x} + c_2^+ e^{ik_2 x} + c^+ \Delta J$ u $\Delta n_+ = c_1^- e^{ik_1 x} + c_2^- e^{ik_2 x} + c^- \Delta J$

2) On both contacts particles of an opposite sign are injected

$$Z = \frac{1}{\Delta J \cdot S'}\int_0^L \Delta E(x,t)dx = Z_0\left[1 - \frac{e(e^{ik_1 L}-1)}{\sigma}\cdot\left(\frac{\upsilon_- C_1^- + \upsilon_+ C_1^+}{\Delta J i k_1 L}\right) + \frac{T}{e}\cdot\frac{\mu_- C_1^- + \mu_+ C_1^+}{\Delta J L} - \right. $$
$$\left. - \frac{e}{\sigma}(\upsilon_- C^- + \upsilon_+ C^+)\right] \tag{28}$$

Considering all four cases we should define constants and therefore an impedance crystal under the formula (28). In the meantime the way of definition of constants is identical in all four cases. Therefore boundary conditions we shall write in such type

$$\Delta n_+(0) = \delta_+(0)\Delta J', \Delta n_+(L) = \delta_+(L)\Delta J', \Delta n_-(0) = \delta_-(0)\Delta J', \Delta n_-(L) = \delta_-(L)\Delta J' \tag{29}$$

Substituting (29) in (27) we shall receive

$$C_1^+ = \frac{[\delta_+(0) - C^+](e^{\alpha_2} - e^{\alpha^1}) - [\delta_+(L) - \delta_+(0)]}{(e^{\alpha_2} - e^{\alpha^1})}\cdot\Delta J';$$
$$C_2^+ = \frac{[\delta_+(L) - \delta_+(0)]}{(e^{\alpha_2} - e^{\alpha^1})}\cdot\Delta J'.$$

$$C_1^- = \frac{[\delta_+(0) - C^-](e^{\alpha_2} - e^{\alpha^1}) - [\delta_-(L) - \delta_-(0)]}{(e^{\alpha_2} - e^{\alpha^1})}\cdot\Delta J';$$
$$C_2^- = \frac{[\delta_-(L) - \delta_-(0)]}{(e^{\alpha_2} - e^{\alpha^1})}\cdot\Delta J'. \tag{30}$$

Substituting (30) in (28) we shall receive expressions of an impedance as function of an electric field and frequency of fluctuation of a current. However the received expressions of an impedance are bulky enough. Therefore they will be analyzed in following limiting cases.

High-frequency case:

$$\omega \gg \nu_+^E, \nu_\pm, \nu_\pm'$$

1) $n \gg n_+$, given δ_+^0 $L\upsilon_-\beta_- \ll \upsilon_+$

$$\frac{\mathrm{Re}\,Z}{Z_0} = 1 - \left(\frac{2\nu_-\beta_-}{\omega}\right)^2 - \frac{E_0}{E_1} - \frac{E_0^2}{E^2(\delta_+(0))}\cdot\left(\frac{3\nu_-\beta_-}{\omega}\cdot\sin\theta + \cos\theta\right); \theta = \frac{\omega L}{\upsilon_+}$$

$$\frac{\text{Im}\, Z}{Z_0} = \left(\frac{2v_- \beta_-}{\omega}\right)^2 - \frac{6v_-}{\omega} \cdot \frac{E_0}{E_1} - \frac{E_0^2}{E^2(\delta_+(0))} \cdot \left(\sin\theta - \frac{3v_-}{\omega}\cos\theta\right).$$

(31)

Where $Z_0 = \dfrac{L}{\sigma_0 S}$; S-cross-section section of the sample.

$$\frac{1}{E_1} = \frac{8v_+^E v_-^2 \beta_+ \beta_-^2 \mu_+}{L\omega^4}; \quad \frac{1}{E^2(\delta_+(0))} = \frac{4v_- \mu_- e\mu_+ \delta_+(0)\beta_-}{L\omega^2}$$

Solving system of the equations

$$\begin{cases} \dfrac{\text{Re}\, Z}{Z_0} + \dfrac{R}{Z_0} = 0 \\ \dfrac{\text{Im}\, Z}{Z_0} + \dfrac{R_1}{Z_0} = 0 \end{cases}$$

(32)

Where, R-ohmic, R1-capacitor or inductive resistance at

$$R = R_1 = Z_0.$$

Let's easily receive

$$E_0 = \frac{2E_1}{1 + \dfrac{6v_-}{\omega}}; \quad \omega = 3v_-(\beta_-)^{\frac{1}{2}}$$

2) $n \gg n_+$, given $\delta_-^0(0)$

$$\frac{\text{Re}\, Z}{Z_0} = 1 - \left(\frac{2v_- \beta_-}{\omega}\right)^2 - \frac{E_0^2}{E^2(\delta_+(0))} \cdot \left(2 + \frac{\omega}{v_-} \cdot \sin\theta + \cos\theta\right) + 1 = 0$$

$$\frac{\text{Im}\, Z}{Z_0} = \frac{E_0^2}{E_1^2(\delta_-(0))}\left(\frac{v_- \beta_-}{\omega}\sin\theta + \cos\theta\right) - \left(\frac{2v_- \beta_-}{\omega}\right)^2 + 1$$

(33)

From (33) we shall easily receive

$$E_0 = \frac{E_1[\delta_-(0)]}{\sqrt{2}}; \qquad \omega = v_- \beta_- ; \qquad E[\delta_-(0)] = \left(\frac{L\beta_- v_-}{e\mu_- \mu_+ \delta_-}\right)^{\frac{1}{2}}$$

3) $n \ll n_+$, given $\delta_-^0(0)$

$$\frac{\text{Re}\, Z}{Z_0} = 1 + \frac{E_0}{E_1}\left(\frac{\mu_+ v_-}{\mu_- \omega}\sin\theta + \cos\theta\right) - \frac{E_0^2}{E^2(\delta_-^L)}\left(\frac{\mu_+ \omega}{\mu_- v_-}\sin\theta + \cos\theta + \frac{4n_- \mu_- \beta_-}{n_+ \mu_+}\cos\theta\right) + 1 = 0 \quad (34)$$

$$\frac{\text{Im}\, Z}{Z_0} = \frac{E_0}{E_1}\left(\sin\theta - \frac{v_-}{\omega}\cos\theta\right) - \frac{E_0^2}{E^2(\delta_-^L)}\left(\sin\theta - \frac{4\omega\mu_-}{v_- \mu_+} + 1\right)\cos\theta = 0$$

$$\frac{1}{E_1} = \frac{n_- \mu_-^2 \beta_-}{n_+ \mu_+ L\omega^2} ; \qquad \frac{1}{E^2(\delta_-^{L:})} = \frac{v_- e\mu_- \mu_+ \delta_-^L}{L\omega^2}$$

From (34) at. T.e $\omega L / \vartheta_-$-we shall receive

$$E_0 = 2E_1, \qquad \omega = 2\sqrt{2} - \frac{v_- E\delta}{E_1}, \qquad \frac{2\sqrt{2} - v_- E\delta}{E_1} \gg 1$$

(35)

4) $n_- \ll n_+$, given δ_+^L

$$\frac{\operatorname{Re} Z}{Z_0} = 2 + \frac{E_0}{E_1}\left(-\frac{\mu_-}{\mu_+}\sin\theta + \frac{\mu_-\omega}{\mu_+ v_-}\cos\theta\right) + \frac{E_0^2}{(E_\delta^2)}\left(\frac{\mu_+\omega}{\mu_- v_-}\sin\theta + \cos\theta\right) = 0$$

$$\frac{\operatorname{Im} Z}{Z_0} = \frac{v_- E_0}{\omega E_1}\left(\sin\theta + \frac{\omega}{v_-}\cos\theta\right) + \frac{E_0^2\omega}{E_{\delta+}^2(v_+^E)}\left(\sin\theta + \frac{\mu_-\omega}{\mu_+ v_-}\cos\theta\right) + 1 = 0$$

(36)

Substituting value E_δ in (36) we shall receive

$$\frac{\omega}{v_-} = \sqrt{2}\pi\left(\frac{\mu_-}{\mu_+}\frac{1}{e\vartheta_-\delta_+^L}\right)^{\frac{1}{2}}\left(\frac{\vartheta}{v_- L}\right)^{\frac{1}{2}} \gg 1 \text{ and it proves that } \omega \gg v_-.$$

Low-frequency case $\omega \ll v_+^E$; $Lv_-\beta_- \ll \vartheta_-$

1) $n_- \gg n_+$, given δ_+^0,

$$\frac{\operatorname{Re} Z}{Z_0} = 2 - \frac{E_0}{E_1}\left(\frac{\mu_-}{\mu_+}\sin\theta + \ln\theta\right) - \frac{E_0^2}{(E_\delta^2)}\left(\frac{\omega}{v_+}\sin\theta + \ln\theta\right) = 0$$

$$\frac{\operatorname{Im} Z}{Z_0} = -\frac{E_0}{E_1}\left(\frac{4\omega}{v_+}\cos\theta - \sin\theta + \frac{\omega}{v_+}\right) + \frac{E_0^2\omega}{E_{\delta+}^2(v_+^E)}\frac{n_-}{n_+}\left(2\sin\theta - \frac{\omega}{v_+}\cos\theta\right) + 1 = 0$$

(37)

$$\frac{1}{E_1} = \frac{n_- v_+^2 \mu_+ e\beta_+}{Lv_+^2 n_1} \quad ; \qquad \frac{1}{E^2(\delta_+^L)} = \frac{\mu_+^2\beta_+ e\delta_+^0}{Lv_+\mu_-}$$

From (34) at $\theta = \dfrac{\pi}{2}$.

$$E_0 = E_1 \qquad , \qquad \omega = 2v_+\left(\frac{E\delta_+^0}{E_1}\right)^2$$

2) $n_- \gg n_+$, given δ_-^0,

$$\frac{\operatorname{Re} Z}{Z_0} = 2 - \frac{\vartheta_+\beta_+}{Lv_+} + \frac{\vartheta_+\beta_+}{Lv_+}\left(\frac{3\omega}{v_+}\sin\theta + \ln\theta\right) - \frac{E_0^2}{(E_\delta^0)}\left(\frac{\omega}{v_+}\sin\theta + \ln\theta\right) = 0$$

$$\frac{\operatorname{Im} Z}{Z_0} = -\frac{3\vartheta_+\beta_-\omega}{Lv_+^2} - \frac{\vartheta_+\beta_+}{Lv_+}(\sin\theta + 3\cos\theta) + \frac{E_0^2}{E_{\delta+}^0}\left(\sin\theta + \frac{\omega}{v_+}\ln\theta\right) + 1 = 0$$

(38)

$$\frac{1}{E^2(\delta_+^L)} = \frac{\mu_+\mu_-\beta_- e\delta_-^0}{Lv_+}$$

From the solution (38) we easily obtain

$$\frac{\omega}{v_+} = \frac{1}{6} \ll 1; \qquad E_0 = \frac{Lv_+}{6\mu_+\beta_-}$$

3) $n_- \ll n_+$, given δ_-^L,

$$\frac{\operatorname{Re} Z}{Z_0} = 2 - a - \frac{E_0^2}{E^2(\delta_-^L)} - \frac{E_0^2}{E^2(\delta_-^L)}\left(\frac{\omega}{v_+}\sin\theta - \ln\theta\right) = 0$$

$$\frac{ImZ}{Z_0} = b - \frac{E_0^2}{E^2(\delta^L_-)} - \frac{\vartheta_+\beta_+}{LV_+}\frac{\omega}{V_+} + \frac{E_0^2}{E^2(\delta^L_-)}\left(sin\,\theta + \frac{\omega}{V_+}ln\,\theta\right) = 0 \tag{39}$$

$\theta = 2\pi$ from (39) obtain:

$$\frac{\omega}{V_+} = \frac{1}{\beta_-}\frac{\mathcal{V}_+^2}{\mathcal{V}_-\mathcal{V}_+^E} \ll 1; \qquad E_0 = E_\delta\left(\frac{2}{\beta_-}\frac{\mathcal{V}_+^2}{\mathcal{V}_-\mathcal{V}_+^E}\right)^{\frac{1}{2}}$$

4) $n_- \ll n_+,$ given $\delta^L_+,$

$$\frac{ReZ}{Z_0} = 2 - a - \frac{E_0^2}{E^2(\delta^L_+)} - \frac{E_0^2}{E^2(\delta^L_+)}(sin\,\theta - cos\,\theta) + \frac{E_0}{E_1}(sin\,\theta + cos\,\theta) = 0$$

$$\frac{ImZ}{Z_0} = b - \frac{E_0}{E_1}\left(sin\,\theta + \frac{2\omega}{V_+}ln\,\theta\right) + \frac{E_0^2}{E^2(\delta^L_+)}\left(sin\,\theta + \frac{\omega}{V_+}ln\,\theta\right) + 1 = 0 \tag{40}$$

From solving (40) given:

$$E_0 = 2E_\delta, \qquad \frac{\omega}{V_+} = \frac{E_1}{E_\delta} \ll 1.$$

DISCUSSION

The analysis of all results in a high-frequency limit leads to a following conclusion. In a high-frequency limit (frequency it is much more than fluctuation of a current than all characteristic frequencies entering into theories) is possible supervision of several areas of instability. These areas essentially depend on value of concentration of carriers of a current, from value of an external electric field, from frequency of fluctuations. Dependence of these observable areas of instability on factors intentions proves only at a high level of injection at eυ±δ±0, L~1 fluctuations in-external a circuit, both in high-frequency, and in a low-frequency limit. Conditions of occurrence of these fluctuations depend on different parities of equilibrium concentration of carriers and different values of an external constant electric field and slightly depend on factors of injection. At very greater levels of injection of a condition of occurrence of these fluctuations depend strongly on factors of injection.

THE RESUME

In semiconductors with two types of carriers of a charge (electrons and holes) deep traps, construct the theory of external instability by calculation of an impedance of an image. At negative value of an actual part of an impedance frequencies of fluctuation of a current, value of an external electric field are calculated. We shall find some areas of external instability of existence of fluctuation of a current in semiconductors with deep traps with the certain concentration. Concentration of deep carriers (N, N-) , (n, n-) change a sign on an electric charge at availability recombination and generation of free carriers. Some values of a parity of free carriers of a charge in which are certain, fluctuations of a current appear in-external a circuit. Are certain, that fluctuations of a current very slightly depend on appropriating factors of injection if the inequality eυ±δ±0, L 1 is satisfied. At the return an inequality eυ±δ±0, L~1 critical value of an external electric field and frequency of fluctuation of a current very strongly change

REFERENCES

1. Nonlinear Oscillations of the Charge Curriers Concentration and Electric Fieldin Semiconductors With Deep Traps. F.F. Aliyev, E.R. Hasanov,10SR Journal of applied Physics (10SR-JAP) e-ISSN. 2278-4861. Volume 10. ISUE 1. Yer. II (Jan-Feb 2018) PP 36-42.

2. Электрические домены в полупроводниках с горячили электронами *В.Л. Бонч-Бруевич* ФТТ. Т. 2. 1986. Стр.356.

3. Доменная электрическая неустойчивость в полупроводниках. *В.Л. Бонч-Бруевич., И.П. Звягин А.Г. Миронов* издательство «Наука» Москва 1972. стр.34-36.

4. Non-linear electric and magnetic fieldof radiation *E.R. Hasanov. R.K. Mustafayeva., A.R. Salimi., S.S. Ahadova., K.N. Yusifova* 13th international Conference on «Technical and Physical Problems of Electrical Engineering». 21-22 September 2017. Pages 201-204.

5. Internal and external instability in low- dimensional conducting medias, E.R.Hasanov, R.K.Mustafayeva, IOSR Journal of applied Physics (IOSR-JAP) e-ISSN. 2278-4861. Volume 11. ISSUE 1. Ser. II (Jan-Feb 2019) PP 08-12.

DECAY CHANNELS OF HIGGS BOSONS
$H(h;A) \Rightarrow \gamma\gamma$, $H(h;A) \Rightarrow \gamma Z$, $H^{\pm} \Rightarrow \gamma W^{\pm}$

ABDULLAYEV S. K., OMAROVA E.SH.

Baku State University

Baku / AZERBAIJAN

sabdullayev@bsu.edu.az, emiliya.abdullayeva@inbox.ru

ABSTRACT

Within the framework of the Minimal Supersymmetric Standard Model, the channels of the Higgs boson decay into photons, photon, and gauge boson are investigated: $H(h;A) \Rightarrow \gamma\gamma$, $H(h;A) \Rightarrow \gamma Z$, $H^{\pm} \Rightarrow \gamma W^{\pm}$. In these decays, fermion, $W^{\pm}$-boson, $H^{\pm}$-Higgs boson, scalar fermion, and chargino loop diagrams are considered. For particles with spin $1/2$, 1 and 0 formfactors were found and their dependence on the variable $\tau = M_H^2 / 4m^2$ was studied, where M_H is the mass of the decaying Higgs boson, and m is the mass of the particle corresponding to the loop. Taking into account the circular polarization of photons, analytical expressions for the decay widths of the Higgs boson are obtained. It is established that photons in decays $H(h;A) \Rightarrow \gamma\gamma$ should have the same circular polarizations: $l_1 = l_2 = \pm 1$.

Keywords: Minimal Supersymmetric Standard Model, Higgs-boson, decay width, photon, coupling constant.

HİQQS BOZONLARIN ÇEVRİLMƏ KANALLARI $H(h;A) \Rightarrow \gamma\gamma$, $H(h;A) \Rightarrow \gamma Z$, $H^{\pm} \Rightarrow \gamma W^{\pm}$

XÜLASƏ

Minimal Supersymmetrik Standart Model çərçivəsində Hiqqs bozonların fotonlara, foton və kalibrləmə bozonuna çevrilmə kanallarıtədqiq edilmişdir: $H(h;A) \Rightarrow \gamma\gamma$, $H(h;A) \Rightarrow \gamma Z$, $H^{\pm} \Rightarrow \gamma W^{\pm}$. Bu çevrilmə kanallarında fermion, $W^{\pm}$-bozon, $H^{\pm}$-Hiqqs bozon, skalyar fermion və çarcino ilgək diaqramları nəzərə alınmışdır. Spini $1/2$, 1 və 0 olan zərrəciklər üçün formfaktorlar müəyyən olunmuş və onların $\tau = M_H^2 / 4m^2$ dəyişənindən aslılığı öyrənilmişdir, burada M_H Hiqqs bozonun, m isə ilgək diaqramına müvafiq olan zərrəciyin kütləsidir. Fotonların dairəvi polarizasiyasını nəzərə alaraq, Hiqqs bozonların çevrilmə kanallarının eni üçün analitik ifadələr əldə edilmişdir. Müəyyən olunmuşdur ki, $H(h;A) \Rightarrow \gamma\gamma$ çevrilmə kanalında fotonlar eyni dairəvi polarizasiyaya malik olmalıdır: $l_1 = l_2 = \pm 1$.

Açar sözlər: Minimal Supersimmetrik Standart Model, Hiqqs bozon, çevrilmənin eni, foton, rabitə sabiti.

КАНАЛЫ РАСПАДА ХИГГС-БОЗОНОВ $H(h;A) \Rightarrow \gamma\gamma$, $H(h;A) \Rightarrow \gamma Z$, $H^{\pm} \Rightarrow \gamma W^{\pm}$

РЕЗЮМЕ

В рамках Минимальной Суперсимметричной Стандартной Модели исследованы каналы распада Хиггс-бозонов на фотоны, на фотон и калибровочный бозон: $H(h;A) \Rightarrow \gamma\gamma$, $H(h;A) \Rightarrow \gamma Z$, $H^{\pm} \Rightarrow \gamma W^{\pm}$. В этих распадах рассмотрены фермионные, $W^{\pm}$ - бозонные, $H^{\pm}$ - Хиггс бозонные, скаляр фермионные и чарджионные петлевые диаграммы. Для частиц со спином $1/2$, 1 и 0 найдены формфакторы и изучена зависимость их от переменной $\tau = M_H^2 / 4m^2$, где M_H – масса распадающего Хиггс бозона, а m – масса частицы, соответствующей петле. С учетом циркулярной поляризации фотонов получены аналитические выражения для ширины распадов. Установлено, что фотоны в распадах $H(h;A) \Rightarrow \gamma\gamma$ должны обладать одинаковыми циркулярными поляризациями: $l_1 = l_2 = \pm 1$.

Ключевые слова: Минимальная Суперсимметричная Стандартная Модель, Хиггс-бозон, ширина распада, фотон, константа связи.

1. Introduction

The Standard model (SM), based on the local gauge symmetry $SU_C(3) \times SU_L(2) \times U_Y(1)$, describes well the physics of strong and electroweak interactions between quarks, leptons and gauge bosons [1–4]. A doublet of scalar fields $\varphi = \begin{pmatrix} \varphi^+ \\ \varphi^0 \end{pmatrix}$, a neutral component, which has a nonzero vacuum value, is introduced into the model. As a result of spontaneous symmetry breaking due to quantum excitations of the scalar field, the standard Higgs boson H_{SM} appears, and due to the interaction with this field, the gauge bosons ($W^\pm, Z^0$), quarks and charged leptons acquire mass. This mechanism of particle mass generation is known as the mechanism of spontaneous breaking of Higgs symmetry [5, 6]. The discovery of the Higgs boson H_{SM} with characteristics corresponding to the predictions of the SM was carried out by the ATLAS and CMS collaborations in 2012 at the Large Hadron Collider (LHC) at CERN [7,8]. With the discovery of the Higgs boson, a new stage began in the study of the properties of fundamental interactions of elementary particles.

Along with the SM, the Minimal Supersymmetric Standard Model (MSSM) is widely discussed in the literature [9–12]. It introduces two complex Higgs $SU_L(2)$ doublets with hypercharges –1 and +1:

$$\varphi_1 = \begin{pmatrix} H_1^0 \\ H_1^- \end{pmatrix}, \quad \varphi_2 = \begin{pmatrix} H_2^+ \\ H_2^0 \end{pmatrix}.$$

To obtain the physical fields of the Higgs boson, the fields φ_1 and φ_2 are written as

$$\varphi_1 = \frac{1}{\sqrt{2}} \begin{pmatrix} \upsilon_1 + H_1^0 + iP_1^0 \\ H_1^- \end{pmatrix}, \quad \varphi_2 = \frac{1}{\sqrt{2}} \begin{pmatrix} H_2^+ \\ \upsilon_2 + H_2^0 + iP_2^0 \end{pmatrix},$$

where H_1^0, P_1^0, H_2^0 and P_2^0 are real fields describing the system excitations with respect to the vacuum states $\langle \varphi_1 \rangle = \frac{1}{\sqrt{2}} \upsilon_1$ and $\langle \varphi_2 \rangle = \frac{1}{\sqrt{2}} \upsilon_2$. The CP-even Higgs bosons H and h are obtained by mixing the fields H_1^0 and H_2^0 (mixing angle α):

$$\begin{pmatrix} H \\ h \end{pmatrix} = \begin{pmatrix} \cos\alpha & \sin\alpha \\ -\sin\alpha & \cos\alpha \end{pmatrix} \begin{pmatrix} H_1^0 \\ H_2^0 \end{pmatrix}.$$

Similarly mix the fields P_1^0 and P_2^0, $H_1^\pm$ and $H_2^\pm$ (mixing angle β):

$$\begin{pmatrix} G^0 \\ A \end{pmatrix} = \begin{pmatrix} \cos\beta & \sin\beta \\ -\sin\beta & \cos\beta \end{pmatrix} \begin{pmatrix} P_1^0 \\ P_2^0 \end{pmatrix}, \quad \begin{pmatrix} G^\pm \\ H^\pm \end{pmatrix} = \begin{pmatrix} \cos\beta & \sin\beta \\ -\sin\beta & \cos\beta \end{pmatrix} \begin{pmatrix} H_1^\pm \\ H_2^\pm \end{pmatrix}.$$

Here, A is a CP-odd Higgs boson, $H^\pm$ is charged Higgs bosons, G^0 and $G^\pm$ are neutral and charged Goldstone bosons.

Thus, after spontaneous symmetry breaking, five Higgs particles appear in the MSSM: CP-even H - and h -bosons, CP-odd A -boson, and charged $H^\pm$ -bosons. In the MSSM, the Higgs sector is characterized by six parameters $M_H, M_h, M_A, M_{H^\pm}, \alpha$ and β. Of these, the parameters M_A and $tg\beta$ are free. Masses M_H and M_h (M_{H^+} and M_{H^-}) are expressed by masses M_A and M_Z (M_A and M_W) [9,10]:

$$M_{H(h)}^2 = \frac{1}{2}\left[M_A^2 + M_Z^2 \pm \sqrt{(M_A^2 + M_Z^2)^2 - 4M_A^2 M_Z^2 \cos^2 2\beta} \right], \quad M_{H^{\pm}}^2 = M_A^2 + M_W^2$$

The mixing angles of fields α and β are related by

$$\text{tg}2\alpha = \text{tg}2\beta \cdot \frac{M_A^2 + M_Z^2}{M_A^2 - M_Z^2}, \quad \left(-\frac{\pi}{2} \leq \alpha < 0 \right).$$

Higgs bosons H, h, A and $H^{\pm}$ – can decay through various channels [10]. Previous works [13–17] are devoted to the study of the H, h, A and $H^{\pm}$ decays of the bosons into a fermion pair, into a gauge boson and a fermion pair, into gauge bosons, and also into decays of light Higgs bosons. In the present work, we study the decays of the Higgs bosons H, h, A and $H^{\pm}$ into photons, into a photon and the gauge boson:

$$H(h; A) \Rightarrow \gamma + \gamma, \tag{1a}$$

$$H(h; A) \Rightarrow \gamma + Z, \tag{1b}$$

$$H^{\pm} \Rightarrow \gamma + W^{\pm}. \tag{1c}$$

Analytical expressions for the widths of these decays are obtained, the dependence of the decay width on the Higgs boson mass is studied.

2. Decays $\Phi \Rightarrow \gamma + \gamma$ ($\Phi = H; h$)

Photons are massless particles, they do not directly interact with the Higgs bosons. Decays (1a) go through loop diagrams with charged particles. First, we consider the fermion loop diagrams shown in Fig. 1a) and b) (4-particle momenta are written in brackets). As is known, the Higgs-boson interaction with the fermion is the greater, the greater its mass, so we can assume that the loop belongs to the heavy $t(b)$-quark, or the τ-lepton.

The matrix element corresponding to the diagram a) Fig.1 can be written as:

$$M_a(\Phi \to \gamma\gamma) = N_C e^2 Q_f^2 \cdot [\sqrt{2}G_F]^{1/2} m_f \cdot g_{\Phi ff} e_\mu^*(k_1) e_\nu^*(k_2) \cdot I_{\mu\nu}, \tag{2}$$

where m_f and Q_f –mass and charge of fermion, G_F – Fermi constant of weak interactions, $g_{\Phi ff}$ – the Higgs-boson coupling constant with the fermion pair, normalized to the standard Higgs-boson coupling constant SM $g_{H_{SM}ff} = [\sqrt{2}G_F]^{1/2} m_f$ (see Table 1), N_C – color factor ($N_C = 1$ with lepton loop and $N_C = 3$ – with quark loop), $e_\mu^*(k_1)$ and $e_\nu^*(k_2)$ – 4-photon polarization vectors, and tensor $I_{\mu\nu}$ has the form

$$I_{\mu\nu} = \int \frac{d^4k}{(2\pi)^4} \cdot \frac{Sp[\gamma_\mu(\hat{k} + \hat{k}_1 + m_f)(\hat{k} - \hat{k}_2 + m_f)\gamma_\nu(\hat{k} + m_f)]}{(k^2 - m_f^2)[(k + k_1)^2 - m_f^2][(k - k_2)^2 - m_f^2]}. \tag{3}$$

We define the trace of the product of Dirac matrices:

$$Sp[\gamma_\mu(\hat{k} + \hat{k}_1 + m_f)(\hat{k} - \hat{k}_2 + m_f)\gamma_\nu(\hat{k} + m_f)] = 4m_f T_{\mu\nu},$$

where

$$T_{\mu\nu} = g_{\mu\nu}[m_f^2 - k^2 - (k_1 \cdot k_2)] + 4k_\mu k_\nu - 2k_\mu k_{2\nu} + 2k_\nu k_{1\mu} - k_{1\mu}k_{2\nu} + k_{2\mu}k_{1\nu}. \tag{4}$$

Using the Feynman integration technique

$$\frac{1}{ABC} = \int\limits_0^1 dx \int\limits_0^1 dy \int\limits_0^1 dz \, \delta(x+y+z-1) \cdot \frac{2}{(Ax+By+Cz)^3}, \tag{5}$$

to calculate the integral (3), here we have taken the notation

$$A = k^2 - m_f^2,$$

$$B = (k+k_1)^2 - m_f^2 = k^2 + 2(k \cdot k_1) - m_f^2, \tag{6}$$

$$C = (k-k_2)^2 - m_f^2 = k^2 - 2(k \cdot k_2) - m_f^2.$$

Then the denominator of the integral (3) takes the form:

$$(Ax+By+Cz)^3 = [(k^2 - m_f^2)x + (k^2 + 2(k \cdot k_1) - m_f^2)y +$$

$$+ (k^2 - 2(k \cdot k_2) - m_f^2)z]^3 = [(k+k_1 y - k_2 z)^2 - b^2]^3,$$

where it is taken into account that $k_1^2 = k_2^2 = 0$, $x+y+z=1$ and the designation $b^2 = m_f^2 - 2(k_1 \cdot k_2) yz$ is entered.

Thus, the integral (3) takes the form:

$$I_{\mu\nu} = \int \frac{d^4 k}{(2\pi)^4} \cdot \int\limits_0^1 dy \int\limits_0^{1-y} dz \cdot \frac{8 m_f T_{\mu\nu}}{[(k+k_1 y - k_2 z)^2 - b^2]^3}. \tag{7}$$

We make the replacement of the integration variable $k \Rightarrow (k - k_1 y + k_2 z)$ and discard the linear in terms of k odd terms, then the expression for the integral (7) is obtained (we also take into account the photon transverse conditions ($\varepsilon_\mu^*(k_1) k_{1\mu} = \varepsilon_\nu^*(k_2) k_{2\nu} = 0$):

$$I_{\mu\nu} = \int \frac{d^4 k}{(2\pi)^4} \cdot \int\limits_0^1 dy \int\limits_0^{1-y} dz \cdot \frac{8 m_f \cdot T'_{\mu\nu}}{(k^2 - b^2)^3}, \tag{8}$$

where

$$T'_{\mu\nu} = 4 k_\mu k_\nu - k^2 g_{\mu\nu} + k_{2\mu} k_{1\nu}(1 - 4yz) + g_{\mu\nu}[m_f^2 - (k_1 \cdot k_2)(1 - 2yz)]. \tag{9}$$

Table 1. Coupling constants of Higgs bosons in the MSSM

Φ	$g_{\Phi tt} / g_{H_{SM}tt}$	$g_{\Phi bb} / g_{H_{SM}bb}$	$g_{\Phi\tau\tau} / g_{H_{SM}\tau\tau}$	$g_{\Phi WW} / g_{H_{SM}WW}$
H	$\dfrac{\sin\alpha}{\sin\beta}$	$\dfrac{\cos\alpha}{\cos\beta}$	$\dfrac{\cos\alpha}{\cos\beta}$	$\cos(\beta-\alpha)$
h	$\dfrac{\cos\alpha}{\sin\beta}$	$-\dfrac{\sin\alpha}{\cos\beta}$	$-\dfrac{\sin\alpha}{\cos\beta}$	$\sin(\beta-\alpha)$
A	$ctg\beta$	$tg\beta$	$tg\beta$	0

Figure.1. Feynman loop diagrams for decay $H(h;A) \rightarrow \gamma\gamma$
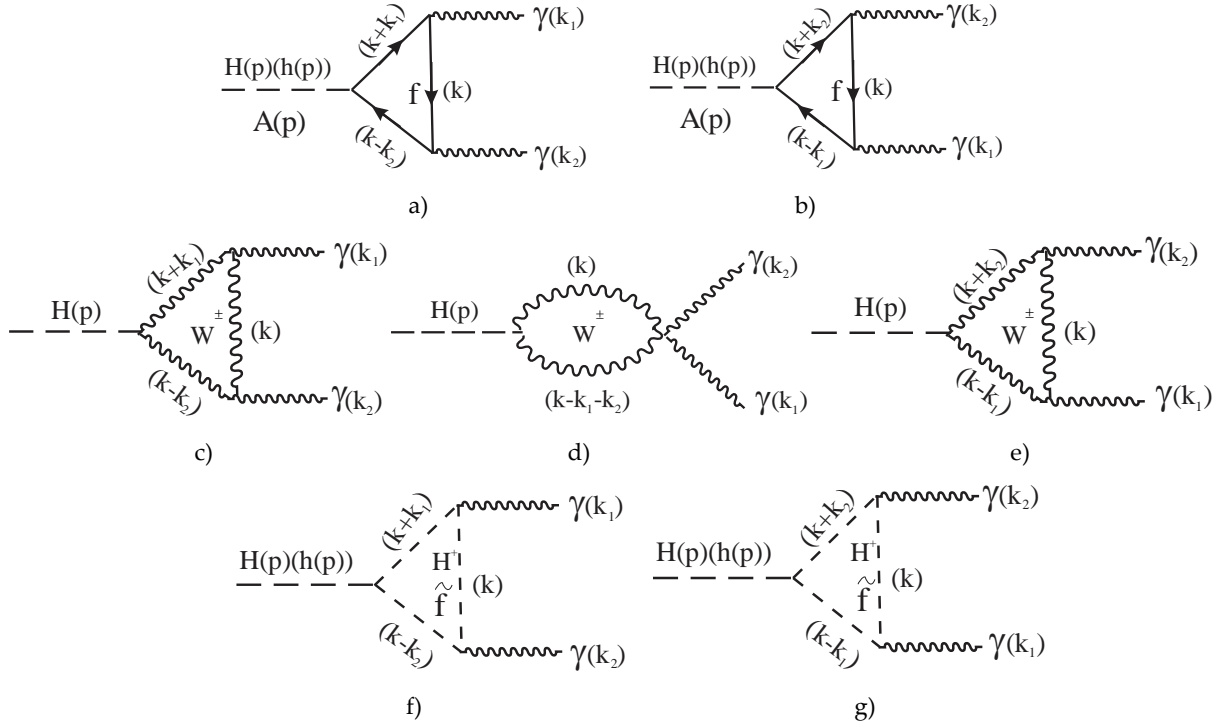
The integrals with respect to in (8) are easily calculated:

$$\int \frac{d^4 k}{(2\pi)^4} \cdot \frac{4k_\mu k_\nu - k^2 g_{\mu\nu}}{(k^2 - b^2)^3} = \frac{i}{32\pi^2} \cdot g_{\mu\nu}, \int \frac{d^4 k}{(2\pi)^4} \cdot \frac{1}{(k^2 - b^2)^3} = -\frac{i}{32\pi^2} \cdot \frac{1}{b^2}. \tag{10}$$

Therefore, for the integral (3) we obtain the expression

$$I_{\mu\nu} = \frac{i m_f}{4\pi^2} [k_{2\mu} k_{1\nu} - (k_1 \cdot k_2) g_{\mu\nu}] \cdot I, \tag{11}$$

where

$$I = \int_0^1 dy \int_0^{1-y} dz \cdot \frac{1 - 4yz}{2(k_1 \cdot k_2) yz - m_f^2} = \frac{1}{M_\Phi^2} \int_0^1 dy \int_0^{1-y} dz \cdot \frac{1 - 4yz}{yz - m_f^2 / M_\Phi^2} = \frac{1}{M_\Phi^2} \cdot I_0. \tag{12}$$

The amplitude corresponding to the second diagram b) is determined similarly. Calculations show that the amplitude of this diagram also produces the same expression as for diagram a). Therefore, the total decay amplitude of the $\Phi \Rightarrow \gamma + \gamma$ $(\Phi = H; h)$ is equal to

$$M(\Phi \rightarrow \gamma\gamma) = \frac{i m_f^2 N_C e^2 Q_f^2}{2\pi^2 M_\Phi^2} [\sqrt{2} G_F]^{1/2} \cdot g_{\Phi ff}^2 e_\mu^*(k_1) \cdot e_\nu^*(k_2) \cdot [k_{2\mu} k_{1\nu} - (k_1 \cdot k_2) g_{\mu\nu}] \cdot I_0. \tag{13}$$

The squared transition amplitude of the process is given by:

$$|M(\Phi \rightarrow \gamma\gamma)|^2 = \left(\frac{N_C e^2 Q_f^2}{2\pi^2}\right)^2 \cdot \sqrt{2} G_F \cdot \left(\frac{m_f^2}{M_\Phi^2}\right)^2 \cdot |I_0|^2 [(e^*(k_1) \cdot k_2)(e^*(k_2) \cdot k_1) -$$

$$- (k_1 \cdot k_2)(e^*(k_1) \cdot e^*(k_2))][(e(k_1) \cdot k_2)(e(k_2) \cdot k_1) - (k_1 \cdot k_2)(e(k_1) \cdot e(k_2))].$$

The 4-vector polarization of a photon with circular polarization can be written as $e_\mu^*(k_1) = (0, \vec{e}^*(k_1))$, where

$$\vec{e}^*(k_1) = \frac{1}{\sqrt{2}}(\vec{\beta} - il_1[\vec{n}_1\vec{\beta}]),\tag{14}$$

$\vec{n}_1$ is unit vector in the direction of the photon momentum, $\vec{\beta}$ is a unit vector perpendicular to the photon momentum $((\vec{\beta}\vec{n}_1) = 0)$, $l_1 = \pm 1$ characterizes the circular polarization of the photon, and for $l_1 = +1(-1)$, the photon has right (left) circular polarization.

For the width of the $H(h)$ Higgs boson decayinto circularly polarized photons, we obtained the expression [18]:

$$\Gamma(\Phi \to \gamma\gamma) = \frac{G_F \alpha_{KED}^2 M_\Phi^3}{512\sqrt{2}\pi^3} \cdot (1 + l_1 l_2)\left|\sum_f N_C Q_f^2 g_{\Phi ff} A_{1/2}^\Phi(\tau_f)\right|^2,\tag{15}$$

where the summation is carried out over loop fermions, l_1 andl_2 arecircular polarizations of photons,, $A_{1/2}^\Phi(\tau_f)$ is a formfactor of a spin $1/2$ fermion

$$A_{1/2}^\Phi(\tau_f) = \frac{2}{\tau_f^2}[\tau_f + (\tau_f - 1)f(\tau_f)],\tag{16}$$

$\tau_f = M_\Phi^2/4m_f^2$, and the function $f(\tau_f)$ is determined by the expression

$$f(\tau_f) = \begin{cases} \arcsin^2\sqrt{\tau_f} & , if \ \tau_f \leq 1, \\ -\dfrac{1}{4}\left[\ln\dfrac{1 + \sqrt{1 - \tau_f^{-1}}}{1 - \sqrt{1 - \tau_f^{-1}}} - i\pi\right]^2 & , if \ \tau_f > 1. \end{cases}\tag{17}$$

From the decay width (15), it follows that photons should have either the right ($l_1 = l_2 = +1$), or the left ($l_1 = l_2 = -1$) circular polarization. The state in which one of the photons has a right and the other a left circular polarization is forbidden by the law of conservation of the total moment.

Note that for $\tau_f \leq 1$ the $A_{1/2}^\Phi(\tau_f)$ formfactor is real, and for $\tau_f > 1$ it is complex. Figure2 a) shows the dependence of real $\mathrm{Re}(A_{1/2}^\Phi(\tau_f))$ andimaginary $\mathrm{Im}(A_{1/2}^\Phi(\tau_f))$ parts of the formfactor as a function of τ_f. At $\tau_f \Rightarrow 0$ the real part of the formfactor approaches the value $4/3$, increases with τ_f and reaches a maximum near $\tau_f \approx 1$, and with further increase in τ_f $\mathrm{Re}(A_{1/2}^\Phi(\tau_f))$ gradually decreases to zero. As for the imaginary part of the formfactor $\mathrm{Im}(A_{1/2}^\Phi(\tau_f))$, then at $\tau_f = 1$it is zero, with increasing τ_f $\mathrm{Im}(A_{1/2}^\Phi(\tau_f))$increases, it reaches a maximum at $\tau_f \cong 3$, and then slowly decreases.

Figure. 2. Formfactors for loop particles with spins $1/2$, 1 and 0

a)

b)

c)

d)
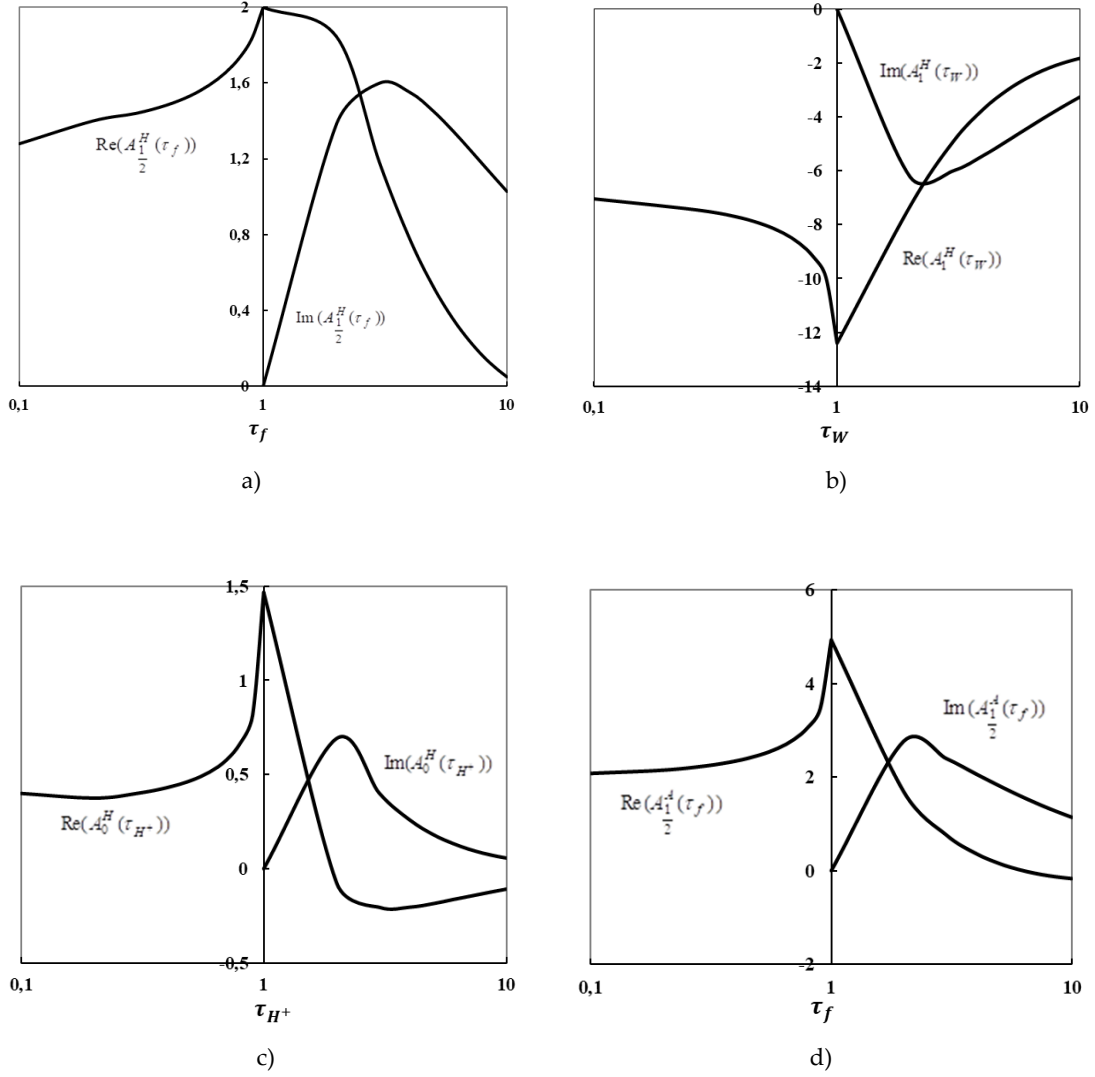
Summing over the circular polarizations of the photons, for the decay width $\Phi \rightarrow \gamma + \gamma$ we get:

$$\Gamma(\Phi \rightarrow \gamma\gamma) = \frac{G_F \alpha_{KED}^2 M_{\Phi}^3}{128\sqrt{2}\pi^3} \cdot \left| \sum_f N_C Q_f^2 g_{\Phi ff} A_{1/2}^{\Phi}(\tau_f) \right|^2 . \tag{18}$$

In Figure 3 shows the dependence of the decaywidth $H \rightarrow \gamma + \gamma$ on the Higgs boson mass at the value of the parameter $tg\beta = 3$. We considered that the loop belongs to the t-quarkwith the mass $m_t = 173,2\,\text{GeV}$. As can be seen, with increasing Higgs boson mass M_H the decay width $\Gamma(H \rightarrow \gamma\gamma)$ increases.

45

Figure 3. Dependence of the decay width $H \Rightarrow \gamma\gamma$ and $A \Rightarrow \gamma\gamma$
on the Higgs-boson mass (t - quark loop diagrams)
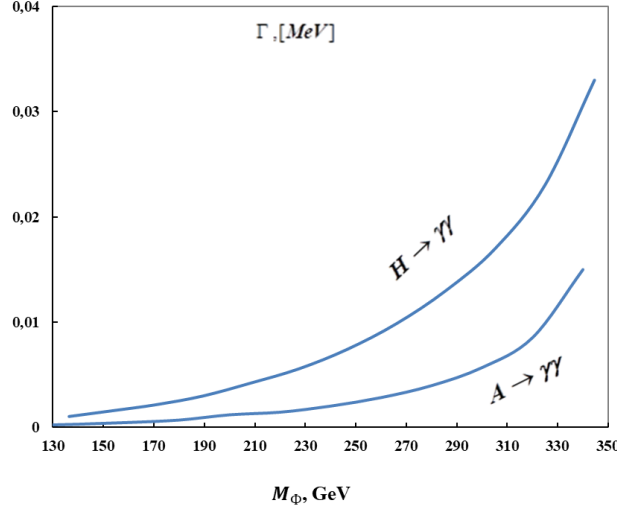
We note that the $H(h) \rightarrow \gamma + \gamma$ decay is contributed by diagrams with charged $W^\pm$- boson loops. In the unitary calibration of all there are three Feynman diagrams, shown in Figure 1 c), d) and e). For the contribution to the decay width of the $\Phi \Rightarrow \gamma + \gamma$ $W^\pm$ - boson loop diagrams, we get the expression:

$$\Gamma(\Phi \rightarrow \gamma\gamma) = \frac{G_F \alpha_{KED}^2 M_\Phi^3}{128\sqrt{2}\pi^3} \cdot g_{\Phi WW}^2 \cdot \left| A_1^\Phi(\tau_W) \right|^2, \tag{19}$$

where

$$A_1^\Phi(\tau_W) = -\frac{1}{\tau_W^2}[2\tau_W^2 + 3\tau_W + 3(2\tau_W - 1)f(\tau_W)] \tag{20}$$

is W - boson loop formfactor, $\tau_W = M_\Phi^2 / 4M_W^2$, $g_{\Phi WW}$ is coupling constant Φ -boson with

W -boson pair, normalized to coupling constant $g_{H_{SM}WW}$ (see Table 1).

Figure 2 b) shows the dependence of $\mathrm{Re}(A_1^\Phi(\tau_W))$ and $\mathrm{Im}(A_1^\Phi(\tau_W))$ on τ_W . As the variable τ_W grows, the real part $\mathrm{Re}(A_1^\Phi(\tau_W))$ decreases and reaches a minimum at $\tau_W = 1$, and a further increase in τ_W leads to an increase in the real part of the formfactor. A similar dependence is also observed for the imaginary part of the form- factor $\mathrm{Im}(A_1^\Phi(\tau_W))$.

Figure 4. illustrates the dependence of the width of the decay $H \Rightarrow \gamma + \gamma$, due to W - boson loop diagrams.

$\Phi \Rightarrow \gamma + \gamma$ contributes to the decay with charged Higgs-boson loop diagrams (Feynman diagrams f) and g) in Figure 1). The matrix element corresponding to these diagrams is:

$$M(\Phi \rightarrow \gamma\gamma) = (-ie)^2 \lambda_{\Phi H^+ H^-} e_\mu^*(k_1) e_\nu^*(k_2)[\sqrt{2}G_F]^{1/2} M_Z^2 \times$$

$$\times \int \frac{d^4 k}{(2\pi)^4} \cdot \frac{8k_\mu k_\nu}{(k^2 - M_{H^\pm}^2)[(k+k_1)^2 - M_{H^\pm}^2][(k-k_2)^2 - M_{H^\pm}^2]},$$

46

where $\lambda_{\Phi H^+ H^-}$ is coupling constant in Φ-boson ($\Phi = H; h$) with charged $H^+ H^-$-bosons. According to the MSSM, this coupling constant depends on the parameters α, β and $x_W = \sin^2 \theta_W$ (θ_W is the Weinberg angle) [10]:

$$\lambda_{HH^+H^-} = -\cos 2\beta \cos(\beta + \alpha) + 2(1 - x_W)\cos(\beta - \alpha),$$

$$\lambda_{hH^+H^-} = \cos 2\beta \sin(\beta + \alpha) + 2(1 - x_W)\sin(\beta - \alpha).$$

Further calculation of the decay width of $\Phi \Rightarrow \gamma + \gamma$ in the case of charged Higgs-boson loop diagrams is carried out similarly to the above method and for the width of this decay the expression is obtained:

$$\Gamma(\Phi \to \gamma\gamma) = \frac{G_F \alpha_{KED}^2 M_\Phi^3}{512\sqrt{2}\pi^3} \cdot \frac{M_Z^4}{M_{H^\pm}^4} \lambda_{\Phi H^+H^-}^2 \cdot \left| A_0^\Phi(\tau_{H^\pm}) \right|^2. \tag{21}$$

Here

$$A_0^\Phi(\tau_{H^\pm}) = \frac{1}{\tau_{H^\pm}^2}[f(\tau_{H^\pm}) - \tau_{H^\pm}] \tag{22}$$

is a formfactor of zero spin particle, $\tau_{H^\pm} = M_\Phi^2 / 4M_{H^\pm}^2$.

On figure 2 c) shows the dependence of the real $\mathrm{Re}(A_0^\Phi(\tau_{H^\pm}))$ and imaginary $\mathrm{Im}(A_0^\Phi(\tau_{H^\pm}))$ parts of the formfactor on the variable $\tau_{H^\pm}$.

Figure 4. Dependence of the decay width $H \Rightarrow \gamma\gamma$ on the mass M_H ($W^\pm$- boson loop diagrams)
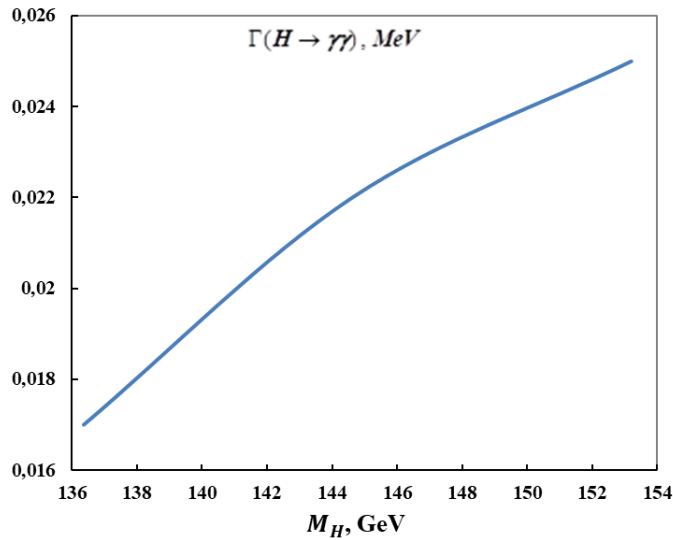
The Feynman loop diagrams of supersymmetric particles can contribute to the decay width $H(h) \Rightarrow \gamma + \gamma$ It is known that the MSSM, like the SM, is based on the $SU_C(3) \times SU_L(2) \times U_Y(1)$ gauge symmetry group. Supersymmetry suggests that gauge bosons with spin 1 ($B, W^\pm, W^0, g$) and their spin 1/2 ($\tilde{B}, \tilde{W}^\pm, \tilde{W}^0, \tilde{g}$) superpartners make up the vector superfield (see Table 2).

Table 2. Fields of the gauge supermultiplet in the MSSM

Name	Spin $\frac{1}{2}$	Spin 1	$SU_C(3)$	$SU_L(2)$	$U_Y(1)$
Gluino, Gluons	$\tilde{g}$	g	8	1	0
Wino, W -bosons	$\tilde{W}^{\pm}, \tilde{W}^0$	$W^{\pm}, W^0$	1	3	0
Bino, B -boson	$\tilde{B}$	B	1	1	0

In the MSSM, as in the SM, there are only three generations of leptons and quarks (the right neutrino is absent). The superpartners of fermions and Higgs bosons in the MSSM are presented in Table 3.

Table 3. Superpartners of fermions and Higgs-bosons in MSSM

Superfields	The composition of the particles	$SU_C(3)$	$SU_L(2)$	$U_Y(1)$
$\hat{Q}$	$(u_L, d_L), (\tilde{u}_L, \tilde{d}_L)$	3	2	1/3
$\hat{U}^c$	$u_R, \ \tilde{u}_R^*$	3	1	$-4/3$
$\hat{L}$	$(v_L, e_L), (\tilde{v}_L, \tilde{e}_L)$	1	2	–1
$\hat{E}^c$	$\bar{e}_R, \ \tilde{e}_R^*$	1	1	2
$\hat{H}_1$	$(H_1, \tilde{H}_1)$	1	2	–1
$\hat{H}_2$	$(H_2, \tilde{H}_2)$	1	2	1

The neutral Higgsino and the neutral gaugino $\tilde{B}$ and $\tilde{W}^0$ are mixed and four mass states, called neutralino $\tilde{\chi}_i^0$ $(i=1,2,3,4)$ appear. Neutralino charge analogs are called charginos: two of them are positively charged and two are negatively charged $\tilde{\chi}_{1,2}^{\pm}$.

Contributions of diagrams with scalar fermion loops (diagrams f) and g) in Figure 1 contribute to the decay width $H(h) \rightarrow \gamma + \gamma$. The contribution of these diagrams to the width of the decay $H(h) \rightarrow \gamma + \gamma$ is given by a formula similar to (21):

$$\Gamma(\Phi \rightarrow \gamma\gamma) = \frac{G_F \alpha_{KED}^2 M_\Phi^3}{512\sqrt{2}\pi^3} \cdot M_Z^4 \cdot \left| \sum_{\tilde{f}} \frac{N_C Q_{\tilde{f}}^2}{m_{\tilde{f}}^2} g_{\Phi\tilde{f}\tilde{f}} A_0^\Phi(\tau_{\tilde{f}}) \right|^2 . \tag{23}$$

Here $m_{\tilde{f}}$ is a mass of scalar fermion and $\tau_{\tilde{f}} = M_\Phi^2 / 4m_{\tilde{f}}^2$.

Chargino loop diagrams also contribute to the Higgs-boson decay $H(h) \rightarrow \gamma + \gamma$. The decay widths of $\Gamma(\Phi \rightarrow \gamma\gamma)$, due to these diagrams, are given by the formula:

$$\Gamma(\Phi \rightarrow \gamma\gamma) = \frac{G_F \alpha_{KED}^2}{128\sqrt{2}\pi^3} M_\Phi^3 \cdot \left| \sum_{\tilde{\chi}_i^{\pm}} \frac{2M_W}{m_{\tilde{\chi}_i^{\pm}}} g_{\Phi\tilde{\chi}_i^+\tilde{\chi}_i^-} A_{1/2}^\Phi(\tau_{\tilde{\chi}_i^{\pm}}) \right|^2 , \tag{24}$$

where $m_{\tilde{\chi}_i^{\pm}}$ is the mass of chargino, $g_{\Phi\tilde{\chi}_i^+\tilde{\chi}_i^-}$ is coupling constant Φ -boson with $\tilde{\chi}_i^+\tilde{\chi}_i^-$ pair and $\tau_{\tilde{\chi}_i^{\pm}} = M_\Phi^2 / 4m_{\tilde{\chi}_i^{\pm}}^2$.

Along with the above contributions of individual loop diagrams to the decay width $H(h) \rightarrow \gamma + \gamma$ there are also contributions due to the interference of these diagrams. Taking into account the interference of the Feynman diagrams, the width of the decay is determined by the following expression (the amplitudes of all the loop diagrams are coherently added):

$$\Gamma(\Phi \rightarrow \gamma\gamma) = \frac{G_F \alpha_{KED}^2 M_\Phi^3}{128\sqrt{2}\pi^3} \cdot \left| \sum_f N_C Q_f^2 g_{\Phi ff} A_{1/2}^\Phi(\tau_f) + \frac{M_Z^2 \lambda_{\Phi H^+ H^-}}{2M_{H^\pm}^2} A_0^\Phi(\tau_{H^\pm}) + \right.$$

$$\left. + \sum_{\tilde{f}_i} \frac{N_C Q_{\tilde{f}_i}^2}{m_{\tilde{f}_i}} g_{\Phi \tilde{f}_i \tilde{f}_i} A_0^\Phi(\tau_{\tilde{f}_i}) + g_{\Phi WW} A_1^\Phi(\tau_W) + \sum_{\tilde{\chi}_i^\pm} \frac{2M_W}{m_{\tilde{\chi}_i^\pm}} g_{H \tilde{\chi}_i^+ \tilde{\chi}_i^-} A_{1/2}^\Phi(\tau_{\tilde{\chi}_i^\pm}) \right|^2 . \tag{25}$$

2. Decay $A \Rightarrow \gamma + \gamma$

The fermion loop diagrams of the decay $A \Rightarrow \gamma + \gamma$ are shown in Fig.1 a) and b) and these diagrams correspond to the amplitude

$$M(A \Rightarrow \gamma\gamma) = 2N_C e^2 Q_f^2 [\sqrt{2}G_F]^{1/2} m_f \cdot g_{Aff} e_\mu^*(k_1) e_\nu^*(k_2) \cdot J_{\mu\nu}, \tag{26}$$

where, due to the pseudoscalarity of the A boson, the tensor $J_{\mu\nu}$ is determined by the integral

$$J_{\mu\nu} = \int \frac{d^4 k}{(2\pi)^4} \cdot \frac{Sp[\gamma_\mu(\hat{k} + \hat{k}_1 + m_f)\gamma_5(\hat{k} - \hat{k}_2 + m_f)\gamma_\nu(\hat{k} + m_f)]}{(k^2 - m_f^2)[(k + k_1)^2 - m_f^2][(k - k_2)^2 - m_f^2]} . \tag{27}$$

In this case, the trace of the product of Dirac matrices is equal to:

$$Sp[\gamma_\mu(\hat{k} + \hat{k}_1 + m_f)\gamma_5(\hat{k} - \hat{k}_2 + m_f)\gamma_\nu(\hat{k} + m_f)] = 4m_f i\varepsilon_{\mu\nu\rho\sigma} k_{1\rho} k_{2\sigma} .$$

Further calculation of the decay width $A \Rightarrow \gamma + \gamma$ is carried out as in the decay of $H \Rightarrow \gamma + \gamma$ and we get the following result:

$$\Gamma(A \rightarrow \gamma\gamma) = \frac{G_F \alpha_{KED}^2 M_A^3}{512\sqrt{2}\pi^3} \cdot (1 + l_1 l_2) \left| \sum_f N_C Q_f^2 g_{Aff} A_{1/2}^A(\tau_f) \right|^2 , \tag{28}$$

where $A_{1/2}^A(\tau_f)$ is fermion loop formfactor

$$A_{1/2}^A(\tau_f) = \frac{2}{\tau_f} f(\tau_f), \tag{29}$$

$\tau_f = M_A^2 / 4m_f^2$, and the function $f(\tau_f)$ is given by (17).

Figure 2d) illustrates the dependence of $\text{Re}(A_{1/2}^A(\tau_f))$ and $\text{Im}(A_{1/2}^A(\tau_f))$ on τ_f .

The decay width $A \rightarrow \gamma + \gamma$, summed over the polarization states of the photons, is equal to:

$$\Gamma(A \rightarrow \gamma\gamma) = \frac{G_F \alpha_{KED}^2 M_A^3}{8\sqrt{2}\pi^3} \cdot \left| \sum_f N_C Q_f^2 g_{Aff} A_{1/2}^A(\tau_f) \right|^2 . \tag{30}$$

Figure 3. also shows the dependence of the decay width $A \rightarrow \gamma + \gamma$ on the Higgs boson mass at the parameter value $tg\beta = 3$ (the fermion loop belongs to the t - quark). With the inc-

rease Higgs boson mass, the decay width also increases, the decay width $H \to \gamma + \gamma$ prevails over the decay width $A \to \gamma + \gamma$, which is due to a large value of the coupling constant $g_{Htt} > g_{Att}$.

In addition to fermion loop diagrams, the chargino loop diagrams also contribute to the decay $A \Rightarrow \gamma + \gamma$. The decay width $A \Rightarrow \gamma + \gamma$ in the general case is:

$$\Gamma(A \to \gamma\gamma) = \frac{G_F \alpha_{KED}^2 M_\Phi^3}{128\sqrt{2}\pi^3} \cdot \left| \sum_f N_C Q_f^2 g_{Aff} A_{1/2}^A(\tau_f) + \sum_{\tilde{\chi}_i^\pm} \frac{2M_W}{m_{\tilde{\chi}_i^\pm}} g_{A\tilde{\chi}_i^+ \tilde{\chi}_i^-} A_{1/2}^A(\tau_{\tilde{\chi}_i^\pm}) \right|^2 . \tag{31}$$

3. Decay $\Phi \Rightarrow \gamma + Z$ ($\Phi = H; h$)

According to the MSSM, the decay of CP-even H - and h -bosons into photon and vector Z -boson can occur through the fermion, $W^\pm$ - and $H^\pm$ - boson, scalar fermion and chargino loop diagrams. First, we consider the fermion loop diagrams shown in Figure1 a) and b) (the photon $\gamma(k_2)$ must be replaced by the vector boson $Z(k_2)$).

The matrix element of the decay $\Phi \Rightarrow \gamma + Z$ can be written as:

$$M(\Phi \Rightarrow \gamma Z) = A^Z e_\mu^*(k_1) U_\nu^*(k_2)[k_{2\mu} k_{1\nu} - (k_1 \cdot k_2) g_{\mu\nu}], \tag{32}$$

$U_\nu^*(k_2)$ is4-vector polarization Z - boson, A^Z determines the contribution to the amplitude fermion, $W^\pm$ - and $H^\pm$ - boson and other loop diagrams. To find the amplitude of the fermion loop diagrams, we write the matrix element corresponding to the diagram a) Figure 1:

$$M_a(\Phi \Rightarrow \gamma Z) = -ieQ_f N_C \cdot [\sqrt{2}G_F]^{1/2} m_f \cdot g_{\Phi ff} e_\mu^*(k_1) U_\nu^*(k_2) \cdot \frac{e}{2\sin\theta_W \cos\theta_W} \cdot V_{\mu\nu}, \tag{33}$$

where the tensor $V_{\mu\nu}$ is determined by the integral:

$$V_{\mu\nu} = \int \frac{d^4 k}{(2\pi)^4} \cdot \frac{Sp[\gamma_\mu(\hat{k} + \hat{k}_1 + m_f)(\hat{k} - \hat{k}_2 + m_f)\gamma_\nu(g_V(f) + \gamma_5 g_A(f))(\hat{k} + m_f)]}{(k^2 - m_f^2)[(k + k_1)^2 - m_f^2][(k - k_2)^2 - m_f^2]}, \tag{34}$$

$g_V(f)$ and $g_A(f)$ -vector and axial-vector coupling constants of a fermion with Z - boson:

$$g_V(f) = I_3(f) - 2Q_f x_W \quad , \quad g_A(f) = I_3(f); \tag{35}$$

$I_3(f) = \pm 1/2$ isthird projection of weak isospin fermion.

Define the trace of the product of Dirac matrices in the numerator of the integral (34):

$$Sp[\gamma_\mu(\hat{k} + \hat{k}_1 + m_f)(\hat{k} - \hat{k}_2 + m_f)\gamma_\nu(g_V(f) + \gamma_5 g_A(f))(\hat{k} + m_f)] =$$

$$= 4m_f g_V(f)T_{\mu\nu} + 4im_f g_A(f)\varepsilon_{\mu\nu\rho\sigma} k_{1\rho}(k_{2\sigma} - 2k_\sigma),$$

where the tensor $T_{\mu\nu}$ is given by (4).

Let's apply the Feynman integration technique

$$\frac{1}{ABC_0} = \int_0^1 dx \int_0^1 dy \int_0^1 dz \delta(x + y + z - 1) \cdot \frac{2}{(Ax + By + C_0 z)^3}$$

and calculate the integral (34), where we entered the notation

$$C_0 = k^2 - 2(k \cdot k_2) + M_Z^2 - m_f^2.$$

Then the integral (34) takes the form:

$$V_{\mu\nu} = \int \frac{d^4k}{(2\pi)^4} \cdot \int_0^1 dy \int_0^{1-y} dz \cdot \frac{8m_f [g_V(f)T_{\mu\nu} + ig_A(f)\varepsilon_{\mu\nu\rho\sigma}k_{1\rho}(k_{2\sigma} - 2k_\sigma)]}{[(k + k_1 y - k_2 z)^2 - a^2]^3}, \tag{36}$$

where $a^2 = m_f^2 - 2(k_1 \cdot k_2)yz - M_Z^2(z - z^2)$.

To calculate the integral (36), we replace the variable

$$k \Rightarrow (k - k_1 y + k_2 z).$$

Then (36) goes to the integral

$$V_{\mu\nu} = \int \frac{d^4k}{(2\pi)^4} \cdot \int_0^1 dy \int_0^{1-y} dz \cdot \frac{8m_f [g_V(f)T'_{\mu\nu} + ig_A(f)\varepsilon_{\mu\nu\rho\sigma}k_{1\rho}(k_{2\sigma} - 2(k - k_1 y + k_2 z)_\sigma)]}{(k^2 - a^2)^3}, \tag{37}$$

where

$$T'_{\mu\nu} = g_{\mu\nu}[m_f^2 - (k_1 \cdot k_2)] - (k - k_1 y + k_2 z)^2 g_{\mu\nu} + 4(k - k_1 y + k_2 z)_\mu (k - k_1 y + k_2 z)_\nu -$$

$$- 2(k - k_1 y + k_2 z)_\mu k_{2\nu} + 2k_{1\mu}(k - k_1 y + k_2 z)_\nu - k_{1\mu}k_{2\nu} + k_{2\mu}k_{1\nu}.$$

Note that the linear terms in k in the numerator of the integral disappear during integration (they are odd functions of k), besides this 4-momenta of the photon and the Z-boson satisfy the conditions of transverseness

$$e_\mu^*(k_1)k_{1\mu} = 0 \quad , \quad U_\nu^*(k_2)k_{2\nu} = 0.$$

As a result, the $T'_{\mu\nu}$ tensor is simplified:

$$T'_{\mu\nu} = 4k_\mu k_\nu - k^2 g_{\mu\nu} + k_{2\mu}k_{1\nu}(1 - 4yz) + g_{\mu\nu}[m_f^2 - (k_1 \cdot k_2)(1 - 2yz)].$$

A similar integral is obtained in the matrix element corresponding to the diagram b) in Figure 1, however, an expression proportional to the axial-vector coupling constant $g_A(f)$ changes its sign to the opposite. Therefore, the total contribution of both diagrams to the width of the decay $\Phi \Rightarrow \gamma + Z$ is proportional to the vector coupling constant of the fermion $g_V(f)$:

$$A_f^Z = \frac{ig_W \alpha_{KED} N_C Q_f}{\pi \cdot M_W \cos\theta_W} \cdot g_V(f) \cdot g_{\Phi ff} \cdot I(\tau_f, \lambda_f). \tag{38}$$

Here $g_W = 2M_W[\sqrt{2}G_F]^{1/2}$ iscommon electroweak coupling constant, $I(\tau_f, \lambda_f)$ isintegral, dependent on parameters $\tau_f = M_\Phi^2 / 4m_f^2$ and $\lambda_f = M_Z^2 / 4m_f^2$:

$$I(\tau_f, \lambda_f) = \int_0^1 dy \int_0^{1-y} dz \cdot \frac{1 - 4yz}{1 - 4(\tau_f - \lambda_f)yz - 4\lambda_f z(z - 1)}. \tag{39}$$

Thus, for the decay amplitude $\Phi \Rightarrow \gamma + Z$ we have the expression:

$$M(\Phi \Rightarrow \gamma Z) = -A_f^Z [(e^*(k_1) \cdot k_2)(U^*(k_2) \cdot k_1) - (k_1 \cdot k_2)(e^*(k_1) \cdot U^*(k_2))]. \tag{40}$$

Summing over the polarization states of the Z-boson

$$\sum_{pol} U_\mu^*(k_2) U_\nu(k_2) = -g_{\mu\nu} + \frac{k_{2\mu} k_{2\nu}}{M_Z^2} :$$

and squaring this amplitude

$$|M(H \Rightarrow \gamma Z)|^2 = |A_f^Z|^2 \left(-g_{\mu\nu} + \frac{k_{2\mu} k_{2\nu}}{M_Z^2} \right) \cdot [(e^*(k_1) \cdot k_2) k_{1\mu} - (k_1 \cdot k_2) e_\mu^*(k_1)] \times$$

$$\times [(e(k_1) \cdot k_2) k_{1\nu} - (k_1 \cdot k_2) e_\nu(k_1)] = |A_f^Z|^2 (k_1 \cdot k_2)^2 = \frac{1}{4} |A_f^Z|^2 M_H^4 \left(1 - \frac{M_Z^2}{M_\Phi^2} \right)^2. \tag{41}$$

It takes into account that, according to the laws of conservation of energy and momentum, $2(k_1 \cdot k_2) = (M_\Phi^2 - M_Z^2)$.

Based on the square of the matrix element (41), taking into account the amplitude (38), the following expression was obtained for the contribution of fermion loop diagrams to the decay width $\Phi \Rightarrow \gamma + Z$:

$$\Gamma(\Phi \Rightarrow \gamma Z) = \frac{G_F^2 \cdot M_Z^2 \cdot \alpha_{KED}}{16\pi^4} M_\Phi^3 \cdot \left(1 - \frac{M_Z^2}{M_\Phi^2} \right)^3 \left| \sum_f g_{\Phi f f} \cdot Q_f \cdot N_C \cdot g_V(f) A_f^\Phi(\tau_f, \lambda_f) \right|^2, \tag{42}$$

where $A_f^\Phi(\tau_f, \lambda_f)$ – loop formfactor:

$$A_f^\Phi(\tau_f, \lambda_f) = F_1(\tau_f, \lambda_f) - F_2(\tau_f, \lambda_f) ,$$

$$F_1(\tau_f, \lambda_f) = \frac{1}{2(\lambda_f - \tau_f)} + \frac{1}{2(\lambda_f - \tau_f)^2}[f(\tau_f) - f(\lambda_f)] - \frac{1}{(\lambda_f - \tau_f)^2}[g(\tau_f) - g(\lambda_f)], \tag{43}$$

$$F_2(\tau_f, \lambda_f) = -\frac{1}{2(\lambda_f - \tau_f)}[f(\tau_f) - f(\lambda_f)],$$

the function $f(\tau_f)$ is given by formula (17), and the function $g(\tau_f)$ is equal to:

$$g(\tau_f) = \begin{cases} \sqrt{\tau_f^{-1} - 1} \arcsin\sqrt{\tau_f} , & if \quad \tau_f \leq 1 , \\ \frac{1}{2}\sqrt{1 - \tau_f^{-1}} \left[\ln \frac{1 + \sqrt{1 - \tau_f^{-1}}}{1 - \sqrt{1 - \tau_f^{-1}}} - i\pi \right], & if \quad \tau_f > 1. \end{cases} \tag{44}$$

The width of the Higgs boson decay (42) shows that in the decay of $\Phi \Rightarrow \gamma + Z$ the photon is not circularly polarized. This is due to the preservation of CP parity in the decay of $\Phi \Rightarrow \gamma + Z$.

The decay of CP-even H - and h - bosons can also occur through $W^\pm$ - and $H^\pm$ - boson loop diagrams. In the unitary gauge, there are only three W - boson loop diagrams. For the contribution to the decay width of the $\Phi \Rightarrow \gamma Z$ $W^\pm$ -boson loop diagrams, the expression is obtained:

$$\Gamma(\Phi \Rightarrow \gamma Z) = \frac{G_F^2 \cdot M_W^2 \cdot \alpha_{KED} M_\Phi^3}{64\pi^4} \cdot g_{\Phi WW}^2 \cdot \left| A_W^\Phi(\tau_W, \lambda_W) \right|^2. \tag{45}$$

Here $A_W^\Phi(\tau, \lambda)$ – W - boson loop formfactor

$$A_W^{\Phi}(\tau,\lambda) = \cos\theta_W \{4(3 - tg^2\theta_W)F_2(\tau,\lambda) + [(1+2\tau)tg^2\theta_W - (5+2\tau)]F_1(\tau,\lambda)\}, \tag{46}$$

functions $F_1(\tau,\lambda)$ and $F_2(\tau,\lambda)$ defined above (formulas (43)).

Figure 5 shows the dependence of the $H \Rightarrow \gamma + Z$ decay width, caused by the contribution of $W^{\pm}$ - boson loop diagrams at $M_W = 80.385$, $x_W = 0.2315$, $tg\beta = 3$, on the Higgs boson mass M_H. As can be seen, with increasing mass M_H, the decay width $H \Rightarrow \gamma + Z$ decreases.

Figure 5. Dependence of the decay width $\Gamma(H \Rightarrow \gamma Z)$ on the mass M_H ($W^{\pm}$ - boson loop diagrams)
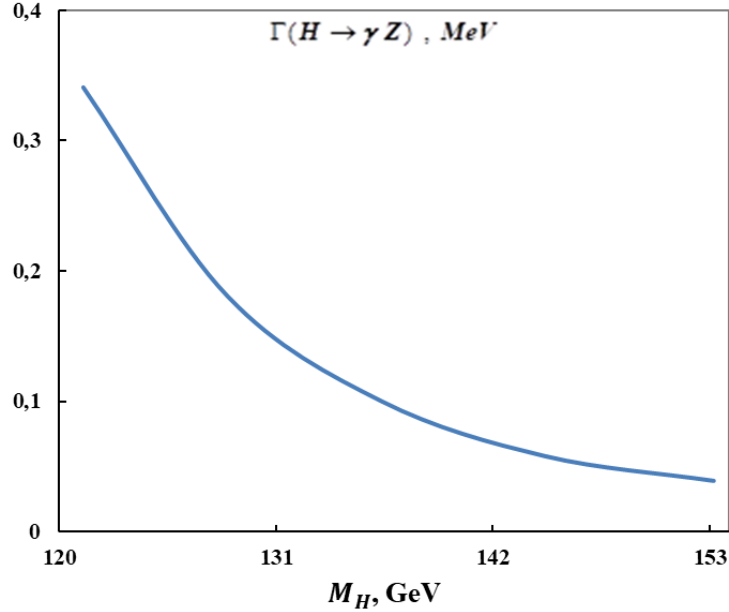
It should be noted that the $H(h) \Rightarrow \gamma + Z$ decay is also contributed by diagrams with charged $H^{\pm}$ Higgs-boson loops (Feynman diagrams are similar to diagrams f) and g) Figure1). For the width of the $\Phi \Rightarrow \gamma + Z$ decay, an expression is:

$$\Gamma(\Phi \Rightarrow \gamma Z) = \frac{G_F^2 \cdot M_Z^2 \cdot \alpha_{KED} M_{\Phi}^3}{256\pi^4} \cdot \left(1 - \frac{M_Z^2}{M_{\Phi}^2}\right)^3 \left(\frac{M_W^2}{M_{H^{\pm}}^2} \cdot g_{H^{\pm}} \cdot \lambda_{\Phi H^+ H^-}\right)^2 \left|A_0^{\Phi}(\tau_{H^{\pm}}, \lambda_{H^{\pm}})\right|^2, \tag{47}$$

where $g_{H^{\pm}} = \cos 2\theta_W / \cos\theta_W$ iscoupling constant Z - boson with $H^{\pm}$-Higgs boson, $A_0^{\Phi}(\tau,\lambda)$ is Higgs-boson loop form factor

$$A_0^{\Phi}(\tau,\lambda) = F_1(\tau,\lambda). \tag{48}$$

Figure 6 shows the dependence of the decay width $H \Rightarrow \gamma + Z$, due to $H^{\pm}$ - boson loop diagrams, on the Higgs boson mass M_H at $tg\beta = 3$ and $x_W = 0.2315$. The width of this decay is very small and decreases with increasing mass M_H.

Figure 6. Dependence of the decay width $\Gamma(H \Rightarrow \gamma Z)$ by mass M_H ($H^{\pm}$ - boson loop diagrams)

The scalar fermion loop diagrams contribute to the $\Phi \Rightarrow \gamma + Z$ decay, the amplitude of which is equal to:

$$A_{sfermion}^{\Phi} = \sum_{\tilde{f}_i} \frac{g_{\Phi\tilde{f}_i\tilde{f}_i}}{m_{\tilde{f}_i}^2} N_C Q_{\tilde{f}_i} g_V(\tilde{f}_i) \cdot A_0^{\Phi}(\tau_{\tilde{f}_i}, \lambda_{\tilde{f}_i}).$$ (49)

The decay width of the $\Phi \Rightarrow \gamma + Z$ with all loop diagrams, except for the chargino diagrams, is given by:

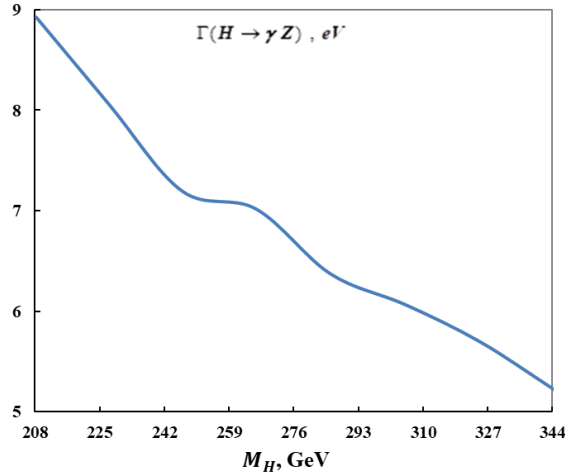$$\Gamma(\Phi \Rightarrow \gamma Z) = \frac{G_F^2 \cdot M_W^2 \cdot \alpha_{KED} M_{\Phi}^3}{64\pi^4} \cdot \left(1 - \frac{M_Z^2}{M_{\Phi}^2}\right)^3 \cdot \left| \sum_f g_{\Phi ff} \frac{Q_f g_V(f)}{\cos\theta_W} N_C A_{1/2}^{\Phi}(\tau_f, \lambda_f) + g_{\Phi WW} A_W^{\Phi}(\tau_W, \lambda_W) + \right.$$

$$\left. + \frac{M_W^2 g_{H^{\pm}}}{2\cos\theta_W M_{H^{\pm}}^2} \lambda_{\Phi H^+ H^-} A_0^{\Phi}(\tau_{H^{\pm}}, \lambda_{H^{\pm}}) + \sum_{\tilde{f}_i} \frac{g_{\Phi\tilde{f}_i\tilde{f}_i}}{m_{\tilde{f}_i}^2} N_C Q_{\tilde{f}_i} g_V(\tilde{f}_i) A_0^{\Phi}(\tau_{\tilde{f}_i}, \lambda_{\tilde{f}_i}) \right|^2.$$ (50)

4. Decay $A \Rightarrow \gamma + Z$

Now let us consider the decay of a CP-odd A-boson through the $A \Rightarrow \gamma + Z$ channel, the fermion loop diagrams of which are similar to the diagrams a) and b) of Figure1. Diagram a) corresponds to the amplitude

$$M_a(A \Rightarrow \gamma Z) = -ieQ_f N_C \cdot [\sqrt{2}G_F]^{1/2} m_f \cdot g_{Aff} e_{\mu}^*(k_1) U_{\nu}^*(k_2) \cdot \frac{e}{2\sin\theta_W \cos\theta_W} \times$$

$$\times \int \frac{d^4 k}{(2\pi)^4} \cdot \frac{Sp[\gamma_{\mu}(\hat{k} + \hat{k}_1 + m_f)\gamma_5(\hat{k} - \hat{k}_2 + m_f)\gamma_{\nu}(g_V(f) + \gamma_5 g_A(f))(\hat{k} + m_f)]}{(k^2 - m_f^2)[(k + k_1)^2 - m_f^2][(k - k_2)^2 - m_f^2]}.$$

For the trace of Dirac matrices, we get the expression:

$$Sp[\gamma_{\mu}(\hat{k} + \hat{k}_1 + m_f)\gamma_5(\hat{k} - \hat{k}_2 + m_f)\gamma_{\nu}(g_V(f) + \gamma_5 g_A(f))(\hat{k} + m_f)] =$$

$$= 4m_f g_V(f) i\varepsilon_{\mu\nu\rho\sigma} k_{1\rho} k_{2\sigma} + 4m_f g_A(f) X_{\mu\nu},$$

where

$$X_{\mu\nu} = g_{\mu\nu}[k^2 - m_f^2 - (k_1 \cdot k_2) - 2(k \cdot k_1)] - 2k_{\mu}k_{2\nu} - 2k_{\mu}k_{1\nu} - k_{1\mu}k_{2\nu} + k_{2\mu}k_{1\nu}.$$

A similar tensor is obtained in the matrix element corresponding to the diagram b), but an expression proportional to the axial-vector coupling constant $g_A(f)$ changes sign to the opposite. The total contribution of diagrams a) and b) to the decay width $A \Rightarrow \gamma + Z$ is proportional to the vector coupling constant $g_V(f)$:

$$M(A \Rightarrow \gamma Z) = -ieQ_f N_C \cdot [\sqrt{2}G_F]^{\frac{1}{2}} m_f \cdot g_{Aff} e_{\mu}^*(k_1) U_{\nu}^*(k_2) \times$$

$$\times \frac{e}{\sin\theta_W \cos\theta_W} \int \frac{d^4k}{(2\pi)^4} \cdot \int_0^1 dy \int_0^{1-y} dz \cdot \frac{8m_f g_V(f) i\varepsilon_{\mu\nu\rho\sigma} k_{1\rho} k_{2\sigma}}{[(k+k_1 y - k_2 z)^2 - a^2]^3} .$$

Replacing the integration variable $k \Rightarrow (k - k_1 y + k_2 z)$, simplify the matrix element

$$M_a(A \Rightarrow \gamma Z) = -ieQ_f N_C \cdot [\sqrt{2}G_F]^{\frac{1}{2}} m_f \cdot g_{Aff} e_{\mu}^*(k_1) U_{\nu}^*(k_2) \times$$

$$\times \frac{e}{\sin\theta_W \cos\theta_W} \int \frac{d^4k}{(2\pi)^4} \cdot \int_0^1 dy \int_0^{1-y} dz \cdot \frac{8m_f g_V(f) i\varepsilon_{\mu\nu\rho\sigma} k_{1\rho} k_{2\sigma}}{(k^2 - a^2)^3} .$$

This matrix element leads to decay width

$$\Gamma(A \Rightarrow \gamma Z) = \frac{G_F^2 \cdot M_Z^2 \cdot \alpha_{KED} M_A^3}{4\pi^4} \cdot \left(1 - \frac{M_Z^2}{M_A^2}\right)^3 \left| \sum_f g_{Aff} \cdot Q_f \cdot N_C \cdot g_V(f) A_f^A(\tau_f, \lambda_f) \right|^2, \tag{51}$$

where the $A_f^A(\tau_f, \lambda_f)$ fermion form factor is given by

$$A_f^A(\tau_f, \lambda_f) = F_2(\tau_f, \lambda_f). \tag{52}$$

In Fig. 7 illustrates the dependence of the decay width $H \Rightarrow \gamma + Z$ and $A \Rightarrow \gamma + Z$ on the mass of the Higgs bosons at the t-quark fermion loop with the parameters $tg\beta = 3$ and $x_W = 0.2315$. Chargino loop diagrams also contribute to the decay width $H \Rightarrow \gamma + Z$, but they are not considered by us.

Figure 7. Dependence of decay width $H \Rightarrow \gamma Z$ and $A \Rightarrow \gamma Z$ by Higgs boson mass (t - quark loop diagrams)
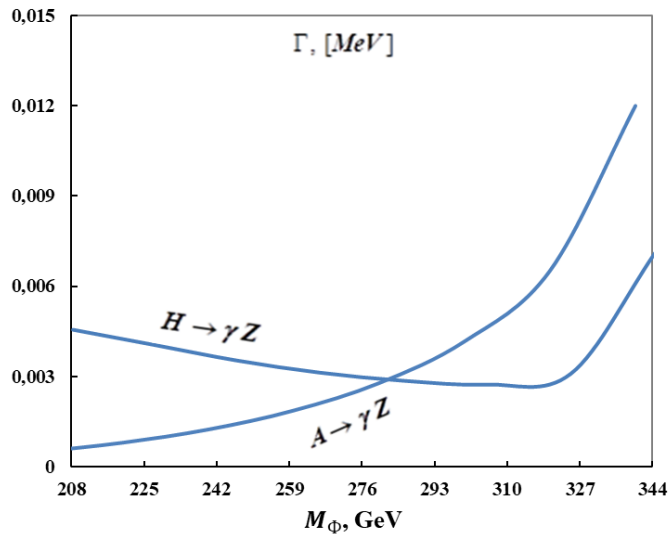
5. Decay $H^{\pm} \Rightarrow \gamma + W^{\pm}$

One of the decay channels of charged Higgs bosons is decay into a photon and gauge $W^{\pm}$ boson. In this case, the loop fermions are t - and b - quarks. Based on the t -quark and $\bar{b}$ -antiquark loop diagram, the expression for the decay width $H^{+} \Rightarrow t^{*} + \bar{b}^{*} \Rightarrow \gamma + W^{+}$ is obtained:

$$\Gamma(H^{\pm} \Rightarrow \gamma W^{\pm}) = \frac{\alpha_{KED}^{3} N_{C}^{2} M_{H^{+}}^{3}}{2^{8} \cdot 9\pi^{2} \cdot M_{W}^{2}} \cdot \left(1 - \frac{M_{W}^{2}}{M_{H^{+}}^{2}}\right)^{3} x_{W} \left[ctg^{2}\beta + \left(\frac{m_{b}}{m_{t}} tg\beta\right)^{2} \right]. \tag{53}$$

Figure 8 shows the dependence of the decay width $H^{+} \Rightarrow \gamma + W^{+}$ on the Higgs boson mass $M_{H^{+}}$ for $tg\beta = 3$, $x_{W} = 0.2315$ $M_{W} = 80,385$ ГэВ, $m_{t} = 173,2$ ГэВ , $m_{b} = 4,88$ ГэВ.

Figure 8. Dependence of the decay width $H^{+} \Rightarrow \gamma + W^{+}$ on the mass $M_{H^{+}}$
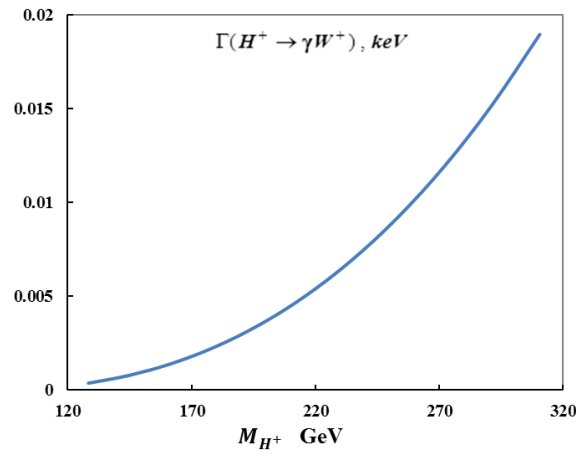
4. Conclusion

Thus, we discussed the MSSM Higgs boson decays into photons $H(h; A) \Rightarrow \gamma + \gamma$, into photon and the gauge boson: $H(h; A) \Rightarrow \gamma + Z$, $H^{\pm} \rightarrow \gamma + W^{\pm}$. Taking into account the fermion, $W^{\pm}$ - and $H^{\pm}$-boson, scalar fermion loop diagrams, analytical expressions for the widths of the indicated decays are obtained. The dependence of the decay width on the Higgs-boson mass is examined. Resultsareillustratedwithgraphs.

REFERENCES

1. Abdullayev S.Q. *Standart Model, lepton və kvarkların xassələri*, Bakı, "Zəka print" ,2017, 284 s.

2. Abdullayev S.Q.*Fundamental qarşılıqlı təsirlərin ümumi xassələri*, Bakı, "Zəka print" ,2018, 332s.

3. Djouadi A. *The Anatomy of Electro-Weak Symmetry Breaking. Tome I: The Higgs boson in the Standard Model*. arXiv: 050317v2, 2005.

4. Langacker P.*The Standard Model and Beyond*. CRS Press. 2010, 635 p.

5. Higgs P.W.*Broken symmetries, massless particles and gauge fields*, Phys. Letters, 1964. V.12., p.132-133.

6. Higgs P.W. *Broken symmetries and the mass of gauge bosons*, Phys. Rev. Lett., 1964. V.13., p.508-509.

7. ATLAS Collaboration. *Observation of a new particle in the search for the Standart Model Higgs boson with the ATLAS detector at the LHC*, Phys. Lett., 2012. B 716, p. 1-29.

8. CMS Collaboration. *Observation of a new boson at a mass of 125 GeV with the CMS experiment at the LHC.*, Phys. Lett., 2012. B 716, p. 30-61.

9. Yemelyanov V.M. Standartnaya model i yeyu rasşireniye, Moskva, Fizmatlit 2007, 584 p. (in Russian)

10. Djouadi A.*The Anatomy of Electro-Weak Symmetry Breaking. Tome II: The Higgs in Minimal Symetric Model*, arXiv: hep-ph /0503173v2, 2003.

11. Gunion J.F., Haber H.E. *Higgs bosons in supersymmetric models (I)* , Nucl. Phys. 1986, B272, p.1-76.

12. Gunion J.F., Haber. H.E. *Higgs bosons in supersymmetric models (II)* ,Nucl. Phys. 1986, B278, p.449-492.

13. Abdullayev S. K., OmarovaE.Sh. *Decays of Higgs bosons into fermion – antifermion pair.*, Russian Physics Journal, 2018, V.61, №9, p. 1603 – 1612.

14. Abdullayev S. K., Omarova E.Sh.*Raspadı Xiqqs bozonov na kalibrovoçnıy bozon i fermion-antiferm ionnuyu paru.* // İzvestiya Vuzov Fizika, 2019, T.62, №1, p. 28-35.

15. Abdullayev S. K., Omarova E.Sh.*Trexçastiçnıye raspadı xiqqs bozonov minimalnoy supersimmetriçnoy standartnoy modeli*, İzvestiya Vuzov Fizika, 2019, T.62, №3, p. 39-47.

16. Abdullayev S. K., Omarova E. Sh. *Decays of supersymmetric Higgs bosons into fermions.*, Azerb. Journal of Physics Fizika, 2018. Vol. XXIV , №4, p. 22-34.

17. Abdullayev S. K., Omarova E. Sh. *Two and three particle decay channels of supersymmetric Higgs bosons.*, Azerb. Journal of Physics Fizika, 2019. Vol. XXV,(çapdadır)

18. Abdullayev S. K., Omarova E. Sh. Raspadı *Xiqqs bozonov $H(h;A)$ na dva fotona (qlyuona)* , İzvestiya Vuzov Fizika, 2019, (çapdadır)

THE OBTAINING METHOD OF BINARY SOLUTION MONOCRYSTALS FROM PURE COMPONENTS BY SIMOULTINOUS APPLY OF TWO NUTRIENTS

[1]QAHRAMANOV N.F.,[1]QARAYEV E.S., [1]SADRADDINOV S.A., [2]HASHIMOVA A.I.

[1]Baku State University,[2]Sumgait State University,

Baku /AZERBAIJAN

eldarsq56@mail.ru

ABSTRACT

This thesis shows that two pure nutritients made from two seperate pure components are used to get monocrystalls of binary solid solutions .According to newly offered variants (cut, crush, scale, mix and fuse, etc.),the less number of manipulations provide the less contamination of obtained monocrystalls .The management of the compositon is realized by sorting out the cross-section dimesions of pure nutritents and their substitution rate .This method is applied onto *Ge-Si* solid solutions.

Although, there are no major problems with the preparation of the feeder, the application of the law of distribution along the crystal for the case of the molar percentage of Silicon within Germanium $C_0=10$ and *1 at.%*indica-tes that it is possible to obtain mono-crystals of fixed content of binary solids under both conditions.

Key words: monocrystal, nutrient, binary solution, component, distribution, alloy.

TƏMIZ KOMPONENTLƏRDƏN EYNI ZAMANDA IKI QIDALANDIRICI TƏTBIQ ETMƏKLƏ BINAR MƏHLULLARIN MONOKRISTALLARININ ALINMASI ÜSULU

XÜLASƏ

Hazırkı işdə putadan dartmaqla binar bərk məhlulların monokristallarını alarkən hər iki təmiz kompanentlərdən ayrı-ayrı düzəldilmiş iki təmiz qidalandırıcıdan istifadə edilmişdir. Təklif edilmiş yeni variant müəyyənmanipulyasiyaların (kəsmək, əzmək, tərəzidə çəkmək, bir yerə qarışdırıb əritmək və.s) sayı az olduğu üçün alınan monokristalların daha az çirklənməsini təmin edir. Tərkibin idarə olunması ayrı-ayrı təmiz kompanentlərinqidalandırıcılarının eninə ölçülərinin və yerdəyişmə sürətlərinin seçilməsi ilə həyata keçirilmişdir. Bu üsul *Ge–Si* bərk məhlullarına tətbiq edilmişdir. Silisiumun germaniumdakı molyar faizi$C_0=10$ və *1 at. %Si* olan hal üçün kristal boyunca paylanma qanununun tədqiqi göstərir ki, bu üsulla hər iki başlanğıc şərt daxilində binar bərk məhlulun sabit tərkibli monokristallarını almaq mümkündür.

Açar sözlər: monokristal, qidalandırıcı, binar məhlul, komponent, paylama, xəlitə.

МЕТОДПОЛУЧЕНИЕ МОНОКРИСТАЛЛОВ БИНАРНЫХ РАСТВОРОВ ИЗ ЧИСТЫХ КОМПОНЕНТОВ С ПРИМЕНЕНИЕМДВУХ ПОДПИТЫВАЮЩИХ СЛИТКОВ

АННОТАЦИЯ

В данной работе при пролучении бинарных твердых растворов вытягиванием из расплава, исползованы два подпитывающих слитка изготовленных из двух чистых компонентов. Предложенный новый вариант содержит минимум манипуляций (резка, измельчение, взвешивание, плавление и т.д.), поэтому обеспечиваем минимум загрязнения полученных монокристаллов. Управление составом обеспечивается толщиной подпитывающих слитков из различных чистых компонентов и выбором скорости вытягивания из расплава. Этот метод был применен к твердым раствором *Ge-Si*. Исследование закономерности распределения состава вдоль слитка для $C_0=10$ и 1ат. % *Si* в *Ge*, показывает, что при этих двух начальных условиях, возможно получить монокристаллы бинарных твердых растворов постоянным составом.

Ключевые слова: монокристалл, подпитка, бинарный раствор, компонент, распределение, сплав.

Binary solid solutions are widely used in the manufacture of multifunctional perceptible devices in modern solid state electronics. Therefore, the acquisition of identical monocrystals of solid solutions in the contemporary semiconductor physics technology is in the foreseeable future[1,2]. The segregation process that occurs during crystallization creates great difficulties in solving this problem. Various methods are used to eliminate these difficulties. One of them is feeding of the fusion while removing monocrystals by binding of binary solutions from the fusion. The optimal variant of the obtaining monocrystals of solid solutionsis givenin [3,4,5].One of the important issues is to prepare a nutritional alloy that is equivalent to the content of the monocrystal compound which requires the growth of its nutrients. Although there is not a major problem with the preparation of the nutritional alloy, it is necessary to expose the initial components (cut, crush, scale, mix and fuse, etc.) into certain manipulation . Probability of contamination of semiconductor substances with super ultra purity is increasing when they are exposed to any kind of operation. Therefore, the number of these operations should be minimized as far as possible.

In the present study, it has been proposed to feed the entire fusion not with alloy obtained from binary solution ,but with both pure nutrients simultaneously. For this purpose, the crystals of the components are cut off in proper quantities, or these crystals are grown in suitable devices. The dimensions of the nutrients must comply with the width and content of the crystal grown.

The crystal cultivation scheme is shown in fig.1. Here, 1 and 2 are the pure nutrients of the first and second components, 3 – is grown crystals, and 4 – is alloy in the pute. We will show the parameters representing them as well as indexes corresponding to their numbers. Let`s point the area of cross-section by S_1, S_2, S_3, thickness by $\rho_1, \rho_2, \rho_3, \rho_4$ displacement rates by v_1, v_2, v_3, the amount of nutrients melting in the fusion and their melted capacity by V_1, V_2, the capacity of the cristal by V_3, the capacity of fusion by V_4, the molar mass of the 1 and 2 components by μ_1 and μ_2.

Fig.1.The crystal cultivation scheme.
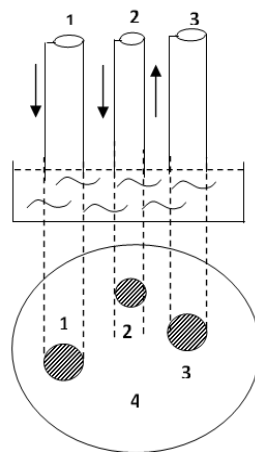
The process of cultivating the crystal is carried in the following way .Some quantities are placed on the germanium pute .After the high vacuum, it melts.After selecting the temprature regime, the crystal is grown, at the same time the feeding of the alloy with germanium (1) and silicon (2) begins. . The melting temperature of the silica (1417℃) is higher than the melting temperature of the germanium (937℃). However, it is well dissolved in germnium liquid. As soon as the nourishing liquid Si enters the liquid Ge liquid, it mixes in a short time an becomes identically mixed. In order to determine the identity of the solution in the pute and to ensure the

regularity of temperature domain in the the horizontal surfaces the pute and crystal revolves at an angle rate of (10-15 $\frac{cycle}{min}$).

To determine the principle of change of the composition throughout the crystal, the inconsistency equation for the second component of matter flux is used. To get the equation we should accept the following three conditions:

1) alloy in the pute is homogenous (this is ensured by the pute revolving and the high diffusion velocity in liquid;

2) transference of the liquid into solid substance does not occur (this is ensured by low diffusion velocity in solid substance);

3) fluid loss due to evaporation does not occur (this is ensured by low vapor pressure of both substances in the crystallization temperature).

Inconsistency equation appears under these conditions, the first component is melted in the alloy in one second and the amount of this substance dissolved in it is $-p_{1\delta}, v_1, S_1$, amount of S_1 molars is $\frac{p_{1\delta}v_1 S_1}{\mu_1}$, the same amount for the second component is properly $-p_{2\delta}, v_2, S_2$ and $\frac{p_{2\delta}v_2 S_2}{\mu_2}$. In a second the molar part of the second substance which is included into the fusion:

$$\frac{\frac{\rho_{1\delta}v_2 S_2}{\mu_2}}{\frac{\rho_{1\delta}v_1 S_1}{\mu_1} + \frac{\rho_{2\delta}v_2 S_2}{\mu_2}} = \frac{\mu_1\rho_{2\delta}v_2 S_2}{(\mu_2\rho_{1\delta}v_1 S_1 + \mu_1\rho_{2\delta}v_2 S_2)} = \frac{\mu_1\rho_{2\delta}v_2 S_2}{\mu_2\rho_{1\delta}v_1 S_1 + \mu_1\rho_{2\delta}v_2 S_2}.$$

The appropriate volume part of the second component $(s_1\upsilon_1 t + s_2\upsilon_2 t)$ including into the fusion in t second equals to $\frac{\mu_1\rho_{2\delta}\upsilon_2 S_2}{(\mu_2\rho_{1\delta}\upsilon_1 S_1 + \mu_1\rho_{2\delta}\upsilon_2 S_2)}(S_1\upsilon_1 + S_2\upsilon_2)\,t$ and the change of second component molar part in t interval is:

$$C_4(t)V_4(t) - C_4(0)V_4(0),$$

its part developed from alloy into cristal:

$$\int_0^1 V_3(t)C_3(t)dt.$$

So, balance equation is derived :

$$C_4(t)V_4(t) - C_4(0)V_4(0) = \frac{\mu_1\rho_{2\delta}v_2 S_2(S_1 v_1 + S_2 v_2)t}{\mu_2\rho_{1\delta}v_1 S_1 + \mu_1\rho_{2\delta}v_2 S_2} - \int_0^1 V_3(t)C_3(t)dt. \quad (1)$$

Certain substitutions are made :

$$\frac{\mu_1\rho_{2\delta}v_2 S_2(S_1 v_1 + S_2 v_2)}{\mu_2\rho_{1\delta}v_1 S_1 + \mu_1\rho_{2\delta}v_2 S_2} = a. \, (2)$$

Firts compostion derivative is obtained with respect to time on both sides in the formula (1):

$$\dot{C}_4(t)V_4(t) + \dot{V}_4(t)C_4(t) = a - V_3(t)C_3(t). \, (3)$$

$$k = \frac{C_3}{C_4}; \; C_3(t) = kC_4(t). \, (4)$$

Let's take (4) back into (3):

$$\dot{C}_4(t)V_4(t) + C_4(t)(\dot{V}_4(t) + k\dot{V}_3(t))C_4(t) = a$$

and all sides are divided into $V_4(t)$:

$$\dot{C}_4(t) + \frac{\dot{V}_4(t) + k\dot{V}_3(t)}{V_4(t)}C_4(t) = \frac{a}{V_4(t)} \quad (5)$$

$$\frac{\dot{V}_4(t) + k\dot{V}_3(t)}{V_4(t)} = P(t); \quad \frac{a}{V_4(t)} = Q(t). \quad (6)$$

(6) substiution is written in its right place in (5):

$$\dot{C}_4(t) + P(t)C_4(t) = Q(t). \quad (7)$$

The total form of this constant linar differential equation is [6]:

$$C_4(t) = exp\left(-\int P(t)dt\right)\left\{Q(t)exp\left[\int P(t)dt\right]dt + A\right\}. \quad (8)$$

A - is an integral constant. For determinig it, the initial conditions are used.First, let us look at it in a simple state . Let's consider that the nutritional alloy, as well as grown crystal are in thecylindrical state, where the cross-section area of the nutritents is equal to the cross-section area of the crystal$S_1 + S_2 = S_3$and their velocity are the same in this case $(v_1 = v_2 = v_3 = v)$,so in this case the volume of the alloy remains stable and the level of its surface does not change. In this case, the obtained volume is clearly the following:

$$V_1(t) = S_1vt; \quad V_2(t) = S_2vt; \quad V_3(t) = S_3vt; \quad V_4(t) = V_4(0) = const \quad (9)$$

$$\dot{V}_1 = S_1v; \quad \dot{V}_2 = S_2v; \quad \dot{V}_3 = S_3v; \quad \dot{V}_4 = 0. \quad (10)$$

Consider (10) and (6):

$$P = \frac{kS_3v}{V_4(0)}; \quad Q = \frac{a}{V_4(0)}. \quad (11)$$

Consider (11) and (8):

$$C_4(t) = exp\left(-\int \frac{kS_3v}{V_4(0)}dt\right)\left\{\frac{a}{V_4(0)}exp\left[\int \frac{kS_3v}{V_4(0)}dt\right]dt + A\right\} =$$

$$= \frac{a}{kS_3v} + A\,exp\left(-\frac{kS_3v}{V_4(0)}t\right). \quad (12)$$

Defining *A* for two different initial state:

1). If *t = 0*, then it equals to $C_4(0) = 0$. Here out of (12):

$$0 = \frac{a}{kS_3v} + A; \quad A = -\frac{a}{kS_3v}. \quad (13)$$

If we consider the value of *A* in (2):

$$C_4(t) = \frac{a}{kS_3v}\left[1 - exp\left(\frac{kS_3v}{V_4(0)}t\right)\right] =$$

$$= \frac{\mu_1\rho_{2\delta}S_2(S_1v_1 + S_2v_2)}{\mu_2\rho_{1\delta}S_1 + \mu_1\rho_{2\delta}v_2S_2}\left(1 - exp\left(\frac{kS_3v}{V_4(0)}t\right)\right). \quad (14)$$

Then, to obtain the distribution of the composition in crystal:

$$C_3(t) = kC_4(t) = \frac{\mu_1\rho_{2\delta}S_2(S_1v_1 + S_2v_2)}{kS_3v_3(\mu_2\rho_{1\delta}S_1 + \mu_1\rho_{2\delta}S_2)}\left[1 - exp\left(\frac{kS_3v}{V_4(0)}t\right)\right]. \quad (15)$$

2). In the second case we sholud choose the initial condition in order to make the consentration of the second component in alloy to be equal to its saturation rate. For that *t=0* equals to

$$C_4(0) = \frac{\mu_1 \rho_{2\delta} S_2 (S_1 v_1 + S_2 v_2)}{k S_3 v (\mu_2 \rho_{1\delta} S_1 + \mu_1 \rho_{2\delta} S_2)}.$$

So the equation is derived out of (12) is:

$$\frac{\mu_1 \rho_{2\delta} S_2 (S_1 v_1 + S_2 v_2)}{k S_3 v_3 (\mu_2 \rho_{1\delta} S_1 + \mu_1 \rho_{2\delta} S_2)} = \frac{\mu_1 \rho_{2\delta} S_2 (S_1 v_1 + S_2 v_2)}{k S_3 v_3 (\mu_2 \rho_{1\delta} S_1 + \mu_1 \rho_{2\delta} S_2)} + A \cdot$$

Where *A=0* and

$$C_4(0) = \frac{\mu_1 \rho_{2\delta} S_2 (S_1 v_1 + S_2 v_2)}{k S_3 v (\mu_2 \rho_{1\delta} S_1 + \mu_1 \rho_{2\delta} S_2)}. \quad (16)$$

The consentartion of the second component through the crystal remains stable

$$C_3 = k C_4 = \frac{\mu_1 \rho_{2\delta} S_2 (S_1 v_1 + S_2 v_2)}{S_3 v (\mu_2 \rho_{1\delta} S_1 + \mu_1 \rho_{2\delta} S_2)}, \quad (17)$$

$$C_0 = \frac{\mu_1 \rho_{2\delta} S_2}{\mu_2 \rho_{1\delta} S_1 + \mu_1 \rho_{2\delta} S_2}. \quad (18)$$

The molar percentage of silicium in germanium is $C_0 = 10$ and for the case of *1 at %* the obtained dependants through the crystal out of (15) and (17) for C_3 / C_0 are shown relatively in fig.2 with the help of 1 and 2 curves. As shown, it is possible to obtain stable compositon mono-crystalls of binary solutionsin both initial conditions by this method.

Fig.2. The distribution rule of the C_3/C_0 amount through the crystal
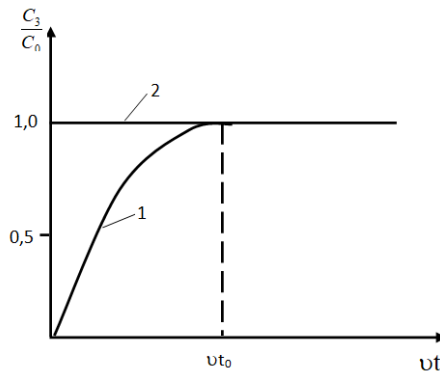
REFERENCES

1. Тагиров В.И., Тагиров У.В., Гахраманов Н.Ф. Физика полупроводников. Изд. СГУ, Баку-Сумгаит, 2006.

2. Тагиров В.И., Агамалиев З.А., Садыхова С.Р., Гулиев А.Ф., Гахраманов Н.Ф. // Об энергетических уровнях серебра в твердых растворах Ge-Si. // ФТП, 2012, т.46, в.3, с.304-307.

3. Tahirov V.İ., Həsənov Z.Y., Tahirov Ü.V., Qəhrəmanov N.F. Monokristal özəkdən istifadə etməklə binar bərk məhlul monokristallarının alınmasının sadə üsulu // AMEA-nın "Məruzələr", c.65, №3, 2009, s.590.

4. Tahirov V.İ. Yarımkeçiricilər fizikasının əsasları, Bakı-Sumqayıt, 2012, 445s.

5. Тагиров В.И. Полупроводниковые твердые растворы Ge-Si. Баку, «Элм», 1983, с.208.

6. Фихтенгольц Г.М. *Курс дифференциального и интегрального исчисления.-М.:* ФИЗМАТЛИТ, *т.2*, 810с.

ANISOTROPY OF THE NERNST-ETTINGSHAUSEN EFFECT IN QUASI-TWO-DIMENSIONALITY AND QUASI-THREE-DIMENSIONALITY ELECTRONIC SYSTEMS

HUSEYNAGHA HUSEYNOV

Azerbaijan University of Architecture and Construction

Baku/AZERBAIJAN

huseynov.h.i@mail.ru

ABSTRACT

The present work is devoted to the study of the anisotropy of the Nernst-Ettingshausen (NE) effect in superlattices depending on the direction of the magnetic field and the dimensionality of the electron gas. In this case is calculated the NE coefficient of quasi-two-dimensionality and quasi-three-dimensionality degenerate electron gas with cosine dispersion law in transverse and longitudinal magnetic field at scattering of charge carriers on acoustic, polar optical phonons and impurity ions.

It is found that in the perpendicular magnetic field at scattering by acoustic phonons for quasi-two-dimensionality electron gas the NE coefficient is zero, and the quasi-three-dimensionality one is negative, while at scattering by polar optical phonons the NE coefficient is positive. When scattering on weakly screened impurity ions with an increase in the magnetic field, the sign of the effect changes from negative to positive, and in weak magnetic fields with an increase in the dimensionality of the electron gas, the sign of the effect changes from positive to negative. In a parallel magnetic field for all types of scattering NE coefficient is nonzero and depending on the dimensionality of the electron gas and the magnetic field changes its sign. In strong magnetic fields, the NE coefficient at scattering by polar optical phonons in the same sample changes sign twice depending on the degree of miniband filling and the magnetic field. When scattering on phonons, the criteria of strong and weak magnetic field are influenced by the parameters of the superlattice.

Key words: superlattice, quasi-two-dimensional, quasi-three-dimensional, electron gas, NE effect.

АНИЗОТРОПИЯ ЭФФЕКТА НЕРНСТА-ЭТТИНГСГАУЗЕНА В КВАЗИДВУМЕРНЫХ И КВАЗИТРЕХМЕРНЫХ ЭЛЕКТРОННЫХ СИСТЕМАХ

РЕЗЮМЕ

Настоящая работа посвящена к исследованию анизотропии эффекта Нернста-Эттингсгаузена (НЭ) в сверхрешетках в зависимости от направления магнитного поля и размерности электронного газа. При этом вычислен коэффициент НЭ квазидвумерного и квазитрехмерного вырожденного электронного газа с косинусо-идальным законом дисперсии в перпендикулярном и параллельном магнитном поле относительно плоскости слоя при рассеянии носителей тока на акустических, полярных оптических фононах и ионах примеси.

Обнаружено, что в перпендикулярном магнитном поле при рассеянии на акустических фононах для квазидвумерного электронного газа коэффициент НЭ равна нулю, а квазитрехмерного меньше нуля, в то время при рассеянии на полярных оптических фононах коэффициент НЭ больше нуля. При рассеянии на слабо экранированных ионах примеси с ростом магнитного поля знак эффекта меняется с отрицательного на поло-жительный, в то время в слабых магнитных полях с увеличением размерности электронного газа знак эффекта меняется с положительного на отрицательный. В параллельном магнитном поле при всех видах рассеянии коэффициент НЭ отлично от нуля и в зависимости от размерности электронного газа и магнитного поля меняет свой знак. В сильных магнитных полях коэффициент НЭ при рассеянии на полярных оптических фононах в одном и том же образце дважды меняет знак в зависимости от степени заполнения зоны и магнит-ного поля. При рассеянии на фононах на критерии сильного и слабого магнитного поля влияют параметры сверхрешетки.

Ключевые слова: сверхрешетка, квазидвумерный, квазитрехмерный, электронный газ, эффект НЭ.

KVAZİ İKİ VƏ KVAZİ ÜÇ ÖLÇÜLÜ ELEKTRON SİSTEMLƏRİNDƏ NERNST-ETTINGSHA UZEN EFFEKTİNİN ANİZOTROPLUĞU

XÜLASƏ

İcmal ifratqəfəslərdə Nernst-Ettinqshauzen (NE) effektinin anizotropluğunun maqnit sahəsinin istiqamətindən və elektron qazının ölçüsündən asılılığının tədqiqinə həsr olunur. Bundan ötrü kosinusoidal dispersiya qanununa tabe olan kvaziikiölçülü və kvaziüçölçülü cırlaşmış elektron qazı üçün lay müstəvisinə perpendikulyar və paralel istiqamətdə yönəlmiş maqnit sahələrində akustik, polyar optik fononlardan, aşqar ionlarından səpilmə halında NE əmsalı hesablanmışdır.

Alınmışdır ki, NE əmsalı perpendikulyar maqnit sahəsində akustik fononlardan səpilmə üçün kvaziikiölçülü halda sıfıra bərabər, kvaziüçölçülü halda isə mənfidir, halbuki polyar optik fononlardan səpilmə halında müsbətdir. Zəif ekranlaşmış aşqar ionlarından səpilmə halında maqnit sahəsinin qiyməti artdıqca effektin işarəsi mənfidən müsbətə dəyişdiyi halda, zəif maqnit sahəsində elektron qazının ölçüsü artdıqca işarə müsbətdən mənfiyə dəyişir. Paralel maqnit sahəsində bütün səpilmə mexanizmləri halında NE əmsalı sıfırdan fərqlidir və elektron qazının ölçüsündən, maqnit sahəsindən asılı olaraq işarəsini dəyişir. NE əmsalı güclü maqnit sahəsində polyar optik fononlardan səpilmə halında mini-zonanın dolma dərəcəsindən, maqnit sahəsindən asılı olaraq eyni bir nümunədə işarəsini iki dəfə dəyişir. Fononlardan səpilmə halında güclü və zəif maqnit sahəsi kriteriyalarına ifratqəfəs parametrləri ciddi təsir edir.

Açar sözlər: Ifratqəfəs, kvaziikiölçülü, kvaziüçölçülü, elektron qazı, NE effekti.

INTRODUCTION

A characteristic feature of the physics of low-dimensionality electronic systems is, on the one hand, the presence of a number of new physical phenomena that do not occur in massive samples (quantum and spin Hall effects, extraordinary magnetoresistance, the phenomenon of weak electron localization, negative magnetoresistance, negative differential conductivity, oscillations of kinetic coefficients), on the other hand, the possibility of practical application of these new effects in the creation of micro - and nanoelectronic devices [1,2]. Therefore, the study of the properties of low-dimensionality electron gas is one of the current problems [3,4]. Among the kinetic phenomena thermomagnetic, especially the Nernst–Ettingshausen (NE) effect, is more sensitive to the scattering mechanisms, the structure of energy spectrum, the dimension of the electron gas, the temperature and the orientation of the magnetic field. The sign of the effect NE depends on the type of material, temperature and orientation of the magnetic field, in addition, it can vary in the same sample depending on the dimensionality of the electron gas. Determining the sign of the effect, it is possible to obtain valuable information about the mechanism of scattering, the dimensionality of the electron gas, as well as to use its characteristics for practical purposes [5-6].

Despite the fact that the effect NE has been discovered for a long time, in low-dimensionality electronic systems it has become intensively studied relatively recently. In low-dimensionality systems, the scattering mechanism and the energy spectrum are anisotropic, as a function of density of states is stepped view. Anisotropy of physical properties, as well as the direction of the magnetic field strongly affects the behavior of kinetic coefficients. Theoretical studies of the NE coefficient were carried out in [7-12], which considered a quasi–two-dimensionality electron gas with different dispersion laws, namely, linear and sinusoidal. In these works, it is shown that the NE coefficient oscillates proportionally to the magnetization derivative in terms of temperature and concentration of conduction electrons, and these oscillations in a weak magnetic field weaken, in addition, there is an increase and change of the sign of the NE coefficient. An increase in the field NE signal in graphene in the presence of a strong magnetic field was found experimentally in [13-16]. The possibility of sign NE change in strong magnetic fields in two-dimensionality systems is noted in [14]. In the case of a quasi-two-dimensionality electron gas in

a heterostructure in an intermediate magnetic field perpendicular to the layer plane, the NE effect is studied in [17], and in weak fields in [18-21]. The possibilities of changing the sign of the NE effect in classical fields in periodically modulated heterostructures [20] and in layered semiconductor structures [21-23] are analyzed. The dependences of the NE coefficient of a two-dimensionality electron gas on the direction of the magnetic field relative to the layer plane are devoted to [24-25]. In the above works, the NE effect was mainly studied in the perpendicular plane of the layer the magnetic field for the two-dimensional electron gas at low temperatures, did not sufficiently consider the impact of the scattering mechanism and the degree of miniband filling on the NE effect. In addition, in the parallel magnetic field to the layer plane, the NE effect is insufficiently studied. In the super–lattice, the nature of electron motion in the layer plane and perpendicular to it are very different. This movement in the presence of an electric and magnetic field is highly dependent on the topology of the Fermi surface and the direction of the magnetic field. In addition, the electron gas in superlattices can be both quasi-two-dimensionality and quasi-three-dimensionality depending on the Fermi surface topology.

This review is devoted to the NE effect in the scattering of charge carriers on different types of phonons and impurity ions in the perpendicular and parallel magnetic field to the layer plane in quasi-two-dimensionality and quasi-three-dimensionality electronic systems with cosine dispersion law. Using the quasi-classical approximation, the general expressions of the compo–nents of galvanic and thermomagnetic tensors and the coefficient NE for the degenerate electron gas in an arbitrary magnetic field are obtained. The analytical expressions of the coefficient NE in the limiting magnetic field cases and the dimensionality of the electronic system are determined. The features of the coefficient NE associated with the direction of the magnetic field are studied.

In the second part of the review, for the cosine dispersion law, expressions for anisotropic relaxation time at scattering of conduction electrons on phonons and impurity ions are given. In the third part of the review, general expressions of the components of galvanic and thermomagnetic tensors in the perpendicular and parallel magnetic field to the layer plane for the degenerate electron gas are obtained. In the fourth and fifth parts of the review, the dependences of the NE coefficient on the magnitude and direction of the magnetic field, as well as the degree of miniband filling at scattering on phonons and impurity ions, respectively, were investigated.

1. THE ENERGY SPECTRUM AND THE MECHANISM OF SCATTERING IN SUPERLATTICES (SL).

The peculiarity of superlattices is that electrons, in addition to the main periodic potential of the crystal lattice, are artificially created additional periodic potential with a period of an order of magnitude or more than the constant lattice. The period of the repeating layers in the superlattices ranges from 1nm up to tens of nanometers. In the superlattice, the width of the energy zone, the so-called mini zone or miniband, is less than the width of the energy zone of the material layers. Inside the layer, atoms are interconnected by strong chemical bonds - ionic or covalent, and between the layers a weak Van-der-Vaals bond acts. The energy spectrum of conduction electrons in layered structures and superlattices consists of the spectrum of free motion of electrons in the plane perpendicular to the axis of the superlattice - the approximation of a weak bond - $\hbar^2 k_\perp^2 / 2m_\perp$, and independently of it for the movement of electrons along the axis - the approximation of a strong bond of the spectrum - $\varepsilon_0 (1 - \cos ak_z)$. Thus, the energy spectrum of conduction electrons in superlattices takes the form:

$$\varepsilon = \hbar^2 k_\perp^2 / 2m_\perp + \varepsilon_0 (1 - \cos a k_z) . \tag{1.1}$$

Where $\hbar$ -Planck's constant, $k_\perp^2 = k_x^2 + k_y^2$, k_x and k_y the longitudinal components of the wave vector in the plane of the layer and k_z the transverse component of the wave vector along the SL axis, ε_0 — the half width of the conduction miniband, a - the SL constant, due to anisotropy $m_x = m_y = m_\perp$ -the components of the effective mass of the electron in the layer plane, and perpendicular to the layer plane, the effective mass depends on the components k_z of the wave vector and has the form:

$$m_z^{-1} = \frac{\varepsilon_0 a^2}{\hbar^2} \cos a k_z \tag{1.2}$$

The energy spectrum (1.1) in addition to SL is also applicable to layered semiconductor crystals, transition metal dichalcogenides, and periodically modulated heterostructures. In superlattices, not only the energy spectrum and structure, but also the mechanisms of scattering of conduction electrons are anisotropic. The main parameter characterizing the scattering mechanism is the inverse relaxation time tensor. When scattering by acoustic and polar optical phonons, the inverse relaxation time tensor is proportional to the density of the conduction electron state $g(\varepsilon)$ and can be written as [26]:

$$\frac{1}{\tau_\alpha} = A_r \frac{g(\varepsilon)}{(k_\alpha k_\perp)^r} \tag{1.3}$$

here $g(\varepsilon) = \frac{m_\perp Z(\varepsilon)}{\pi^2 \hbar^2 a}$, $Z(\varepsilon) = a k_z$, $Z(\varepsilon) = \pi$ when $\varepsilon > 2\varepsilon_0$ then $Z(\varepsilon) = \arccos(1 - \varepsilon/\varepsilon_0)$ and when $\varepsilon < 2\varepsilon_0$, $\alpha = (\perp, II)$, k_α - longitudinal and transverse components of the wave vector, A_r - constant for this scattering mechanism [27], at scattering by acoustic $r = 0$, and at scattering by polar optical phonons $r = 1$. It follows from formula (1.3) that the relaxation time for acoustic phonon scattering is isotropic and depends only on the density of states, while for polar optical phonon scattering the relaxation time is anisotropic and depends differently on the wave vector components.

At low temperatures, the main mechanism of scattering is scattering by impurity ions. Impurity atoms create discrete energy levels in forbidden zones near the valence band. Therefore, they are easily ionized at low temperatures. To obtain the final relaxation time, the radius of action of the Coulomb potential must be limited, i.e. the Coulomb potential must be screened. The screening radius r_0 of the Coulomb potential depends on the energy of conduction electrons and for a quasi-two-dimensional electron gas has the form [3, 27]:

$$r_0^{-2} = \left(\frac{4\pi e^2 n}{\chi \varepsilon_0} \right) \tag{1.4}$$ where $n = \frac{m_\perp \varepsilon_F}{\pi^2 \hbar^2 a}$ the concentration of charge carriers, ε_F - Fermi energy, χ -is the dielectric constant. In obtaining this formula, it is necessary to take into account the condition of the electroneutrality of the system $(n = N_i)$, i.e. the concentration of electrons is equal to the concentration of ions. With the change of the radius of the screening nature of the scattering changes. To obtain analytical expressions for the relaxation time it is necessary to consider the limiting cases: weak screening $k r_0 \gg 1$, strong screening $k r_0 \ll 1$ [28]. In case of

weak screening, the components of the inverse relaxation time tensor depend differently on the components of the wave vector and have the following form:

$$\frac{1}{\tau_\perp} = \frac{1}{\tau_0} \frac{\ln 4 k_z r_0}{(2 k_\perp r_0)^3},$$ (1.5)

$$\frac{1}{\tau_\parallel} = \frac{1}{\tau_0} \frac{1}{4 k_\perp k_z r_0^2}$$ (1.6)

here $\tau_0 = \frac{(m_\perp \chi)^{1/2}}{8 \pi N_i e a^{3/2}}$, where N_i -the impurity concentration, χ - is the dielectric constant.

The formulas (1.5) and (1.6) show that the transverse component of the inverse relaxation time depends strongly on the longitudinal component of the wave vector $k_\perp$ and logarithmically weakly on the transverse k_z and longitudinal component of the inverse relaxation time equally depends on the longitudinal and transverse components of the wave vector.

With strong screening, the scattering character varies greatly, the relaxation time becomes isotropic and is determined through the density of States. In this case, the charged impurity atom behaves as a point defect with a short-acting potential. This feature leads to the fact that the components of the inverse relaxation time tensor take the following form [28]:

$$\frac{1}{\tau_\parallel} = \frac{1}{\tau_\perp} = \frac{1}{\tau_0} 2 k_z r_0 = \frac{1}{\tau_0} \left(\frac{2 r_0}{a} \right) \cdot Z \ ($$ 1.7)

Formulas (1.5-1.7) are obtained in the born approximation $r_0 \ll r_B$ (where $r_B = \chi \hbar^2 / m e^2 -$ is effective Bohr radius). Now, knowing the relaxation time, we can proceed to finding the components of the galvanic and thermomagnetic tensor, through which the NE coefficient is expressed.

2. GALVANIC - AND THERMOMAGNETIC TENSOR

In multilayer solid-state structures with a controlled energy spectrum, which are called superlattices, depending on the degree of miniband filling, low–dimensionality electron gas is quasi-two-dimensionality or quasi-three-dimensionality. Therefore, the theory of kinetic phenomena in the magnetic field in anisotropic electron systems with cosine dispersion law should be developed in the direction that takes into account the dependence of the relaxation time on the components of the wave vector, as well as the dimensionality of the electronic system. In the semiclassical approximation, i.e. if the condition is met $\varepsilon_0 \gg \hbar / \tau$, it is possible to calculate the galvanic and thermomagnetic coefficients using the Boltzmann equation in the approximation of the relaxation time.

To determine the components of the galvanic and thermomagnetic tensor it is necessary to proceed from the generalized Ohm's law.

$$j_i = \sigma_{ik} E_k - \beta_{ik} \nabla_k T$$ (2.1)

where $i, k = x, y, z$.

To calculate the current density necessary to find the nonequilibrium distribution function from the Boltzmann equation in the relaxation time approximation for the anisotropic energy spectrum:

$$\vec{\upsilon}\vec{\Phi}_0 + \frac{e}{\hbar}\left[\vec{\upsilon}\vec{B}\right]\vec{\nabla}_k(\vec{\upsilon}\vec{P}) - \left(\vec{\upsilon}\left(\hat{\tau}^{-1}\vec{P}\right)\right) = 0 \tag{2.2}$$

where- $\vec{P}$ - the momentum of the generalized force, which includes all external forces (magnetic field $\vec{B}$, electric field $\vec{E}$, temperature gradient $\vec{\nabla}T$), $\vec{\upsilon}$ - the speed of conduction electrons,

- $\Phi_{0i} = -eE_i - (\varepsilon - \zeta)\nabla_i/T$ – the generalized disturbing force causing a deviation from the equilibrium distribution, ζ – is the chemical potential.

Solving the equation (2.2) in a random in magnitude and direction of the magnetic field, for the generalized force momentum we obtain:

$$\vec{P} = \frac{1}{1+v_0^2}\left\{\hat{\tau}\vec{\Phi}_0 + e\,\hat{\tau}\left[\vec{B}\hat{m}^{-1}\left(\hat{\tau}\vec{\Phi}_0\right)\right] + e^2\frac{|\hat{\tau}|}{|\hat{m}|}\left(\vec{B}\vec{\Phi}_0\right)\left(\hat{m}\vec{B}\right)\right\}, \tag{2.3}$$

where we have introduced the notation $v_0^2 = e^2\dfrac{|\hat{\tau}|}{|\hat{m}|}\left(\hat{m}B\right)\left(\hat{\tau}^{-1}B\right)$, $|\hat{m}| = m_\perp^2 m_{II}$ and $|\hat{\tau}| = \tau_\perp^2\tau_{II}$. Now,

substitute the nonequilibrium distribution function (2.3) in the current density expression, which is convenient for this law of dispersion (1.1) in cylindrical coordinates has the form [29]:

$$j_i = -\frac{em_\perp}{\pi^2\hbar^2 a}\int\limits_0^{Z_0}dZ\int\limits_0^{2\pi}d\varphi\int\limits_0^{\infty}\left(-\frac{\partial f_0}{\partial\varepsilon_\perp}\right)P_i v_i^2 d\varepsilon_\perp , \tag{2.4}$$

where Z_0 - is the degree of miniband filling and determines the dimensionality of the electron gas:

$$Z_0 = \begin{cases} \pi, & \zeta \succ 2\varepsilon_0, quasi-two-\dim ensional, opened\ Fermi\ surface \\ \arccos(1-\zeta/\varepsilon_0), & \zeta \prec 2\varepsilon_0, quasi-three-\dim ensional, closedFermisurfase \end{cases}$$

The open Fermi surface is represented as an open corrugated cylinder, and the closed surface is represented as an ellipsoid.

In layered structures, the nature of the motion of electrons in the plane of the layer and perpendicular to it are significantly different. Therefore, the dynamics of conduction electrons will strongly depend on the direction of the magnetic field and affect the behavior of the kinetic coefficients. Two geometries of the problem are considered here: 1) the temperature gradient $\vec{\nabla}T$ is directed along the axis x, the magnetic induction $\vec{B}$ along the axis z is perpendicular to the magnetic field (Fig.1a); 2) the temperature gradient is directed along the axis $\vec{\nabla}T$, the magnetic induction along the axis y - the longitudinal magnetic field (Fig.1b). However, for both geometries, the magnetic field is perpendicular to the temperature gradient.

Fig. 1. Geometry of the problem.

a.

b.
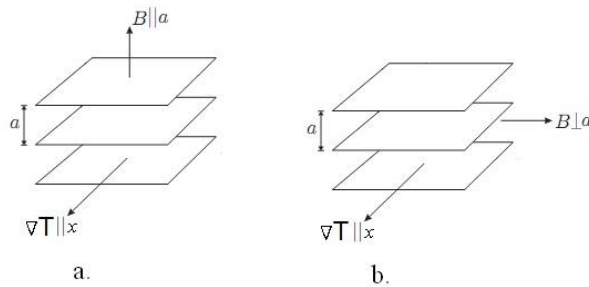
In the case of the first geometry of the problem based on the expression (2.3) and (2.4) for the components of the galvanic and thermomagnetic tensor we obtain [30,31]:

$$\sigma_{ik} = n_0 e^2 \left\langle \frac{\tau_\perp v_\perp^{i-k}}{1+v_\perp^2} \right\rangle, \quad \beta_{ik} = -\frac{n_0 e}{T} \left\langle \left(\varepsilon_\perp - \zeta_z\right) \frac{\tau_\perp v_\perp^{i-k}}{1+v_\perp^2} \right\rangle, \quad (2.5)$$

In the second geometry of the problem the components of galvanic and thermomagnetic tensors take the form [32, 33]:

$$\sigma_{xx} = e^2 n_0 < \frac{\tau_\perp}{1+v_\perp v_{//}} >, \sigma_{xz} = e^2 n_0 < \frac{\tau_\perp v_{//}}{1+v_\perp v_{//}} >, \sigma_{zz} = e^2 n_0 << \frac{\tau_{//}}{1+v_\perp v_{//}} >>,$$

$$\sigma_{zx} = e^2 n_0 << \frac{\tau_{//} v_\perp}{1+v_\perp v_{//}} >>, \quad (2.6)$$

$$\beta_{xx} = -\frac{en_0}{T} < \frac{\tau_\perp}{1+v_\perp v_{//}} (\varepsilon - \zeta) >, \beta_{xz} = -\frac{en_0}{T} < \frac{\tau_\perp v_{//}}{1+v_\perp v_{//}} (\varepsilon - \zeta) >,$$

$$\beta_{zz} = -\frac{en_0}{T} << \frac{\tau_{//}}{1+v_\perp v_{//}} (\varepsilon - \zeta) >> , \quad \beta_{zx} = -\frac{en_0}{T} << \frac{\tau_{//} v_\perp}{1+v_\perp v_{//}} (\varepsilon - \zeta) >>,$$

where averaging signs $\langle ... \rangle$ $\langle\langle ... \rangle\rangle$ have the following meaning, respectively:

$$\langle ... \rangle = \frac{1}{\pi^2 \hbar^2 n_0 a} \int\limits_0^\infty d\varepsilon_\perp \int\limits_0^{2\pi} d\varphi \int\limits_0^{Z_0} A\varepsilon_\perp dZ,$$

$$\langle\langle ... \rangle\rangle = \frac{\varepsilon_0}{\pi^2 \hbar^2 a n_0} \cdot \frac{m_\perp}{m_{//0}} \int\limits_0^\infty \int\limits_0^{Z_0} \left(-\frac{\partial f_0}{\partial \varepsilon_\perp}\right) A \cdot \left(\varepsilon_\perp, Z\right) \cdot \sin^2 Z \cdot d\varepsilon_\perp \cdot dZ,$$

$$v_\perp = eB\tau_\perp / m_\perp = \Omega\tau_\perp \left(m_{//0}/m_\perp\right)^{1/2}, v_{II} = eB\tau_{II}/m_{II} = \Omega\tau_{II} \left(m_\perp/m_{II0}\right)^{1/2},$$

$$v_\perp v_{II} = \Omega^2 \tau_\perp \tau_{II} \cos Z , \; v_\perp v_{II} = \Omega^2 \tau_\perp \tau_{II} \cos Z, \; \Omega = eB / \sqrt{m_\perp m_{II0}} .$$

We proceed to the calculation of the NE coefficient for the problem geometries considered in this review.

3. TRANSVERSE NE EFFECT IN THE SCATTERING ON PHONONS.

The transverse NE effect occurs for the same reason as the Hall effect, that is, as a result of the deflection of the flow of charged particles by the Lorentz force. The difference, however, is that in the Hall effect, the directed flow of particles occurs as a result of their drift in the electric field, and in the NE effect as a result of diffusion. A significant difference is the fact that unlike the constant Hall, the sign of the NE effect does not depend on the sign of the charge carriers. The sign of the transverse NE effect is determined by the nature of the dependence of the relaxation time on the components of the wave vector of charge carriers, i.e. on the nature of the scattering mechanism, which in superlattices is significantly different from the relaxation time in isotropic systems. It should be noted that with temperature the nature of scattering, i.e. the dominant mechanism, changes: at helium temperatures, the main one is scattering by impurity ions; at temperature, $40K$ - scattering by acoustic and $80K$ at optical phonons. Further, using the obtained expressions for galvanic and thermomagnetic tensors (2.5) and (2.6), it is necessary to consider separately the specific geometry of the problem and scattering by acoustic and polar optical phonons.

3.1 Transverse NE effect for scattering on acoustic phonons.

a) **The perpendicular magnetic field (** $B_\perp = B_z$ **).** With this geometry of the problem, the General formula for the NE coefficient $Q = -E_y/B\nabla_x T$ has the form:

$$Q = \frac{1}{B}\frac{\sigma_{xy}\beta_{xx} - \sigma_{xx}\beta_{xy}}{\sigma_{xx}^2 + \sigma_{xy}^2} \; . \tag{3.1}$$

Given the expressions for the components of a galvanic - and thermomagnetic tensors (2.5) in (3.1) get the general expression for the NE coefficient.

$$Q = \frac{1}{eT}\frac{\left\langle \frac{\tau_\perp v_\perp}{1+v_\perp^2}(\varepsilon-\zeta)\right\rangle\left\langle \frac{\tau_\perp}{1+v_\perp^2}\right\rangle - \left\langle \frac{\tau_\perp}{1+v_\perp^2}(\varepsilon-\zeta)\right\rangle\left\langle \frac{\tau_\perp}{1+v_\perp^2}\right\rangle}{\left\langle \frac{\tau_\perp}{1+v_\perp^2}\right\rangle^2 + \left\langle \frac{\tau_\perp v_\perp}{1+v_\perp^2}\right\rangle^2} \; . \tag{3.2}$$

In the case of a degenerate quasi-two-dimensionality electron gas when scattered by acoustic $(r=0)$ phonons, $\tau_\perp/m_\perp$ it is independent of energy, therefore $Q=0$ [34].

For a quasi-three-dimensionality electron gas in an arbitrary magnetic field, the coefficient NE, unlike the quasi-two-dimensional one, is nonzero $Q \neq 0$ and has the following form:

$$Q = \left(\frac{k_0}{e}\right)\frac{\pi^2}{3}\frac{k_0 T}{\varepsilon_0}u_{\perp 0}\frac{\int_0^{Z_0}\frac{dZ}{Z^2 Y_1}\int_0^{Z_0}\frac{XdZ}{ZY_1} - \int_0^{Z_0}\frac{dZ}{ZY_1}\int_0^{Z_0}\frac{XdZ}{Z^2 Y_1}}{\left[\int_0^{Z_0}\frac{XdZ}{ZY_1}\right]^2 + (\Omega_\perp\tau_0)^2\left[\int_0^{Z_0}\frac{XdZ}{Z^2 Y_1}\right]^2} \; , \tag{3.3}$$

here $X = \cos Z - \cos Z_0$, $Y_1 = 1 + (\Omega_\perp\tau_0)\frac{1}{Z^2}$, k_0 - Boltzmann constant, $u_\perp = e\tau_{01}/m_\perp$ - the mobility of the charge carriers in the plane of the layer.

From the expression (3.3) for the NE coefficient in a weak magnetic field $(\Omega_\perp\tau_0)<<1$ we obtain:

$$Q = \left(\frac{k_0}{e}\right)\frac{\pi^2}{3}\frac{k_0 T}{\varepsilon_0}u_{\perp 0}\frac{I_{-2,0,0}I_{-1,0,0} - I_{-1,0,0}I_{-2,0,1}}{I_{-1,0,1}^2} \; , \tag{3.4}$$

where $I_{klm} = \int_0^{Z_0}Z^k\cos^l Z(\cos Z - \cos Z_0)dZ$, here $\sigma_0 = e^2 n_0\tau_0/m_\perp$, $n_0 = m_\perp\varepsilon_0/\pi^2\hbar^2 a$ -concentration of quasi-two-dimensional electron gas, $v_0 = eB\tau_0/m_\perp = \Omega_\perp\tau_0$, $\Omega_\perp = eB/m_\perp$, $\tau_0 = A_0^{-1}(\pi^2\hbar^2 a/m_\perp)$. The calculations show that in this case the NE coefficient is directly proportional to the ratio $k_0 T/\varepsilon_0$ and mobility $u_{\perp 0}$, and the sign of the coefficient is negative: $Q<0$.

The following analytical result was obtained in a strong magnetic field $(\Omega_\perp\tau_0)>>1$:

$$Q = \left(\frac{k_0}{e}\right)\frac{\pi^2}{3}\frac{k_0 T}{\varepsilon_0}\frac{1}{B^2 u_{\perp 0}}\frac{(Z_0^2/2)\sin Z_0 + Z_0(\cos Z_0 - 1)}{(\sin Z_0 - Z_0\cos Z_0)^2} \; , \tag{3.5}$$

From (3.5) it can be seen that in a strong magnetic field, the NE coefficient is strongly dependent on Z_0, directly dependent on $k_0 T/\varepsilon_0$ and inversely proportional to the magnitude of the magnetic field, and the sign is negative $Q \prec 0$, as well as in a weak magnetic field.

$b)$**The parallel magnetic field ($B = B_{II}$).** In this case, the NE coefficient is expressed by the formula: $Q = - E_z / B \nabla_x T$, and it looks like [35]:

$$Q = - \frac{E_z}{B \nabla_x T} = \frac{1}{B} \frac{\sigma_{xx} \beta_{zx} - \sigma_{zx} \beta_{xx}}{\sigma_{xx} \sigma_{zz} + \sigma_{xz} \sigma_{zx}} \tag{3.6}$$

Substituting expressions for the galvanic and thermomagnetic components (2.6) in (3.6) for the NE coefficient we obtain:

$$Q = \frac{1}{B} \cdot \frac{1}{eT} \frac{\left\langle \frac{\tau_\perp}{1 + v_\perp v_{II}} \right\rangle \left\langle \left\langle \frac{\tau_{II} v_\perp}{1 + v_\perp v_{II}} (\varepsilon - \zeta) \right\rangle \right\rangle - \left\langle \frac{\tau_{II} v_\perp}{1 + v_\perp v_{II}} \right\rangle \cdot \left\langle \left\langle \frac{\tau_\perp}{1 + v_\perp v_{II}} (\varepsilon - \zeta) \right\rangle \right\rangle}{\left\langle \frac{\tau_\perp}{1 + v_\perp v_{II}} \right\rangle \cdot \left\langle \left\langle \frac{\tau_{II}}{1 + v_\perp v_{II}} \right\rangle \right\rangle + \left\langle \frac{\tau_\perp v_{II}}{1 + v_\perp v_{II}} \right\rangle \cdot \left\langle \left\langle \frac{\tau_{II} v_\perp}{1 + v_\perp v_{II}} \right\rangle \right\rangle} \tag{3.7}$$

The formula (3.7) is valid for an arbitrary degree of degeneration of the electron gas in a parallel magnetic field when scattered on acoustic and optical phonons, as well as on impurity ions.

When scattering by acoustic phonons $\beta_{zz} = \beta_{zx} = 0$ and the NE coefficient (3.7) will take the form:

$$\frac{Q}{Q_0} = - \frac{\frac{k_0 T}{\varepsilon_0} \frac{1}{Z_0} \int_0^{Z_0} \frac{dZ}{1 + \Omega^2 \tau_0^2 \cos Z}}{\int_0^{Z_0} \frac{\cos Z - \cos Z_0}{1 + \Omega^2 \tau_0^2 \cos Z} dZ + \Omega^2 \tau_0^2 \int_0^{Z_0} \frac{\cos Z (\cos Z - \cos Z_0) dZ}{1 + \Omega^2 \tau_0^2 \cos Z}} , \tag{3.8}$$

Here $Q_0 = \frac{k_0}{e} \frac{\pi^2}{3} \frac{e \tau_0}{m_\perp}$, $\tau_0 = \frac{\pi \hbar^3 \rho v_0^2 a}{E_1^2 k_0 T m_\perp Z_0}$, E_1 - is the constant of deformation potential, ρ - is the density of the crystal, v_0 - is the speed of sound in the crystal. From the expression (3.8) it can be seen that in the parallel magnetic field to the plane of layer $B = B_{II}$, the NE coefficient at scattering on acoustic phonons is nonzero and depends significantly on the degree of miniband filling Z_0 and the magnitude of the magnetic field B . On the basis of the formula (3.8) dependences Q/Q_0 on the degree of miniband filling are constructed (Fig.2) and the magnitude of the magnetic field (Fig.3)

Fig.2. The dependence of the dimensionless NE coefficient $Q(B_{II})/Q_0$ on the degree of miniband filling Z_0 :

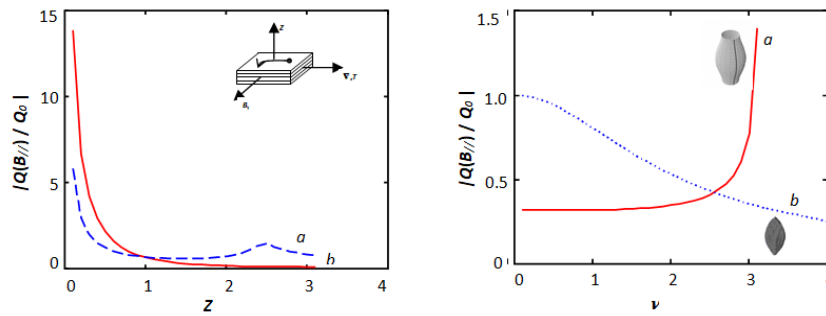a - -strong magnetic field($v = \Omega \tau_0 = 5$); b - weak magnetic field ($v = \Omega \tau_0 = 0.5$) .

Fig.3. Dependence of the dimensionless NE coefficient $Q(B_{II})/Q_0$ on the longitudinal magnetic field $v = \Omega \tau_0$: a - $Z_0 = \pi$; b - $Z_0 = \pi$

The figures show the Fermi surfaces for the quasi-two - dimensionality ($\varepsilon_F > 2\varepsilon_0$ - corrugated cylinder) and quasi-three-dimensionality ($\varepsilon_F < 2\varepsilon_0$ - ellipsoid) electron gas.

From Fig.2 it follows that in weak magnetic fields at small degrees of miniband filling, the NE coefficient takes a large value, and with a decrease in the dimensionality of the electron gas tends to zero. And in the field dependence of the NE coefficient there is a big difference: in the quasi-two-dimensionality case, the NE coefficient increases in the magnetic field, while for the quasi-three-dimensionality electron gas, on the contrary, decreases.

The analytical expression of the coefficient NE can be obtained only in the limiting magnetic field cases. In a weak magnetic field $\Omega\tau_0 << 1$ when scattered on acoustic phonons, the coefficient NE is determined by the formula:

$$Q = -\frac{k_0}{e}\frac{\pi^2}{3}\frac{e\tau_0}{m_\perp}\frac{Z_0}{\sin Z_0 - Z_0\cos Z_0}\left(1 - \Omega^2\tau_0^2\frac{\sin Z_0}{Z_0}\right). \tag{3.9}$$

It follows from (3.9) that the NE coefficient is negative at small degrees of miniband filling and modulo takes large values, and as the miniband is filled decreases, striving to constant value. In addition, the NE coefficient is directly proportional to the mobility of the current carriers in the plane of the layer. In a strong magnetic field of the NE coefficient has the form $\Omega\tau_0 >> 1$:

$$Q = -\frac{k_0}{e}\frac{\pi^2}{3}(\frac{e\tau_0}{m_{II0}})^{-1}\frac{k_0T}{\varepsilon_0}\frac{1}{B^2}\frac{\ln(tg(0.5Z_0 + 0.25\pi))}{\sin Z_0 - Z_0\cos Z_0}. \tag{3.10}$$

Unlike a weak magnetic field, the NE coefficient in a strong magnetic field is inversely proportional to the mobility of the electron gas in the direction perpendicular to the layer plane and the square of the magnetic field.

3.2 The transverse NE effect for scattering on polar optical phonons. When scattering by polar optical phonons, the relaxation time, in contrast to scattering by acoustic phonons, is strongly anisotropic, the transverse $\tau_\perp$ and longitudinal $\tau_{II} = \tau_z$ components of the relaxation time depend differently on the components of the wave vector $k_\perp, k_{II} = k_z$. The direction of the magnetic field strongly affects the dynamics of the conduction electrons and this affects the behavior of the NE coefficient. Consider the NE coefficient in the transverse $B = B_\perp = B_Z$ and longitudinal magnetic field $B = B_{II} = B_y$, separately.

a) **The perpendicular magnetic field ($B_\perp = B_z$).**

Substituting formulas (2.5) in (3.2), we obtain a general expression for the NE coefficient at scattering on polar optical phonons in a perpendicular magnetic field [36]:

$$\frac{Q}{Q_0} = \frac{\int_0^{Z_0}\frac{X^2dZ}{Y_{2\perp}}\left[\int_0^{Z_0}\frac{1}{2}\left(\frac{2X^2}{Y_{2\perp}^2} + \frac{X^2}{Y_{2\perp}}\right)\right] - \int_0^{Z_0}\frac{X^3dZ}{Y_{2\perp}}\int_0^{Z_0}\frac{XdZ}{Y_{2\perp}^2}}{\left(\frac{X^2dZ}{Y_{2\perp}}\right)^2 + v_0^2\left(\frac{\varepsilon_0}{k_0T}\right)^2\frac{1}{Z_0^2}\left(\int_0^{Z_0}\frac{X^2dZ}{Y_{2\perp}}\right)^2}, \tag{3.11}$$

where $Y_{2\perp}(Z) = 1 + v_{\perp 0}^2\frac{1}{Z_0^2}\left(\frac{\varepsilon_0}{k_0T}\right)^2 X^2(Z)$, $\tau_{\perp 0} = \frac{1}{A_1}\frac{\pi^2\hbar^2 a}{m_\perp}\left(\frac{2m_\perp k_0T}{\hbar^2}\right)$,

$$\tau_{II0} = \frac{1}{A_1} \frac{\pi^2 \hbar^2 a}{m_\perp} \left(\frac{2m_\perp k_0 T}{\hbar^2} \right)^{1/2} \frac{1}{a} \, , \; \nu_\perp = \nu_{\perp 0} \frac{1}{Z_0} \left(\frac{\varepsilon_\perp}{k_0 T} \right) , \; \nu_{\perp 0} = \frac{eB\tau_{\perp 0}}{m_\perp} \, .$$

To obtain an explicit dependence of the NE coefficient on the degree of miniband filling and the magnitude of the magnetic field, we consider separately the cases of a weak $\nu_\perp \ll 1$ and strong $\nu_\perp \gg 1$ magnetic field. In a weak magnetic field $\nu_\perp \ll 1$, the NE coefficient at scattering by polar optical phonons ($r = 1$) has the form:

$$Q = Q_0 \frac{2}{Z_0} \left(\frac{3}{2} - \frac{\sin Z_0 - Z_0 \cos Z_0}{(0.5Z_0 - 0.75 \sin 2Z_0 + Z_0 \cos Z_0)^2} I_{0,0,3} \right), \tag{3.12}$$

From the formula (3.12) we obtain that in the quasi-two-dimensionality case $Q = 2Q_0$, and in the quasi-three-dimensionality case $Q = 4Q_0/3$. In both cases, the NE coefficient is positive. In a strong magnetic field; the NE coefficient has the form,

$$Q = \frac{1}{B^2} Q_0 \frac{1}{u_\perp^2} \frac{Z_0}{\left(\sin Z_0 - Z_0 \cos Z_0 \right)^2} \, . \tag{3.13}$$

In the case of a quasi - two-dimensionality gas , the NE coefficient is determined by the formula $Q = Q_0 / (u_\perp B)^2 Z_0^2$, and in the case of a quasi-three-dimensionality gas– $Q = Q_0 / 3(u_\perp B)^2$.

Analyzing the dependence of the NE coefficient, one can notice a strong anisotropy in the scattering on polar optical phonons from the perpendicular magnetic field and from the degree of miniband filling (the concentration of charge carriers). The appearance of such anisotropy of the NE effect may be due to the presence of both open and closed cyclotron orbits in the magnetic field.

$b)$ **The parallel magnetic field ($B = B_{II}$).**

In this geometry of the problem for the NE coefficient of the degenerate electron gas in an arbitrary value of the parallel magnetic field and the degree of miniband filling at scattering by polar optical phonons, we obtain [35]

$$\frac{Q}{Q_0} = \frac{\frac{3}{2Z_0} \left(\int_0^{Z_0} \frac{X^2 dZ}{Y_{4II}} \int_0^{Z_0} \frac{X^{1/2} Z \sin^2 ZdZ}{Y_{4II}^2} \right) - \frac{1}{2Z_0} \int_0^{Z_0} \frac{X^{3/2} Z \sin^2 ZdZ}{Y_{4II}} \int_0^{Z_0} \frac{X(3 + Y(Z))dZ}{Y_{4II}^2}}{\int_0^{Z_0} \frac{X^2 dZ}{Y_{4II}} \int_0^{Z_0} \frac{X^{1/2} Z \sin^2 ZdZ}{Y_{4II}} + \Omega^2 \tau_{\perp 0} \tau_{II0} \left(\frac{\varepsilon_0}{k_0 T} \right)^{3/2} \int_0^{Z_0} \frac{X^{5/2} \cos ZdZ}{Y_{4II}} \int_0^{Z_0} \frac{X^{3/2} Z \sin^2 ZdZ}{Y_{4II}}}, \tag{3.14}$$

where $\tau_{\perp 0} = \dfrac{\hbar \chi a}{e^2 Z_0}; \tau_{II0} = \dfrac{\hbar \chi a}{e^2 Z_0} \sqrt{\dfrac{m_{II0}}{m_\perp}} \sqrt{\dfrac{\varepsilon_0}{k_0 T}} \, .$

On the basis of the expression (3.14) the dependence of the NE coefficient on the degree of miniband filling (Fig.4) and the magnitude of the magnetic field (Fig.5).

In layered semiconductors and superlattices with a small degree of miniband filling, the NE coefficient Q takes large positive values, then in the order $\pi/2$ region Z_0 becomes negative and for quasi–two-dimensionality electron gas ($Z_0 = \pi$) again becomes positive, i.e. changes sign twice (Fig.4). As it is known [27], in a three-dimensionality electron gas (massive semiconductor)

the sign of the effect can change in the same sample depending on the temperature. The sign of the NE coefficient in anisotropic systems is determined by the parameter $\gamma = \dfrac{m_{II}}{m_{\perp}} \dfrac{\tau_{\perp}}{\tau_{II}}$, i.e. dependence of relaxation time on energy and anisotropy of effective masses. And for a low-dimensionality electron gas, the sign changes can occur in the same sample not only depending on the temperature, but also on the degree of miniband filling and the direction of the magnetic field. This feature of low-dimensionality electron gas can be used in nanoelectronics.

Fig.4. The dependence of the dimensionless coefficient NE Q($B_{//}$)/Q_0 on the degree of miniband filling:

$$a - v_o = \Omega\sqrt{\tau_{0\perp}\tau_{0II}} = 4.5; \quad b - v_o = 1; \quad c - v = 0.5.$$
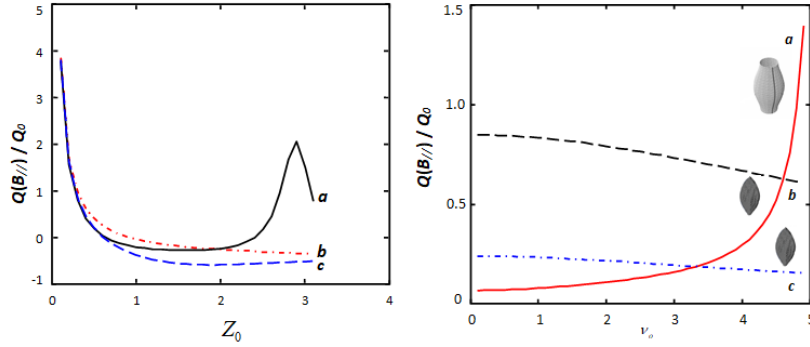
Fig.5. The dependence of the dimensionless coefficient NE Q($B_{//}$)/Q_0 on the degree of minibandfilling: $a - Z_0 = \pi$, $b - Z_0 = \dfrac{\pi}{3}$, $c - Z_0 = \dfrac{\pi}{2}$

The change in the NE coefficient in low-dimensional electronic gas is explained as follows. In layered semiconductors and superlattices, where the dimensionality of the electron gas can be both quasi-two-dimensionality and quasi-three-dimensionality, the effective masses of the conduction electrons along and perpendicular to the layer differ, $m_{\perp} < m_{II}$, moreover, it m_{II} depends on the wave vector $k_{II} = k_z$, as well as on the scattering of charge carriers on polar optical phonons, the relaxation time depends differently on the components of the wave vector $k_{\perp} u \ k_{II}$.

As a result, there are two different groups of electrons with different relaxation times and effective masses when moving along the plane of the layer and perpendicular to it. Parallel to the plane of the layer, the magnetic field acts differently on them and confuses these movements. For these groups of electrons, the ratio between the radius of the cyclotron orbit and the free path length is different and this plays a major role in changing the sign of the NE effect. A similar situation in the longitudinal magnetic field occurs for the Hall effect of a qua–si-two-dimensionality electron gas, where the sign change is associated with the existence of electrons with a negative effective mass m_{II} in the miniband region [29].

Analytical expressions for the coefficient Q can be obtained only in the cases of magnetic field limits.

The coefficient NE in a weak magnetic field $\Omega\tau \ll 1$ has the form:

$$Q = Q_0 \frac{1}{Z_0}\left[\frac{3}{2} + 2\frac{(\sin Z_0 - Z_0\cos Z_0)\cos Z_0}{0.5Z_0 - 0.75\sin 2Z_0 + Z_0\cos^2 Z_0}(1 + \frac{2}{3Z_0\sin Z_0}) \right] \tag{3.15}$$

The NE coefficient in a strong magnetic field $\Omega\tau \gg 1$ at scattering by polar optical phonons takes the following form:

$$Q = -Q_0 \frac{1}{2Z_0}\left(\frac{k_0 T}{\varepsilon_0}\right)^{3/2}\frac{1}{u_\perp u_{II0}B^2}\frac{I_{-1,-1,-1/2}}{\sin Z_0 - Z_0 \cos Z_0} \tag{3.16}$$

From the formulas (3.15) and (3.16) it follows that when the Fermi surface is closed in a weak magnetic field, it Q takes large positive values $Q = Q_0/Z_0 \cos Z_0$, and when approaching Z_0 to π (the open Fermi surface) - small negative values $Q = -Q_0/6$. A large value of the NE coefficient is associated with high mobility of current carriers in superlattices (for example, $GaAs/AlGaAs$ $u_\perp = 9.5\times10^5 cm^2/B\cdot c$, $u_{II} = 7.5\times10^3 cm^2/B\cdot c$ [37]) and depends on the position of the Fermi level (the degree of miniband filling) [18]. In a strong magnetic field from the formula (3.16) it follows that the scattering on polar optical phonons takes negative values and depending on the topology of the Fermi surface, the NE coefficient has a feature. Below is a comparison of the dependence of the NE coefficient on the magnetic field in the scattering of conduction electrons on acoustic and polar optical phonons for quasi-three-dimensionality (Fig.6) and quasi-two-dimensionality electron gas (Fig.7), respectively.

It follows from figures (6) and (7) that in weak magnetic fields the signs of the NE effect of a quasi-three-dimensionality electron gas in the scattering of charge carriers on acoustic and polar optical phonons differ from each other, while in the quasi-two-dimensionality case in a strong magnetic field the signs coincide. When scattering by polar optical phonons, the sign Q changes at the order of v_o 4.5, which for the above mobility of superlattices $GaAs/AlGaAs$ with $a = 5nm$ corresponds to the value of the magnetic field $B \approx 0.5Tl$ (under the condition $\hbar\omega < k_0 T$). In experimental work [23] it is shown that in layered crystals the sign change in concentration dependence Q is observed .

To study the concentration dependence of the NE coefficient in strong and weak magnetic fields separately based on the formula (3.9),(3.10),(3.15),(3.16) the dependence of the NE coefficient on the degree of miniband filling Z_0 (Fig.8), (Fig.9). It can be seen from figures 8 and 9 that the NE coefficients in a weak magnetic field for small concentration values at scattering by optical and acoustic phonons are very different, and at large values they approaching to zero [38]. In strong magnetic fields at low concentrations of charge carriers, the NE coefficient becomes negative when scattered on polar optical phonons, as well as when scattered on acoustic phonons.

Fig. 6. Dependence of the dimensionless NE coefficient $Q(B_{//})/Q_0$ on the magnetic field for quasi-three-dimensionality electron gas: a - scattering by polar optical phonons, b − scattering by acoustic phonons.
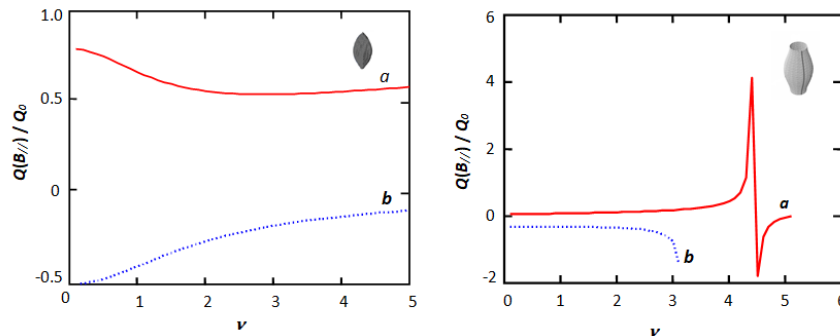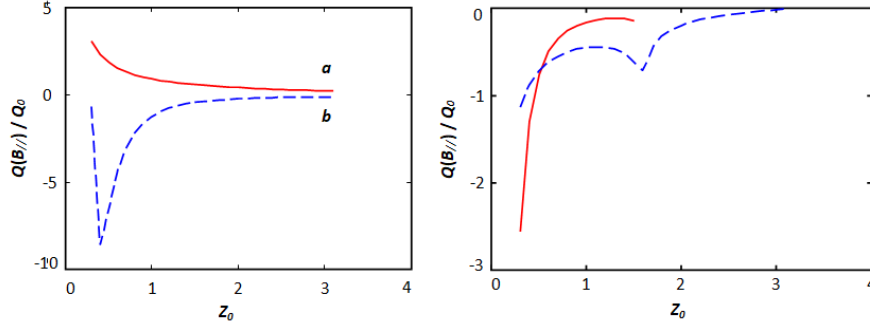
Fig. 7. The dependence of the dimensionless NE coefficient $Q(B_{//})/Q_0$ on the magnetic field for quasi-two-dimensionality electron gas: a - scattering by polar optical phonons; b – scattering by acoustic phonons.

Fig. 8. The dependence of the dimensionless NE coefficient $Q(B_{//})/Q_0$ on the degree of miniband filling in a weak magnetic field: a – scattering by optical phonons, b - scattering by acoustic phonons.

Thus, the sign of the effect can change in one of the samples depending on the concentration of the charge carriers and the magnetic field. At large values of the degree of miniband filling Z_0, the NE coefficient tends to zero, in agreement with experimental work [27]

Fig. 9. Dependence of the dimensionless NE coefficient $Q(B_{//})/Q_0$ on the degree of miniband filling in a strong magnetic field: a – scattering by optical phonons, b - scattering by acoustic phonons.

Analyzing the criteria of strong and weak magnetic field, it can be seen that these criteria are influenced by the parameters of the superlattice a and ε_0.

4. THE TRANSVERSE NE EFFECT FOR SCATTERING ON IMPURITY IONS.

In impurity semiconductors in the study of kinetic effects, taking into account the long-range Coulomb potential of the ion leads to the inverse value of the relaxation time to logarithmic divergence, mobility takes on an infinitely large value and loses physical meaning. It is obvious that to obtain the final value τ^{-1} and mobility it is necessary to limit the radius of action of the Coulomb potential of the ion [27]. Here we can consider two limiting cases: weak $kr_0 \succ\succ 1 u$ and $kr_0 \prec\prec 1$ strong screening. Consider the NE effect for scattering of charge carriers by weakly screened impurity ions. In [28] the relaxation times are calculated and it is shown that in this case the components of the inverse relaxation time tensor depend differently on the components of the momentum of conduction electrons. Below we will look at two geometries of the problem.

a) **The perpendicular magnetic field ($B_\perp = B_z$).** Given the geometry of the problem for the NE coefficient of the degenerate electron gas in an arbitrary perpendicular magnetic field, we have [39]:

$$Q = \frac{\pi^2}{3}\frac{k_0}{e}\frac{k_0 T}{\varepsilon_0}u_{\perp 0}\left\{\frac{\int_0^{Z_0}\frac{X^3(3+Y_{3\perp})dZ}{(\ln t)^2 Y_{3\perp}^2}\int_0^{Z_0}\frac{X^{5/2}dZ}{(\ln t)Y_{3\perp}} - \left[\int_0^{Z_0}\frac{X^{3/2}dZ}{(\ln t)Y_{3\perp}} + \frac{3}{2}\int_0^{Z_0}\frac{X^{3/2}(2-Y_{3\perp})}{(\ln t)Y_{3\perp}^2}\right]\int_0^{Z_0}\frac{X^4 dZ}{(\ln t)^2 Y_{3\perp}}}{\left[\int_0^{Z_0}\frac{X^{5/2}}{(\ln t)Y_{3\perp}}\right]^2 + (\Omega_\perp \tau_{01})^2\left[\frac{X^4 dZ}{(\ln t)^2 Y_{3\perp}}\right]^2}\right\}, \tag{4.1}$$

where $Y_{3\perp}(Z) = 1 + v_0^2 X^3(Z)(\ln t)^{-2}$, $\sigma_0 = e^2 n_0 \tau_{\perp 0} / m_\perp$, $t = 2Z_0 r_0 / a$.

In the weak magnetic field $v_\perp \ll 1$ of (4.1) for the coefficient we have:

$$Q = \frac{\pi^2}{3}\left(\frac{k_0}{e}\right)\frac{k_0 T}{\varepsilon_0}\frac{e\tau_{0\perp}}{m_\perp}\frac{1}{\ln(2Z_0 r_0/a)}\frac{1}{I_{0,0,5/2}}\left(4I_{0,0,3} - \frac{5}{2}\frac{I_{0,0,3/2}}{I_{0,0,5/2}}I_{0,0,4}\right) \tag{4.2}$$

It follows from (4.2) that in a weak magnetic field the NE coefficient does not depend on the magnetic field and is expressed through integrals $I_{k,l,m}$ which are analytically calculated only in special cases by the dimension of the electron gas:

For quasi-two-dimensionality electron gas

$$Q = -4\pi^2\left(\frac{k_0}{e}\right)\frac{k_0 T}{\varepsilon_0}\frac{e\tau_{\perp 0}}{m_\perp}. \tag{4.3}$$

It follows from the formula (4.3) that for a quasi-two-dimensionality electron gas in a weak magnetic field, the coefficient NE is negative and does not depend on the screening parameter of the Coulomb potential.

For quasi-three-dimensionality electron gas

$$Q = \frac{\pi^2}{3}\left(\frac{k_0}{e}\right)\frac{k_0 T}{\varepsilon_0}\frac{e\tau_{\perp 0}}{m_\perp}\frac{1}{\sin 0.5Z_0}\{4\left[-Z_0\left(\cos^2 Z_0 + 1.5\right) + 0.5\left(5 - 3.7\sin^2 Z_0\right)\sin Z_0\right] -$$

$$\frac{2.5(\sin Z_0 - Z_0\cos Z_0)}{Z_0\left(0.5 + \cos^2 Z_0\right) - 0.75\sin 2Z_0}\left[Z_0\left(0.4 + 3\cos^2 Z_0 + \cos^4 Z_0\right) - 2.2\left(1 - 0.5\sin^2 Z_0\right)\sin 2Z_0\right]\}$$

$$\tag{4.4}$$

For a quasi–three-dimensionality electron gas in a weak magnetic field, the NE coefficient (4.4) strongly depends on the degree of miniband filling and is directly proportional to the mobility of the conduction electrons, while the NE coefficient can take both positive and negative values. When scattering on weakly screened impurity ions, the change in the sign of the NE coefficient seems to be due to the existence of a region with a negative effective mass in the miniband.

In a strong magnetic field $v_\perp = \omega\tau_\perp \gg 1$ for the NE coefficient we obtain:

$$Q = \frac{1}{B^2}\frac{\pi^2}{3}\left(\frac{k_0}{e}\right)\frac{k_0 T}{\varepsilon_0}\frac{\ln(2Z_0 r_0/a)}{e\tau_{\perp 0}/m_\perp}\left[\frac{1}{2}\frac{I_{0,0,-3/2}}{I_{0,0,1}} + \frac{I_{0,0,-1/2}I_{0,0,0}}{I_{0,0,1}^2}\right] \tag{4.5}$$

It follows from the formula (4.5) that in a strong magnetic field the coefficient NE is positive, nonmonotonically depends on the degree of band filling Z_0 and logarithmically on the ratio between the screening radius of the Coulomb potential of the ions of the mixture and the superlattice constant.

$b)$ **The parallel magnetic field ($B = B_{II}$).**

Since the dynamics of the electron in the layer plane and perpendicular to it is very different, the most interesting results for the study of the NE effect should be expected for the second geometry of the problem, when the magnetic field is directed along the layer plane.

For the NE coefficient of the degenerate electron gas we obtain [40, 41]:

$$\frac{Q}{Q_0}=\left(\frac{\varepsilon_0}{k_0T}\right)^{1/2}\frac{2\int_0^{Z_0}\frac{X^{5/2}dZ}{Y_{3II}\ln t}\cdot\int_0^{Z_0}\frac{ZX\sin^2ZdZ}{Y_{3II}\ln t}-\frac{1}{2}\int_0^{Z_0}\frac{ZX^2\sin^2ZdZ}{Y_{3II}\ln t}\cdot\int_0^{Z_0}\frac{X^{3/2}[4+Y_{3II}]dZ}{Y_{3II}\ln t}}{\int_0^{Z_0}\frac{X^{5/2}dZ}{Y_{3II}\ln t}\cdot\int_0^{Z_0}\frac{ZX^{1/2}\sin^2ZdZ}{Y_{3II}}+\Omega^2\tau_\perp\tau_{II0}\left(\frac{\varepsilon_0}{k_0T}\right)^2\int_0^{Z_0}\frac{ZX^3\cos ZdZ}{Y_{3II}\ln t}\int_0^{Z_0}\frac{ZX^2\sin^2ZdZ}{Y_{3II}\ln t}} \tag{4.6}$$

On the basis of the formula (4.6) we plot the dependence of the NE coefficient on the magnetic field at different degrees of miniband filling ($Z=\pi/2$, -quasi–two-dimensionality electron gas, Fig.10) and ($Z=\pi/2$, quasi-three-dimensionality electron gas, Fig.11).

The figures show that for a degenerate quasi-two-dimensionality electron gas, the NE coefficient is negative, monotonically depends on the magnetic field and tends to zero with increasing field. And when the electron gas changes its dimensionality, becoming quasi-three-dimensionality, the NE coefficient is positive and with the increase of the magnetic field tends to zero from the positive values.

Fig. 10. Dependence of the NE coefficient Q/Q_0 on the magnetic field for
quasi-two-dimensionality electron gas $Z_0=\pi$.
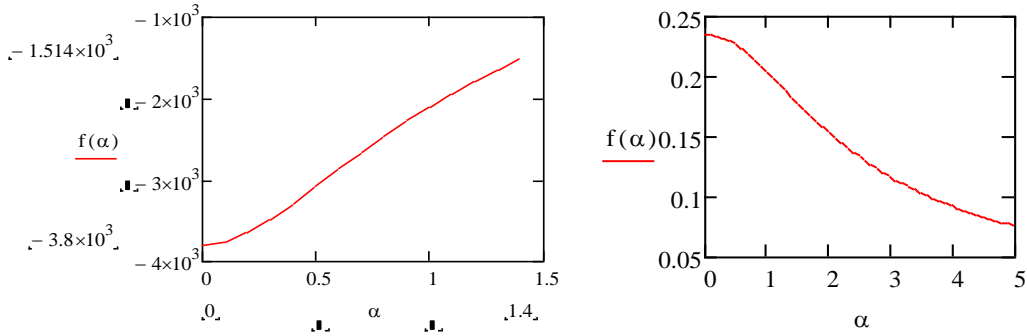
Fig.11. Dependence of the NE coefficient Q/Q_0 on the magnetic field:

for quasi-three-dimensionality electron gas $Z_0=\pi/2$.

The peculiarities in the behavior of the NE coefficient seem to be related to the change in the free path length in a strong magnetic field, to the ratio between the superlattice constant and the radius of the cyclotron orbit, and also to the fact that in the quasi – two-dimensionality case the screening radius does not depend on the concentration. The inversion of the sign of the NE coefficient is due to the geometric effect of electronic orbits in relatively strong magnetic fields.

In a weak magnetic field, decomposing expression (4.6) by parameter $\Omega\tau<<1$, is obtained for the coefficient in the following dependence on the degree of miniband filling Z_0 and the ratio between the screening radius and the constant over the lattice a.

$$\frac{Q}{Q_0}=\left(\frac{\varepsilon_0}{k_0T}\right)^{1/2}\frac{1}{\ln\left(2r_0Z_0/a\right)}\left[2\frac{I_{1,0,1}-I_{1,2,1}}{I_{1,0,1/2}-I_{1,2,1/2}}-\frac{5}{2}\cdot\frac{I_{0,0,3/2}}{I_{0,0,5/2}}\frac{I_{1,0,2}-I_{1,2,2}}{I_{1,0,1/2}-I_{1,2,1/2}}\right] \tag{4.7}$$

$$\frac{Q}{Q_0}=\left(\frac{\varepsilon_0}{k_0T}\right)^{1/2}\frac{1}{\ln t}\cdot\frac{8}{[(1-\cos Z_0)/2]^{1/2}\left(Z_0^2-Z_0\sin 2Z_0+\sin^2Z_0\right)}\left[\varphi_1(Z_0)-1,25\frac{\sin Z_0-Z_0\cos Z_0}{Z_0\left(0.5+\cos^2Z_0\right)}\varphi_2(Z_0)\right] \tag{4.8}$$

$$\varphi_1(Z_0)=\left(\frac{2}{9}-\frac{Z_0^2}{4}\right)\cos Z_0+\frac{1}{3}Z_0\left(\frac{7}{2}\cos Z_0+1\right)\sin Z_0-\frac{5}{36}\sin^2Z_0\cos Z_0-\frac{2}{9}$$

$$\varphi_2(Z_0) = \frac{Z_0^2}{4}\left(\frac{1}{4} + \cos^2 Z_0\right) + \frac{1}{16}Z_0\left(1 - 6\cos^2 Z_0\right)\sin 2Z_0 + \left(\frac{5}{16} + \frac{2}{9}\right)\frac{1}{4}\sin^2 2Z_0 - \frac{1}{3}\sin^2 Z_0 \sin 2Z_0$$

From the formula (4.7) and (4.8) it can be seen that the NE coefficient Q/Q_0 in weak magnetic fields depends logarithmically weakly on r_0/a, non-monotonically on Z_0, and also depends on the ratio between the half-width of the miniband ε_0 and $k_0 T$ does not depend on the magnitude of the magnetic field B. Now consider the limiting case in the dimensionality of the electron gas. For a quasi-two-dimensionality electron gas, the NE coefficient is

$$\frac{Q}{Q_0} = \left(\frac{\varepsilon_0}{k_0 T}\right)^{1/2}\frac{1}{\ln(2r_0 Z_0/a)}(-0,432) < 0 \tag{4.9}$$

It can be seen that the NE coefficient Q/Q_0 for the quasi-two-dimensionality electron gas, i.e. when the Fermi energy surface of the corrugated cylinder (open), is negative, and the magnitude is directly proportional $(\varepsilon_0/k_0 T)^{1/2}$ и and inversely logarithmically depends on r_0/a.

For quasi-three-dimensionality electron gas, in this case, the formula (4.8) shows that the sign of the coefficient can change.

In a strong magnetic field $\Omega\tau \gg 1$, taking into account the NE coefficient, we obtain

$$\frac{Q}{Q_0} = -\frac{1}{B^2 u_{\perp 0} u_{II0}}\left(\frac{k_0 T}{\varepsilon_0}\right)^{3/2}\frac{1}{2}\frac{I_{-1,-1,-1/2}}{I_{0,0,1}} = -\frac{1}{B^2 u_{\perp 0} u_{II0}}\left(\frac{k_0 T}{\varepsilon_0}\right)^{3/2}\frac{1}{2}\frac{\int_0^{Z_0} Z^{-1}X^{-1/2}\cos Z^{-1}dZ}{\sin Z_0 - Z_0 \cos Z_0} \tag{4.10}$$

Here $u_{II0} = e\tau_0/m_{II0}$ the mobility of the conduction electrons is perpendicular to the layer plane. It can be seen that in a strong magnetic field, the NE coefficient is negative, inversely dependent on B^2 and $u_\perp u_{II0}$, as well as directly proportional to $(k_0 T/\varepsilon_0)^{3/2}$

CONCLUSION.

The effect NE strongly depends on the direction of the magnetic field, so the anisotropy NE is investigated depending on the direction of the magnetic field. In this review, the NE coefficient of a low-dimensional (quasi-two-dimensionality and quasi-three-dimensionality) electron gas with a cosine law of dispersion in perpendicular and parallel magnetic fields relative to the layer plane is calculated with respect to the scattering of charge carriers on acoustic, polar optical phonons and impurity ions.

In the perpendicular magnetic field it was found that the scattering on acoustic phonons for quasi-two-dimensionality electron gas coefficient NE is zero, and the quasi-three-dimensionality gas is less than zero. When scattering on polar optical phonons, the NE coefficient is greater than zero, increases with the magnetic field at the open Fermi surface, while at the closed Fermi surface decreases. When scattering on weakly shielded ions of an impurity with an increase in the magnetic field, the sign of the effect changes from negative to positive, while in weak magnetic fields with an increase Z_0 in the sign of the effect chan–ges from positive to negative.

In parallel weak magnetic fields in the quasi-three-dimensionality case, the NE coefficient on module is increased, and this increase is almost three times greater in scattering by acoustic than by polar optical phonons. And in strong magnetic fields, the NE coefficient has small values and when the radius of the cyclotron orbit and the superlattice constant are of the same order,

the sign is inverted by scattering on polar optical phonons for a quasi-two-dimensionality electron gas. In strong magnetic fields at low concentrations, the NE coefficient for polar optical phonons changes sign to negative, as for acoustic phonons, and at high concentrations tends to zero. In strong magnetic fields, the NE coefficient at scattering by polar optical phonons in the same sample changes the sign a twice depending on the degree of miniband filling and the magnitude of the magnetic field. This feature of low-dimensionality electron gas can be used in nanoelectronic. In phonon scattering, the strong and weak magnetic field criteria are influenced by the parameters of the superlattice a and ε_0 . The NE coefficient in the scattering of charge carriers on weakly screened impurity ions with an increase in the concentration of charge carriers changes its sign from positive to negative. In the values $(r_0/a)\!>\!>\!1$ with increasing Z_0 electron gas Q/Q_0 changes its sign. The change of the sign of thermomagnetic coefficients is associated with the change of electronic orbits in relatively strong magnetic fields and the dependence of the screening radius on the concentration. In the case of a quasi-two-dimensionality electron gas, the NE coefficient is negative and monotonically depends on the magnetic field, and with increasing field tends to zero, while in the quasi-three-dimensionality case the NE coefficient is positive and also with increasing magnetic field tends to zero from the positive values.

REFERENCES

[1]   John H. Davies.The physics of low- dimensional semiconductors. Cambridge UniversityPress, 450p, 1998

[2]   Solid State Physics. Lund University. FFF N35- Physics of low-dimensional structures and quantum devices. Course info fall 2017

[3]   Т.Андо, А.Фаулер, Ф.Стерн.Электронные свойства двумерных систем. Пер.с анг.М.:Мир, 416 стр., 1985

[4]   В.П.Драгунов, И.Г.Неизвестный, В.А.Гридчин. Основы наноэлектроники. Новосибирск: Изд.НГТУ, 332стр., 2000

[5]   М.А.Херман. Полупроводниковые сверхрешетки.Мир, 240 стр.,1989

[6]   В.Н.Неверов, А.Н.Титов. Физика низкоразмерных систем.Екатернбург, 231стр., 2008

[7]   I. A. Lukyanchuk, A. A. Varlamov, A. V. Kavokin, Giant Nernst-Ettingshausen oscillations in semiclassically strong magnetic fields, Phys.Rev.Lett.Vol. 107, p.016601 , 2011

[8]   R. Fletcher, Magnetothermoelectric effects in semiconductor systems, Semicond. Sci. Technol. Vol.14, R1-R15, 1999

[9]   K. Behnia, M.A. Méasson, Y. Kopelevich, Oscillating Nernst-Ettingshausen effect in bismuth across the quantum limit, Phys. Rev Lett. Vol.98, p. 166602, 2007

[10]. J. Oji, Thermomagnetic effects in two-dimensional electron systems, J. Phys. C 17, p.3059, 1984

[11] V.P. Gusynin1, V.M. Loktev, I.A. Luk'yanchuk, S.G. Sharapov, A.A. Varlamov, Quantum oscillations as the tool for study of new functional materials, Low Temp. Phys.Vol.40, p. 355-366 , 2014

[12] E. H. Hwang, E. Rossi, S. Das Sharma, Theory of thermopower in 2D graphene, Phys. Rev. B 80,p. 235415, 2009

[13] Y.M. Zuev, W. Chang, P.Kim, Thermoelectric and magnetothermoelectric transport measurements of graphene, Phys.Rev.Lett.Vol.102, p. 096807, 2009

[14] J.G. Checkelsky and N.P. Ong, Thermopower and Nernst Effect in graphene in a magnetic field, Phys.Rev. B 80, p. 081413(R), 2009

[15] D.L.Bergman at al. Theory of dissipationless Nernst effects Phys.Rev.Lett. Vol.104, p.066601, 2010

[16] Z.Zhu, H.Yang, B. Fauque, Y. Kopelevich, K. Behnia, Nernst effect and dimensionality in the quantum limit, Nature Phys. Vol.6 , p. 26 ,2009

[17] X. Zianni, P. N. Butcher, M. J. Kearney, Semiclassical magnetothermopower of a quasi-two-dimensional electron gas, Phys. Rev. B 49, p.7520, 1994

[18] X.Z. Yan, C.S. Ting, Nernst effect of Dirac fermions in graphene under a weak magnetic field, Phys. Rev. B 81, p. 155457, 2010

[19] S. Goswami, C. Siegert, M. Pepper, I. Farrer, D.A. Ritchie, A. Ghosh, Signatures of an Anomalous Nernst Effect in a Mesoscopic Two-Dimensional Electron System, Phys. Rev. B83, p.073302, 2011

[20] A. Nogaret, Signature of phonon drag thermopower in periodically modulated structures, Phys. Rev. B 66, p.125302, 2002

[21] T. Liang, Q. Gibson, J. Xiong, M. Hirschberger, S.P. Koduvayur, R.J. Cava, N.P. Ong, Evidence for massive bulk Dirac fermions in $Pb_{1-x}Sn_xSe$ from Nernst and thermopower experiments, Nature communications , Vol.4, p.2696, 2013

[22] С.А.Немов, М.К.Житинская, Л.Е.Шелимова, Т.Е. Свечникова, Об анизотропии рассеяния дырок в слоистом соединении Bi_2Te_3 по данным коэффициента Нернста-Эттингсгаузена, ФТТ, Т. 50, стр.1166, 2008

[23] М.К.Житинская, С.А. Немов, Т.Е. Свечникова, Влияние неоднородностей кристаллов $PbSb_2Te_4$ на поперечный эффект Нернста-Эттингсгаузена, ФТП, Т. 31, стр.441, 1997

[24] O.V. Kirichenko, V.G. Peschansky, R.A.Hasan, Thermomagnetic phenomena in layered conductors, Low Temp. Phys. Vol.32, p. 1154, 2006

[25] O. Galbova, O.V. Kirichenko, V.G. Peschansky, Angular magnetic breakdown oscillations in organic conductors, Low Temp. Phys. Vol.39, p. 602, 2013

[26] B.M.Askerov, B.I.Kuliev, S.R.Figarova, I.R.Gadirova, Electron-phonon scattering and anisotropy of conductivity in quasi-two-dimensional systems, J.Phys.: Condens.Matter Vol.7, 843, 1995

[27] B.M.Askerov, Electron Transport Phenomena in Semiconductors, World Scientific, Singapore, 421p, 1994

[28] Б.М. Аскеров, Г.И. Гусейнов, С.Р. Фигарова, Анизотропия примесного рассе–яния и электропроводности квазидвумерных электронных систем, ФТТ, т.50,вып.4, стр.746-750, 2008

[29] S.R. Figarova, V.R. Figarov, Hall effect in a two-dimensional electron gas, Phil. Mag. Lett. Vol.87, p. 373, 2007

[30] Б.М. Аскеров, Г.И. Гусейнов, С.Р. Фигарова, Поперечное магнетосопротивление низкоразмерной электронной системы при рассеянии на ионах примеси, Вестник НАНА, серия Физико-Математический и Технический наук,Т. XXX, No.5 стр.3-8, 2010

[31] B.M. Askerov, S.R. Figarova, Thermodynamics, Gibbs method and Statistical Physics of Electron Gases. Springer, Heidelberg, 2010, 374p

[32] S.R.Figarova,V.R.Figarov. Transverse magnetorezistance in layered electron systems. EPL, Vol.89, p. 37004 , 2010

[33] Б.М. Аскеров, С.Р. Фигарова, Г.И. Гусейнов, Магнетосопротивление в слоистых полупроводниках при рассеянии на ионах примеси, ФТП Т. 48, вып.6, стр.768 ,2014 [34] H.İ.Hüseynov, Kvaziikiölçülü elektron sistemlərində fononlardan səpilmə halında Ner–nst-Ettinqshauzen effekti. Bakı, AzTU, Elmi əsərlər. Fundamental elmlər. Cild 2, No.2, s.29-33, 2015

[35] S.R. Figarova, H.I. Huseynov, V.R. Figarov. Transverse Nernst-Ettingshausen Effect in Superlattices Upon Electro-Phonon Scattering, Semiconductors, Vol.52, No.7, pp.853-858. 2018

[36] S.R. Figarova, H.I. Huseynov, V.R. Figarov. Anisotropy of Nernst-Ettingshausen Effect in Superlattices during scattering on Phonons, Russian Physics Journal, Vol.60, No.11, pp.1931-1937, 2018

[37] С.И.Борисенко, Расчет низкополевой подвижности квазидвумерных электронов в сверхрешетках $GaAs/Al_{0.36}Ga_{0.64}As$ в области температуры 77K, ФТП, Т. 36, стр.861, 2002

[38] С.Р.Фигарова, Г.И.Гусейнов, А.Ф.Асланлы. Концентрационная зависимость коэффициента Нернста-Эттингсгаузена в слоистых полупроводниках в продольном магнитном поле, Ученые записки. Физика, №1, стр. 64-72, 2017

[39] Б.М.Аскеров, С.Р.Фигарова, Г.И.Гусейнов, Поперечный эффект Нернста-Эттингсгаузена в сверхрешетках. Вестник Бакинского Университета, серия Физико-Математических наук. №1, стр. 86-92, 2013

[40] S.R.Figarova, H.I.Huseynov, Semiclassical Nernst-Ettingshausen effect of quasi-two-dimensional electron gas, 1st International Turkish World Engineering and Science Congress in Antalya, Turkey, December 7-10, 2017

[41] S.R. Figarova, H.I. Huseynov, V.R. Figarov. Magnetothermoelektric properties of layered structures for ion impurity scattering. Superlattices and Microstructures, Vol. 117, pp.469-475, 2018

INVESTIGATION OF THE INFLUENCE OF FILLER OF BIOLOGICAL ORIGIN ON THE STRUCTURE OF HIGH-PRESSURE POLYETHYLENE

E.M.GOJAYEV[1], V.V. SALIMOVA[2]

Head of department Physics, Azerbaijan Technical University[1],

geldar-04@mail.ru

Sumgait State University[2]

ABSTRACT

Were obtained polymeric-based composite materials with nanostructured metal filler and bio-filler, protect the material from environmental influences, including oxidation, and giving the required flexibility to the composite, subject to biocompatibility. Composites were obtained from a homogeneous mixture of the powders of the matrix components and the filler using a heated press at a temperature of 420 K and a pressure of 15 MPa. The quenching crystallization mode is the rapid cooling of samples in a water-ice mixture. The results of a study of IR spectra taken with a Fourier spectrometer Varian 640 FT-IR, high-pressure polyethylene composites modified with biological filler, and HPPE + x vol.% FS +y vol.% Fe bionanocomposites in the frequency range 4000-400 cm^{-1} were presented. It was revealed that the introduction of modifiers from fish scales and metallic nanoparticles (Fe) in HPPE in an optimal amount does not contribute to the appearance of new absorption bands, i.e., it practically does not change the shape of their IR spectrum. This means that the modifier of biological origin is technologically compatible with HPPE. The introduction of fish scale filler to HPPE contributes to a noticeable decrease in the intensity of the formation of C = O groups (1720 cm^{-1}), which is a measure of the oxidative degradation of polymer chains. The results show that the introduction of fish scales into the structures of high-pressure polyethylene contributes to the formation of an optimal and stable structure, which, in turn, interferes with the intensive development of the photo-oxidative process caused by UV irradiation.

Keywords: IR absorption spectra, fish scales, HPPE + x vol.% FS biocomposites, bionanocomposites.

ИССЛЕДОВАНИЯ ВЛИЯНИЕ НАПОЛНИТЕЛЯ БИОЛОГИЧЕСКОГО ПРОИСХОЖДЕНИЯ НА СТРУКТУРУ ПОЛИЭТИЛЕНА ВЫСОКОГО ДАВЛЕНИЯ

АННОТАЦИЯ

Были получены композитные материалы на полимерной основе с наноструктурным металлическим наполнителем и бионаполнителем, которые защищают материал от воздействий окружающей среды, в том числе от окисления, и придают композиту необходимую гибкость при условии биосовместимости. Композиты получали из гомогенной смеси порошков компонентов матрицы и наполнителя с использованием нагретого пресса при температуре 420 K и давлении 15 МПа.Режим закалочной кристаллизации - быстрое охлаждение образцов в смеси воды со льдом. Были представленырезультаты исследования ИК-спектров, снятых на Фурье-спектрометре Varian 640 FT-IR, композитовполиэтиленавысокого давления, модифицированного биологическим наполнителем и ПЭВД + х об.% РЧ + у об.% Fe бионанокомпозитов в диапазоне частот 4000- 400 см$^{-1}$. Выявлено, что введение в ПЭВД в оптимальном количестве модификаторов из чешуи рыб и металлических наночастиц (Fe) не способствует появлению новых полос поглощения, т. е. практически не меняет форму их ИК-спектра.Это означает, что модификатор биологического происхождения является технологически совместимым с ПЭВД. Введение в ПЭВДнаполнителя из рыбьей чешуи способствует заметному снижению интенсивности образования C = O групп (1720 см$^{-1}$), которая является мерой окислительной деградации полимерных цепей. Результаты показывают, что введение рыбьей чешуи в структуры полиэтилена высокого давления способствует формированию оптимальной и устойчивой структуры, что, в свою очередь, препятствует интенсивному развитию фотоокислительного процесса, вызванного УФ-облучением.

Ключевые слова:ИК-спектры поглощения, рыбья чешуя, ПЭВД + х об.% РЧ, биокомпозиты, бионанокомпозиты.

BİOLOJİ MƏNŞƏLİ DOLDURUCUNUN YÜKSƏK TƏZYİQLİ POLİETİLENİN STRUKTURUNA TƏSİRİNİN TƏDQİQİ

XÜLASƏ

Materialı ətraf mühitin təsirindən o cümlədən, oksidləşmədən qoruyan və kompozitə zəruri olan keyfiyyətləri təmin edən, polimer əsaslı bioəlaqəli və nanoquruluşlu metallik doldurucu nanokompozit materialları alınmışdır. Kompozitlər matrisanın və doldurucunun tozlarının bir-birinə qarışdırılaraq 420K temperaturda və 15MPa təzyiqdə alınmışdır. Proses başa çatdıqdan sonra alınmış nümunə əriməkdə olan buzda ani soyudulmuşdur. Təqdim olunan işdə YTPE+x həcm% BP +y həcm% Fe biokompozitlərinin Varian 640 FT-IR Furye spektrometrində alınmış İQ spektrləri 4000÷400sm⁻¹tezlik diapazonunda tədqiq edilmişdir.

Aşkar edilmişdir ki, yüksək təzyiqli polietilenə optimal miqdarda balıq pulcuqlaeından modifikatorlar və dəmir nanohissəciklərinin əlavə edilməsi İQ spektrdə yeni udma xətlərinin meydana çıxmasına səbəb olmur. Yəni doldurucu modifikatorlar İQ spektrin formasını səyişmir. Bu o deməkdir ki, bioloji modifikator və YT PY texnoloji baxımdan bir -birinə uyğundur. YTPE -yə balıq pulcuqlarının əlavə edilməsi 1720sm⁻¹-də müşahidə edilən intensivliyinin C=O azalmasına, bu da öz növbəsində polimer zəncirlərinin dağılmasına səbəb olur. Alınmış nəticələr göstərir ki, yüksək sıxlıülı polietilenin quruluşuna balıq pulcuğunun optimal miqdarda əlavə edilməsi dayanıqlı strukturlu ultrabənövşəyi şüalanma nəticəsində fotooksidləşmə prosesinin qarşısını alır.

Açar sözlər: IQ udulma spektrləri, balıq pulcuqları, YTPE + x həcm% BP, biokompozitlər, bionanokompozitlər.

Introduction

The expansion of polymeric materials use in various areas of national economy necessi-tates the development of technology for producing new polymeric composites with specified complexes of properties and stability with respect to the influence of external factors and biocompatibility. In the field of creating composite materials for special purposes, polymer composites have acquired the greatest relevance, whose properties are largely determined by the interaction of the polymer with the filler at the interface. Therefore, the regulation of interaction with the aim of improving the properties of composite materials when creating functional filled polymers is an important task and requires focused basic research, including in the field of filler modification, changing its structure, synthesis, phase and structure formation of metallic fillers. In terms of improving the wear resistance and biocompatibility of composites, it is of interest to study the material modification with biological fillers, which can be used in electronics in contact with the human body, as well as in food packaging [1-3]. From the researches done, nanocomposite was established as a promising route to enhance mechanical and barrier properties of biopolymers. Bio-nanocomposite is a multiphase material comprising of two or more constituents which are continuous phase or matrix particularly biopolymer and discontinuous nanodimensional phase or nanofiller (<100 nm). The nano-sized fillers play a structural role in which they act as reinforcement to improve the mechanical and barrier properties of the matrix. The unique physicochemical properties of transition metal nanowires, clusters and etc. are of great scientific interest [4,5]. Increased attention to these objects is primarily due to the fact that they are the main candidates for use in many areas of modern nanotechnology: spintronics, magnetic recording, highly sensitive magnetic sensors, etc. The use of the polymer matrix as a framework for low-dimensional metal structures and their protection from external influence is an important technological task. In particular, it is known to obtain and study some properties of composite materials of biological origin [6,7]. In these works, fish bones and scales with stable dielectric parameters were used as modifiers [6]. Their temperature and frequency characteristics of dielectric parameters [7], electrical and mechanical strength [8] were investigated. It is also known that one of the effective methods for detecting molecular structural changes in polymer composites that occur under external influence is IR spectroscopy. IR spectroscopy can provide

valuable information when figuring out the mechanism for changing the parameters of polymer composites. IR spectroscopy is widely used nowadays due to its versatility, the possibility of direct and independent determination of a number of important functional groups and structural fragments in small quantities of the test substance in any aggregative state and without any significant limitation of physical and chemical properties.

In this work, the structural changes in films obtained on the basis of high-pressure polyethylene modified with fish scales were studied by IR spectroscopy. The aim of the study was to create a composite material with a nanostructured magnetic metal filler and a bio-filler protecting the material from the influence of the external environment, including oxidation, and giving the composite the required flexibility, subject to biocompatibility.

Experimental Technique

To obtain biocomposites, high-pressure polyethylene (LDPE) of the brand M - 158 was used as a matrix, and fish scales (FS) were used as a filler. To obtain filler powders, at the beginning the fish scales were thoroughly cleaned and dried by gradually increasing the temperature from room temperature to 500°C, keeping at this temperature for 10 minutes, then dried fish scales in a special mill were ground into powder. The content of bio-fillers in composites ranged from 5 to 15% by volume. Composites were obtained from a homogeneous mixture of the powders of the matrix components and the filler using a heated press at a temperature of 420 K and a pressure of 15 MPa. The quenching crystallization mode is the rapid cooling of samples in a water-ice mixture.

To study the structural changes in biocomposites, an IR spectroscopy technique was used, based on measuring the transmission spectra of semi-transparent films. The spectra were measured in a Varian 640 FT-IR FTIR spectrometer in the wavelength range of 4000–400 cm^{-1}. Samples for the study were obtained in the form of thin films with a thickness of 1–10 μm and a size of 8×30 mm^2 by stepwise pressing under a pressure of $6 \cdot 10^4 N/m^2$ at room temperature using a special mold from Varian.

Experimental Results and Discussion

The experimental results obtained for the absorption bands of IR spectra for LDPE + x vol.% FS biocomposites and LDPE + x vol.% FS + y vol.% Fe biocomposites are shown in the figures. Comparison of these spectra shows that in all considered cases the introduction of modifiers from fish scales and metal nanoparticles into the LDPE does not contribute to the appearance of new absorption bands, i.e. does not change the overall shape of the IR spectra. This gives us reason to assume that these modifiers in the proposed volumetric amount are technologically compatible with LDPE. In other words, they mainly affect the physical structure of LDPE. As follows from the figure 1, the highest frequencies are characterized by the bands of free stretching vibrations not participating in the formation of hydrogen bonds, hydroxyl groups located on the edge of the considered spectral region (3857 cm^{-1}).

In the high-frequency region of the field of main oscillations of the molecules there can be bands of stretching vibrations of acetylene hydrogen C_{SP}-H, hydroxyl, primary and secondary amino groups. These bands usually intense, the contour and position of the bands OH and NH groups depend on their participation in the formation of hydrogen bonds. The occurrence of strong hydrogen bonds leads to a strong shift of the absorption maxima towards lower frequencies and a very significant increase in the width of the bands forming sometimes wide

absorption zones of a complex office with several arms and flat maxima. These bands may overlap with a group of bands of alkyl radicals and even be to the right of it. The weak absorption bands in the shortwave part of the IR spectrum not containing hydroxyl groups are explained by the admixture of moisture.

The formation of associates due to the O – H....O hydrogen bond is clearly traced in the IR spectrum due to a decrease in the O – H stretching vibration frequency and the manifestation of the second characteristic very wide band (3000-2800cm^{-1}) corresponding to numerous associates coexisting in equilibrium. The position of the bands of associated hydroxyl groups depends on the strength of hydrogen bonds, and for very strong associates, the frequency can be reduced to 2400 cm^{-1}. The intense absorption bands observed in the spectra of the overwhelming majority of organic substances in the region of 2800–3000 cm^{-1} correspond to the stretching vibrations of the hydrogen of the CH, CH$_2$, CH$_3$ groups. Hydrogen atoms associated with carbon in the sp^2 hybridization state have higher valence vibration frequencies (3000 - 2800 cm^{-1}). Here you can distinguish the group bands=CH$_2$ (2928.407 cm^{-1}) and CH (2853.4 cm^{-1}). Compounds containing the -CH = CH2 vinyl group have both bands in the spectrum. In the same area, there are much higher bands of stretching vibrations of acetylene hydrogen atoms≡C-H. The deformation vibrations have frequencies much less than the frequencies of valent vibrations of the same groups, so that all the bands of deformation vibrations are located in the area of "fingerprints". The exception is the bands of primary amino groups. Of the deformation vibrations of other hydrogen-containing groups, the antisymmetric and symmetric deformation vibrations of the methyl groups (1471-1462 and 1367 - 1352 cm^{-1}) of the scissors vibration of the methyl group are of the greatest importance for structural analysis. The absorption band at 757 cm^{-1} is responsible for vibrations of methylene groups. Another type of characteristic vibrations of molecules, which are very important for determining the structure of organic molecules, are the frequencies of stretching vibrations of double and triple bonds. In the C = N and O = N, C≡N, O≡N groupings, the reduced masses are close but the force constants differ significantly depending on the number of bonded electrons and reveal a clearly pronounced dependence on conjugation effects leading to a decrease in the numerical values of the characteristic frequencies of conjugate multiples connections compared to isolated. The intensity of the corresponding bands in the IR spectra depends on the polarity of these bonds. The polar groups of different electronegativity atoms (C = O, N = O, S = O, etc.) are characterized by a very high intensity of stretching vibration bands, which, according to this feature, are easily detected in the spectra. But double and triple bonds between identical atoms (C = C, N = N, C≡C) usually have medium and weak stretching vibration bands, and in symmetric structures such vibrations are generally inactive in the IR spectra.

IR spectra were also studied for LDPE + x vol. % FS + y vol.% Fe bionanocomposites. The results of study of their IR spectrum are shown in **Fig. 2.** As follows from the figure **2.** two bands are observed in the IR spectra of bionanocomposites in the frequency ranges of 1470 - 1450 cm^{-1} and 750 -700 cm^{-1}.

Antisymmetric C-H deformation oscillations, out-of-plane oscillations of five neighboring atoms N.

Analysis of the results shows that the proposed additives of biological origin in the optimal amount surpass other light stabilizers in their light-stabilizing features. This, apparently, is primarily due to the fact that, when introduced into LDPE, the fish scales used by us contribute to the formation of a more optimal and stable structure, which hamper the intensive development of the photo-oxidative process caused by UV irradiation.

Thus, from experimental data it can be seen that in modified LDPE films the optical density of IR absorption revealed end carbonyl groups in the sample, it can be concluded that fish scales reduce chemical changes in LDPE as a result of oxidation, destruction and crosslinking of polymer chains. This proves that the fish scale additive in the optimal amount is a physical structuring for LDPE, increases the packing density of polymer chains and hinders diffusion of ozone molecules into LDPE, which in turn weakens the oxidation processes.

Fig.1.IR spectra ofbiocompositesLDPE + x vol.%FS, where, 1-x = 1, 2-x = 5, 3-x = 7.
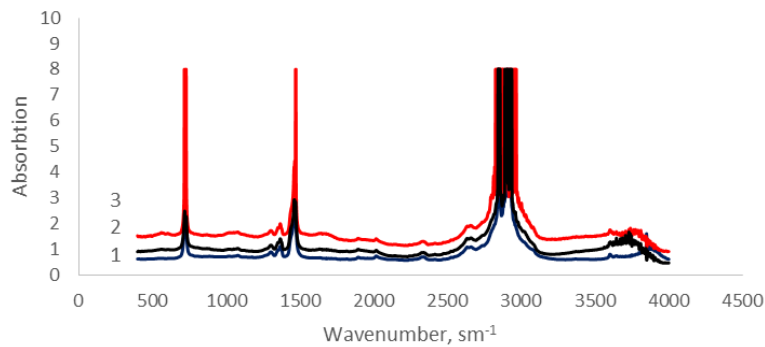
Fig.2. IR spectra ofbionanocompositesLDPE + x vol.% FS + y vol.% Fe, where,
1-x = 1, y = 1, 2-x = 5, y = 5, 3- x = 7, y = 3, 4 = x = 10, y = 10.
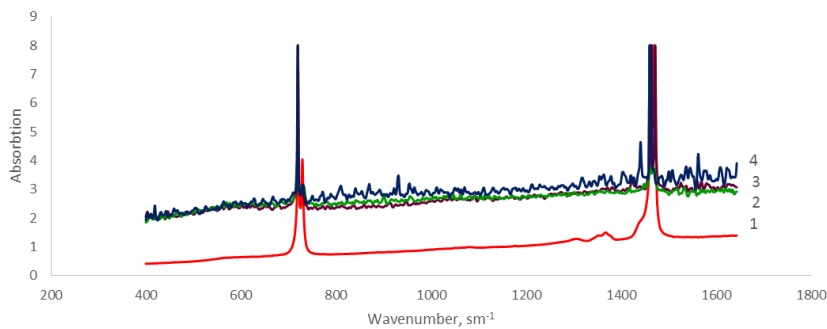
Conclusion

It was revealed that the introduction of modifiers from fish scales and metallic nanoparticles (Fe) in LDPE in an optimal amount does not contribute to the appearance of new absorption bands, i.e., it practically does not change the shape of their IR spectrum. This means that the modifier of biological origin is technologically compatible with LDPE. The introduction of fish scale filler to LDPE contributes to a noticeable decrease in the intensity of the formation of C = O groups (1720 cm^{-1}), which is a measure of the oxidative degradation of polymer chains.

REFERENCES

1. Choudalakis, G., Gotsis, A.D., 2009. Permeability of Polymer/Clay Nanocomposites: A Review. European Polymer Journal 45, 967–984

2. Bordes, P., Pollet, E., Avérous, L., 2009. Nano-Biocomposites: Biodegradable Polyester/Nanoclay Systems. Progress in Polymer Science 34, 125-155

3. John, M.; Thomas, S. Biofibres and biocomposites. Carbohydr. Polym. 2008, 71, 343–364.

4. Przybylski, M. Structure and magnetism of Fe mono- and multi-layer systems as seen by conversion electron Mössbauer spectroscopy at atomic scale. Hyperfine Interactions 1998, Vol.113, Is.1-4, pp.135–163. 113:135. https://doi.org/10.1023/A:1012619615420

5. K. Svensson, H. Olin, E. Olsson. Nanopipettes for Metal Transport. Phys. Rev. Lett. 93, Iss.14, 145901 (2004).

6. Godzhaev E.M., Salimova V.V., Aleskerova D.M. Surface micro-relief and dielectric properties of LDPE + x vol.% FS and LDPE + x vol.% $Bi_{0.5}Si_{1.5}Te_3$composites, International Journal of Innovative Science, Engineering & Technology, March 2017, Vol . 4, Issue 3, pp.42-45.

7. Gojaev E.M., Alieva Sh. V., Gulmammadov K. C., Osmanova S. S. Dielectric properties of fishbone kutum and com posite materials with its participation. Open Journal of Inorganic Non-Metallic Materials, 2016, 6, 1-5Published Online January 2016 in SciRes.http://www.scirp.org/journal/ojinmhttp://dx.doi.org/10.4236/ojinm.2016.61001

8. Gojaev E.M., Alieva, Sh.V., Nadirova N.B. The bones and scales of fish, their structure and dielectric properties. Actual problems of the humanities and natural sciences, Journal of Scientific Publications, 2015, №11, partV, pp.5-14.

THE INFLUENCE OF SOLAR ACTIVITY ON THE DISCOVERY OF PERIODIC COMETS OF THE JUPITER FAMILY*

Hazi GASIMOV

Baku Engineering University

hqasimov@beu.edu.az

ABSTRACT

The distribution of the dates of the discovery of comets of the Jupiter family from the phases of the 11-year cycle of solar activity (S.A.) is investigated in this work. The analysis covers 403 comets with aphelinic distances up to 7 a.u., found before the beginning of the 24th cycle. It is determined that the maximum in this distribution corresponds to the post-maximal epoch of the S.A. In this respect, periodic comets differ from long-period comets.

Key words: solar activity, periodic comets, observed dates.

YUPITER PERIODIK KOMET AILƏSININ MÜƏYYƏN OLUNMASINDA GÜNƏŞ AKTIVLIYININ ROLU

XÜLASƏ

Bu işdə Yupiter periodik komet ailəsinin kəşf olunma tarixləri Günəş aktivliyinin 11-illik dövrünün fazalarına görə tədqiq olunur. Tədqiqat afel məsafəsi 7 a.v.-dək olan 403 kometi əhatə edir. Müəyyən olunmuşdur ki, kometlərin kəşf olunma tarixlərinin maksimumu Günəş aktivliyinin maksimum müddətindən sonrakı dövrə uyğun gəlir. Bu baxımdan periodik kometlər uzun periodlu kometlərdən fərqlənirlər.

Açar sözlər: günəş aktivliyi, periodik kometlər, müşahidə tarixləri.

О ВЛИЯНИИ СОЛНЕЧНОЙ АКТИВНОСТИ НА ОТКРЫТИЕ ПЕРИОДИЧЕСКИХ КОМЕТ СЕМЕЙСТВА ЮПИТЕРА

РЕЗЮМЕ

В работе изучается вопрос о распределении дат открытия комет семейства Юпитера по фазам 11-летнего цикла Солнечной активности (С.А.). Анализ охватывает 403 кометы с афелийными расстояниями до 7а.е., найденные до начала 24-го цикла. Установлено, что максимум в этом распределении соответствует после-максимальной эпохе С.А. Периодические кометы в этом отношении отличаются от долгопериодических.

Ключевые слова: солнечная активность, периодические кометы, даты открытия.

Introduction

It is known that the aphelions of the orbits of short-period comets are unevenly distributed and are concentrated near the orbits of the giant planets. On this basis, short-period comets are divided into families. This pattern is one of the main dynamic features of these objects and, in the opinion of many researchers, can serve as a key to the problem of the origin of short-period comets.To test one or another concept of the origin of short-period comets, numerous calculations are carried out mainly relative to the Jupiter family. The propensity of researchers to the cometary family of this planet is due to two reasons. First of all, Jupiter is the most massive and closest giant planet to the Sun; secondly, the number of comets, the family of this planet, far exceeds the number of similar objects belonging to the families of other giant planets. More distant comet families, such as Saturn, Uranus and Neptune, are still almost unexplored. Therefore, along with the family of short-period Jupiter comets, we will consider these families and try to find out the patterns to which they obey.

The question of the influence of solar activity (S.A.), in particular the 11-year cycle on the distribution of cometary parameters, has been the subject of numerous studies. The most complete review of such works is contained in the monograph by Dobrovolsky [4].Numerous graphs regarding this factor are presented in the works of Z. Sekanin [5-7]. Svoren [8] found a number of dependences of cometary brightness on S.A., while using data from cycles 9-22. The existence of a good dependence of cometary parameters and characteristics on S.A. can be considered proven. If we consider all the comets, it turns out that many parameters show a two-vertex distribution.

In this case, they correspond to the period of decline and rise of the 11-year cycle. This is apparently due to the properties of the solar wind, which plays a major role in the physical development of comets as they approach the Sun or vice versa. The recent work of Guliyev and Gasimov [3] on the basis of more statistical material has once again confirmed the reality of the previously discovered two-peak distribution for long-period comets.

As shown by Guliyev [1], in this context, periodic comets are isolated. Some features of such comets are peculiar to the detection of a single-peaked maximum corresponding immediately after the maximum SA epoch. Hence the author of the cited article made a cosmogonic assumption about some differences in the physical properties of the nuclei of long-period and periodic comets. Further, this issue was considered in more detail in [2], where it was found that comets, the discovery of which occurred at different phases of the S.A., differ even in their dynamic features. Since the publication of work [1] more than three decades have passed, comets have been added to the catalogs for at least two 11- year cycles. This data is much larger than the period data of previous S.A. cycles.

In [2], its author instead of the traditional equation for determining the phase of the S.A

$$F = (t - T_1)/(T_2 - T_1) \tag{1}$$

used a moreperfect(2) equation

$$F = \begin{cases} \frac{t - T_1}{2(T_{max} - T_1)}; & if \ t - T_{max} < 0 \\ \frac{t - T_{max}}{2(T_2 - T_{max})} + 0.5; & if \ t - T_{max} > 0 \end{cases} \tag{2}$$

Here, t - the moment of discovery of the comet, T_1 and T_2 - the dates of successive minima of the S.A., T_{max} - the date of the maximum between them. The difference between (2) and (1) is that with this definition of the S.A. phase, the maximum always corresponds to the phase 0.5. In the classical phase definition [4-8], the maximum varies in a wide range of F and does not always coincide with the value 0.5. Graphical representation of the phase definition on the basis of these two equationsis given in Fig. 1a and 1b, respectively.

Fig.1. The determination of the phase of solar activity using equations (1) and (2)

1. b
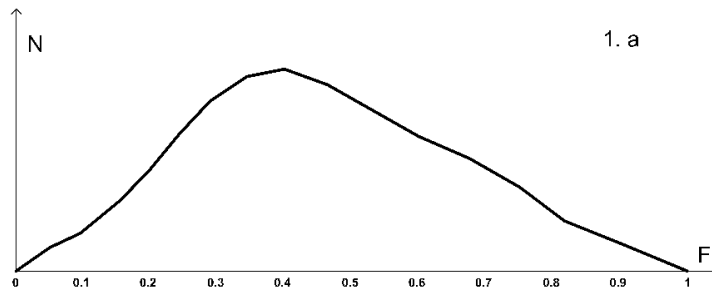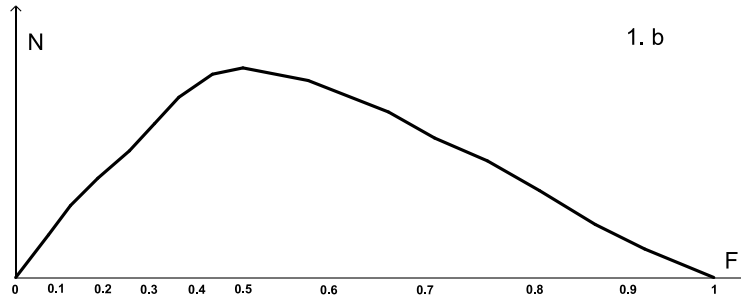
Statement of the question and the data used

In this paper, the discovery of periodic comets of the Jupiter family, depending on the S.A., will be analyzed in a broader context. Data from 1-23 S.A. cycles will be used, for comparison we note that in [2] the analysis covered the data of cycle 1-21, which corresponded to only 98 periodic comets. During the 1-23 cycles of the S.A., their number increased almost fourfold and amounted to 403. It is a matter of comets whose aphelion distances do not exceed 7 a.u. At the same time, one should keep in mind the fact that the contours of the Saturn family are now becoming clearer, and in time they become the rival to the Jupiter comet family. Therefore, comets possible contenders for the family of Saturn will be considered in a separate work.

Our list starts with comet 3D / 1772, (comet Biela), which collapsed and turned into a meteor shower, and ends with comet P / 2008 Y2. Of the 403 comets, 302 are numbered, 7 are considered "lost" and have the corresponding designation D. To determine the dates of discovery of the comets in question, the NASA site was used [9]. Comets of the main belt (the so-called MBCs) are not separately considered, they are still small, and they do not influence the overall statistics.

## The results of the analysis of the comet family of Jupiter

The results of the analysis are given in Table 1, where the number of (N) comet discoveries for each interval of the parameter F is given. It can be seen that the maximum amount falls on the interval 0.5-0.6 (N = 69) and the minimum at 0-0.1 (N = 13). In order to normalize the data of the table taking into account the asymmetry of the S.A., the data for the epochs 0-0.5 must be multiplied by 1.62 [3]. The normalized data (N_{eff}) are given in the third line of Table 1. Even with this factor in mind, it can be argued that the frequency of discovery of comets of the Jupiter family during the period of the S.A. decline is almost 2,4 times higher than the same value during the ascent period. Long-period comets do not possess such a property [2], and they have a two-vertex distribution of T from F, in which, according to the data of [3], the maximum abundances differ little from each other (131 and 123, respectively).

Table 1. Distribution of dates of discoveries of periodic comets Jupiter family by S.A. phases

N	F									
	0.1	0.2	0.3	0.4	0.5	0.6	0.7	0.8	0.9	1
Q<7AU	13	15	27	28	36	69	66	50	42	57
N_{eff}	21	24	44	45	58	69	66	50	42	57

Distributions of the periodic comets family of the Jupiter in accordance with the phase intervals of 1-23 cycles graphical representation has one maximum.The number of comets observed after the maximum epoch of solar activity increases.This activation begins in comets far from the Sun, after 4-5 yearsat the beginning of the phase. Fig.2 illustrates this very well.

**Fig 2.** The dependenceN (F) of the Jupiter comet family on the intervals of 1-23 cycles S.A.
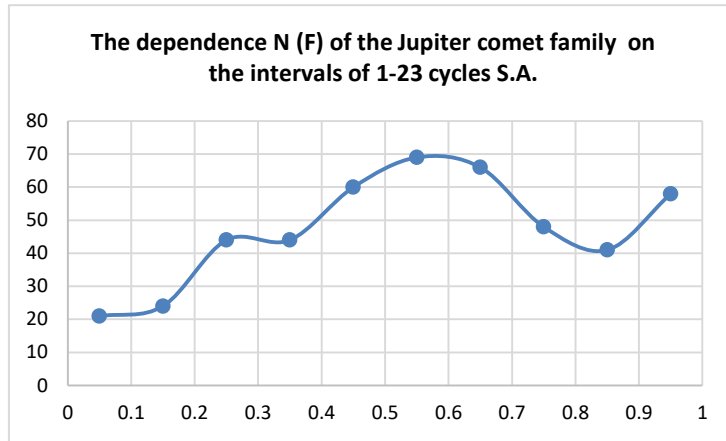
Sunspots are one of the active derivatives of the Sun and determine its overall activity. The magnetic field voltage in the spots is 4500 E.The total magnetic field voltage of the Sun is 1E. The magnetic field's pole in the spots varies according to 11-year cycles. It is important to learn the effect of this change on comets. Therefore, statistical analysis observed numbers of comets in single and double cycles results in very interesting. We conducted these statistical analyzes. In table 2 shows the results of analyzes conducted on single cycles.

Table 2. Distribution of Jupiter comet family by intervals of single cycles

N_{single}	F_{single}									
	0.1	0.2	0.3	0.4	0.5	0.6	0.7	0.8	0.9	1
Q<7AU	7	9	21	21	31	51	46	39	34	47
N_{eff}	11	15	34	34	50	51	46	39	34	47

When the graphical representation of the results is maximized, the curve corresponds to the range of 0.5 to 0.6.When viewing the table, the maximum number of comets (N = 51) was observed in the range of 0.5-0.6. A graphic description of these results is as follows.

**Fig 3.** The dependence N (F) of the Jupiter comet family on the intervals for single cycles S.A.
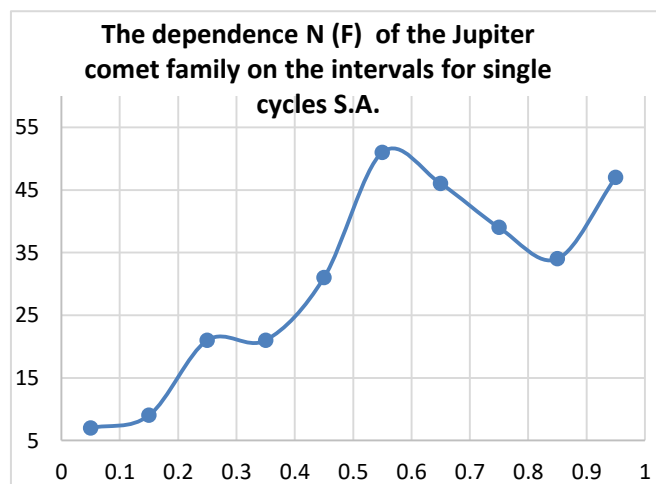
When looking at the intervals of the phase in double cycles, fewer comets are observed than single cycles. The maximum number (N = 20) comet was observed in the range 0.6 - 0.7 after the maximum epoxa. But here in single cycle, this number is more than twice (N = 51), the comet has been found.

Table 3. Distribution of Jupiter comet family by intervals of double cycles S.A.

N$_{double}$	F$_{double}$									
	0.1	0.2	0.3	0.4	0.5	0.6	0.7	0.8	0.9	1
Q<7AU	6	6	6	6	6	18	20	9	7	11
N$_{eff}$	10	10	10	10	10	18	20	9	7	11

When comparing the N (F) dependency graph for the double cycle intervals with the fig.3 constructed for interval cycles of single cycles, we can clearly see that comets have more reacting to solar activity in single cycles.

Fig 4. The dependence N (F) of the Jupiter comet family on the intervals for double cycles S.A.
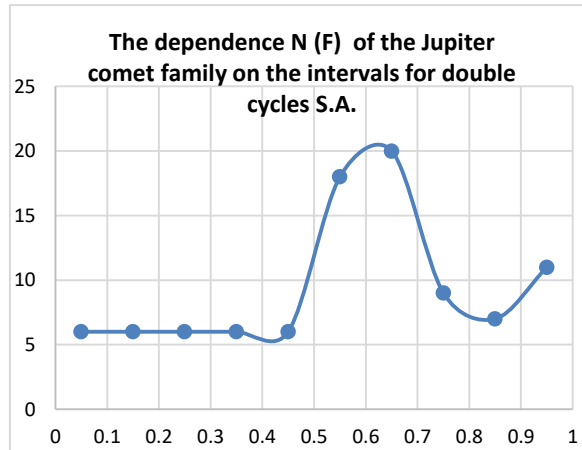
It is possible to conclude that each comet group reacts to the Solar activity in its own way.It was concluded in [1] that the reason for this deviation of the comets under consideration is apparently to be sought in the isolation of the physical properties of their nuclei. In any case, it can be connected with cosmogonic factors. Apparently the nuclei of these two classes of comets are formed in different regions of the solar system (for example, in the Kuiper belt and the Oort zone). Toclarifythisissue, we need to do more research.

*(ADPU-də doktorontların və gənc tədqiqatçıların XXII respubika konfransına göndərilmiş tezisin müzakirəsindən sonra hazırlanmış məqalə)

REFERENCES

1. Гулиев А.С. , 1985. О влиянии солнечной активности на открытие короткопериодических комет // Проблемы косм. физики. –20. – c. 39–43.
2. Гулиев А. С., 1990. О распределении кометных параметров по одиннадцатилетнему циклу солнечной активности // Кинематика и физика небесных тел. – т.6., 4. – c. 68–
3. GuliyevA.S.,Gasimov H.A., FarhadovaT.Distribution of parameters of long-period comets in of the phase 11-year solar activity cycle. Journal of Baku Engineering University-2017, v.2, 181-185 p.
4. ДобровольскийО. В., 1966. Кометы. М.: Наука. –288 c.
5. Secanina Z. Variation of the average absolute brightness of comets during an eleven-year solar cycle. Bulletin of the Astronomical Institute of Czechoslovakia, vol. 11, p.22-
6. Secanina Z. Changes of cometary characteristics as related to the changes of solar activity. Bulletin of the Astronomical Institute of Czechoslovakia, vol. 11, p.94-
7. Sekanina, Z. Solar activity as related to the statistics of comets. Bulletin of the Astronomical Institute of Czechoslovakia, vol. 10, p.103-104.
8. JánSvoreň Distribution of brightenings of periodic comets during solar activity cycles 9–22. Planetary and Space Science. Volume 118, 1 December 2015, Pages 176-180.
9. https://www.jpl.nasa.gov

INSTRUCTIONS FOR AUTHORS

1. "The Baku Engineering University Journal-Physics" accepts original unpublished articles and reviews in the research field of the author.

2. Articles are accepted in English.

3. File format should be compatible with **Microsoft Word** and must be sent to the electronic mail (**journal@beu.edu.az**) of the Journal. The submitted article should follow the following format:

- Article title, author's name and surname
- The name of workplace
- Mail address
- Abstract and key words

4. The title of the article should be in each of the three languages of the abstract and should be centred on the page and in bold capitals before each summary.

5. **The abstract** should be written in **9 point** type size, between **100** and **150** words. The abstract should be written in the language of the text and in two more languages given above. The abstracts of the article written in each of the three languages should correspond to one another. The keywords should be written in two more languages besides the language of the article and should be at least three words.

6. . **UDC** and **PACS** index should be used in the article.

7. The article must consist of the followings:

- Introduction
- Research method and research
- Discussion of research method and its results
- In case the reference is in Russian it must be given in the Latin alphabet with the original language shown in brackets.

8. **Figures, pictures, graphics and tables** must be of publishing quality and inside the text. Figures, pictures and graphics should be captioned underneath, tables should be captioned above.

9. **References** should be given in square brackets in the text and listed according to the order inside the text at the end of the article. In order to cite the same reference twice or more, the appropriate pages should be given while keeping the numerical order. For example: [7, p.15].

Information about each of the given references should be full, clear and accurate. The bibliographic description of the reference should be cited according to its type (monograph, textbook, scientific research paper and etc.) While citing to scientific research articles, materials of symposiums, conferences and other popular scientific events, the name of the article, lecture or paper should be given.

Samples:

a) *Article:* Demukhamedova S.D., Aliyeva İ.N., Godjayev N.M.. *Spatial and electronic structure af monomerrik and dimeric conapeetes of carnosine üith zinc,* Journal of structural Chemistry, Vol.51, No.5, p.824-832, 2010

b) *Book:* Christie ohn Geankoplis. *Transport Processes and Separation Process Principles.* Fourth Edition, Prentice Hall, p.386-398, 2002

c) *Conference paper:* Sadychov F.S., Aydın C., Ahmedov A.İ.. Appligation of Information – Commu-nication Technologies in Science and education. II International Conference."*Higher Twist Effects In Photon- Proton Collisions", Bakı, 01-03 Noyabr, 2007, ss 384-391*
References should be in 9-point type size.

10. The margins sizes of the page: - Top 2.8 cm. bottom 2.8 cm. left 2.5 cm, right 2.5 cm. The article main text should be written in Palatino Linotype 11 point type size single-spaced. Paragraph spacing should be 6 point.

11. The maximum number of pages for an article should not exceed 15 pages

12. The decision to publish a given article is made through the following procedures:

- The article is sent to at least to experts.
- The article is sent back to the author to make amendments upon the recommendations of referees.
- After author makes amendments upon the recommendations of referees the article can be sent for the publication by the Editorial Board of the journal.

YAZI VƏ NƏŞR QAYDALARI

1. "Journal of Baku Engineering University" Fizika- əvvəllər nəşr olunmamış orijinal əsərləri və müəllifin tədqiqat sahəsi üzrə yazılmış icmal məqalələri qəbul edir.

2. Məqalələr İngilis dilində qəbul edilir.

3. Yazılar **Microsoft Word** yazı proqramında, (**journal@beu.edu.az**) ünvanına göndərilməlidir. Göndərilən məqalələrdə aşağıdakılara nəzərə alınmalıdır:

- Məqalənin başlığı, müəllifin adı, soyadı,
- İş yeri,
- Elektron ünvanı,
- Xülasə və açar sözlər.

4. **Məqalədə başlıq hər xülasədən əvvəl** ortada, qara və böyük hərflə xülasələrin yazıldığı hər üç dildə olmalıdır.

5. **Xülasə** 100-150 söz aralığında olmaqla, 9 punto yazı tipi böyüklüyündə, məqalənin yazıldığı dildə və bundan əlavə yuxarıda göstərilən iki dildə olmalıdır. Məqalənin hər üç dildə yazılmış xülasəsi bir-birinin eyni olmalıdır. Açar sözlər uyğun xülasələrin sonunda onun yazıldığı dildə verilməklə ən azı üç sözdən ibarət olmalıdır.

6. Məqalədə UOT və PACS kodları göstərilməlidir.

7. Məqalə aşağıdakılardan ibarət olmalıdır:

- Giriş,
- Tədqiqat metodu
- Tədqiqat işinin müzakirəsi və onun nəticələri,
- İstinad ədəbiyyatı rus dilində olduğu halda orjinal dili mötərzə içərisində göstərməklə yalnız Latın əlifbası ilə verilməlidir.

8. **Şəkil**, **rəsm**, **grafik** və **cədvəllər** çapda düzgün, aydın çıxacaq vəziyyətdə və mətn içərisində olmalıdır. Şəkil, rəsm və grafiklərin yazıları onların altında yazılmalıdır. Cədvəllərdə başlıq cədvəlin üstündə yazılmalıdır.

9. **Mənbələr** mətn içərisində kvadrat mötərizə daxilində göstərilməklə məqalənin sonunda mətn daxilindəki sıra ilə düzülməlidir. Eyni mənbəyə iki və daha cox istinad edildikdə əvvəlki sıra sayı saxlanmaqla müvafiq səhifələr göstərilməlidir. Məsələn: [7,səh.15].

Ədəbiyyat siyahısında verilən hər bir istinad haqqında məlumat tam və dəqiq olmalıdır. İstinad olunan mənbənin biblioqrafik təsviri onun növündən (monoqrafiya, dərslik, elmi məqalə və s.) asılı olaraq verilməlidir. Elmi mə-qalələrə, simpozium, konfrans, və digər nüfuzlu elmi tədbirlərin materiallarına və ya tezislərinə istinad edərkən məqalənin, məruzənin və ya tezisin adı göstərilməlidir.

Nümunələr:

a) *Məqalə:* Demukhamedova S.D., Aliyeva İ.N., Godjayev N.M.. *Spatial and electronic structure af monomeric and dimeric complexes of carnosine with zinc,* Journal of structural Chemistry, Vol.51, No.5, p.824-832, 2010

b) *Kitab:* Christie ohn Geankoplis. *Transport Processes and Separation Process Principles*. Fourth Edition, Prentice Hall, 2002

c) *Konfrans:* Sadychov F.S., Aydın C., Ahmedov A.İ.. Appligation of Information-Communication Technologies in Science and education. II International Conference. "*Higher Twist Effects In Photon- Proton Collisions",* *Bakı, 01-03 Noyabr, 2007, ss 384-391*

Mənbələr 9 punto yazı tipi böyüklüyündə olmalıdır.

10. **Səhifə ölçüləri:** üstdən 2.8 sm, altdan 2.8 sm, soldan 2.5 sm və sağdan 2.5 sm olmalıdır. Mətn 11 punto yazı tipi böyüklüyündə, **Palatino Linotype** yazı tipi ilə və tək simvol aralığında yazılmalıdır. Paraqraflar arasında 6 punto yazı tipi aralığında məsafə olmalıdır.

11. Orijinal tədqiqat əsərlərinin tam mətni bir qayda olaraq 15 səhifədən artıq olmamalıdır.

12. Məqalənin nəşrə təqdimi aşağıdakı qaydada aparılır:

- Hər məqallə ən azı iki ekspertə göndərilir.
- Ekspertlərin tövsiyələrini nəzərə almaq üçün məqalə müəllifə göndərilir.
- Məqalə, ekspertlərin tənqidi qeydləri müəllif tərəfindən nəzərə alındıqdan sonra Jurnalın Redaksiya Heyəti tərəfindən çapa təqdim oluna bilər.

YAZIM KURALLARI

1. "Journal of Baku Engineering University-Physics" önceler yayımlanmamış orijinal çalışmaları ve yazarın kendi araştırma alanın-da yazılmış derleme makaleleri kabul etmektedir.

2. Makaleler İngilizce kabul edilir.

3. Makaleler Microsoft Word yazı programında, (**journal@beu.edu.az**) adresine gönderilmelidir. Gönderilen makalelerde şunlar dikkate alınmalıdır:
- Makalenin başlığı, yazarın adı, soyadı,
- İş yeri,
- E-posta adresi,
- Özet ve anahtar kelimeler.

4. **Özet** 100-150 kelime arasında olup 9 font büyüklüğünde, makalenin yazıldığı dilde ve yukarıda belirtilen iki dilde olmalıdır. Makalenin her üç dilde yazılmış özeti birbirinin aynı olmalıdır. Anahtar kelimeler uygun özetin sonunda onun yazıldığı dilde verilmekle en az üç sözcükten oluşmalıdır.

5. Makalede UOT ve PACS tipli kodlar gösterilmelidir.

6. Makale şunlardan oluşmalıdır:
- Giriş,
- Araştırma yöntemi
- Araştırma
- Tartışma ve sonuçlar,
- İstinat Edebiyatı Rusça olduğu halde orjinal dili parantez içerisinde göstermekle yalnız Latin alfabesi ile verilmelidir.

7. **Şekil, Resim, Grafik** ve **Tablolar** baskıda düzgün çıkacak nitelikte ve metin içerisinde olmalıdır. Şekil, Resim ve grafiklerin yazıları onların alt kısımda yer almalıdır. Tablolarda ise başlık, tablonun üst kısmında bulunmalıdır.

8. **Kullanılan kaynaklar**, metin dâhilinde köşeli parantez içerisinde numaralandırılmalı, aynı sırayla metin sonunda gösterilmelidir. Aynı kaynaklara tekrar başvurulduğunda sıra muhafaza edilmelidir. Örneğin: [7,seh.15].

Referans verilen her bir kaynağın künyesi tam ve kesin olmalıdır. Referans gösterilen kaynağın türü de eserin türüne (monografi, derslik, ilmî makale vs.) uygun olarak verilmelidir. İlmi makalelere, sempozyum, ve konferanslara müracaat ederken makalenin, bildirinin veya bildiri özetlerinin adı da gösterilmelidir.

Örnekler:

a) *Makale:* Demukhamedova S.D., Aliyeva İ.N., Godjayev N.M.. *Spatial and Electronic Structure of Monomerik and Dimeric Conapeetes of Carnosine Üith Zinc,* Journal of Structural Chemistry, Vol.51, No.5, p.824-832, 2010

b) *Kitap:* Christie ohn Geankoplis. *Transport Processes and Separation Process Principles.* Fourth Edition, Prentice Hall, p.386-398, 2002

c) *Kongre:* Sadychov F.S., Aydın C., Ahmedov A.İ. Appligation of Information-Communication Technologies in Science and education. II International Conference. *"Higher Twist Effects In Photon- Proton Collisions", Bakı, 01-03 Noyabr, 2007, ss 384-391*

Kaynakların büyüklüğü 9 punto olmalıdır.

9. **Sayfa ölçüleri**; üst: 2.8 cm, alt: 2.8 cm, sol: 2.5 cm, sağ: 2.5 cm şeklinde olmalıdır. Metin 11 punto büyüklükte **Palatino Linotype** fontu ile ve tek aralıkta yazılmalıdır. Paragraflar arasında 6 puntoluk yazı mesafesinde olmalıdır.

10. Orijinal araştırma eserlerinin tam metni 15 sayfadan fazla olmamalıdır.

11. Makaleler dergi editör kurulunun kararı ile yayımlanır. Editörler makaleyi düzeltme için yazara geri gönderilebilir.

12. Makalenin yayına sunuşu aşağıdaki şekilde yapılır:
- Her makale en az iki uzmana gönderilir.
- Uzmanların tavsiyelerini dikkate almak için makale yazara gönderilir.
- Makale, uzmanların eleştirel notları yazar tarafından dikkate alındıktan sonra Derginin Yayın Kurulu tarafından yayına sunulabilir.

13. Azerbaycan dışından gönderilen ve yayımlanacak olan makaleler için,(derginin kendilerine gonderilmesi zamani posta karşılığı) 30 ABD Doları veya karşılığı TL, T.C. Ziraat Bankası/Üsküdar-İstanbul 0403 0050 5917 No'lu hesaba yatırılmalı ve makbuzu üniversitemize fakslanmalıdır.

ПРАВИЛА ДЛЯ АВТОРОВ

1. «Journal of Baku Engineering University» - Физика публикует оригинальные, научные статьи из области исследования автора и ранее не опубликованные.

2. Статьи принимаются на английском языке.

3. Рукописи должны быть набраны согласно программы **Microsoft Word** и отправлены на электронный адрес (**journal@beu.edu.az**). Отправляемые статьи должны учитывать следующие правила:

*   Название статьи, имя и фамилия авторов
*   Место работы
*   Электронный адрес
*   Аннотация и ключевые слова

4. **Заглавие статьи** пишется для каждой аннотации заглавными буквами, жирными буквами и располагается по центру. Заглавие и аннотации должны быть представлены на трех языках.

5. **Аннотация**, написанная на языке представленной статьи, должна содержать 100-150 слов, набранных шрифтом 9 punto. Кроме того, представляются аннотации на двух других выше указанных языках, перевод которых соответствует содержанию оригинала. Ключевые слова должны быть представлены после каждой аннотации на его языке и содержать не менее 3-х слов.

6. В статье должны быть указаны коды UOT и PACS.

7. Представленные статьи должны содержать:

*   Введение
*   Метод исследования
*   Обсуждение результатов исследования и выводов.
*   Если ссылаются на работу на русском языке, тогда оригинальный язык указывается в скобках, а ссылка дается только на латинском алфавите.

8. **Рисунки, картинки, графики и таблицы** должны быть четко выполнены и размещены внутри статьи. Подписи к рисункам размещаются под рисунком, картинкой или графиком. Название таблицы пишется над таблицей.

9. **Ссылки** на источники даются в тексте цифрой в квадратных скобках и располагаются в конце статьи в порядке цитирования в тексте. Если на один и тот же источник ссылаются два и более раз, необходимо указать соответствующую страницу, сохраняя порядковый номер цитирования. Например: [7, стр.15]. Библиографическое описание ссылаемой литературы должно быть проведено с учетом типа источника (монография, учебник, научная статья и др.). При ссылке на научную статью, материалы симпозиума, конференции или других значимых научных мероприятий должны быть указаны название статьи, доклада или тезиса.

    Например:

a) *Статья:* Demukhamedova S.D., Aliyeva I.N., Godjayev N.M. *Spatial and electronic structure of monomeric and dimeric complexes of carnosine with zinc,* Journal of Structural Chemistry, Vol.51, No.5, p.824-832, 2010

b) *Книга:* Christie on Geankoplis. *Transport Processes and Separation Process Principles.* Fourth Edition, Prentice Hall, 2002

c) *Конференция:* Sadychov F.S, Fydin C,Ahmedov A.I. Appligation of Information-Communication Nechnologies in Science and education. II International Conference. *"Higher Twist Effects In Photon-Proton Collision",* Bakı,01-03 Noyabr, 2007, ss.384-391

Список цитированной литературы набирается шрифтом 9 punto.

10. **Размеры страницы:** сверху 2.8 см, снизу 2.8 см, слева 2.5 и справа 2.5. Текст печатается шрифтом **Palatino Linotype**, размер шрифта 11 punto, интервал-одинарный. Параграфы должны быть разделены расстоянием, соответствующим интервалу 6 punto.

11. Полный объем оригинальной статьи, как правило, не должен превышать 15 страниц.

12. Представление статьи к печати производится в ниже указанном порядке:

*   Каждая статья посылается не менее двум экспертам.
*   Статья посылается автору для учета замечаний экспертов.
*   Статья, после того, как автор учел замечания экспертов, редакционной коллегией журнала может быть рекомендована к печати.